

DIGITAL ACCESS TO SCHOLARSHIP AT HARVARD
DASH.HARVARD.EDU

HARVARD LIBRARY


A Quantum Memory Network Based on Diamond Nanophotonics

Citation

Knaut, Can-Paul. 2025. A Quantum Memory Network Based on Diamond Nanophotonics. Doctoral Dissertation, Harvard University Graduate School of Arts and Sciences.

Link

https://dash.harvard.edu/handle/1/42719371

Terms of use

This article was downloaded from Harvard University's DASH repository, and is made available under the terms and conditions applicable to Other Posted Material (LAA), as set forth at

https://harvardwiki.atlassian.net/wiki/external/NGY5NDE4ZjgzNTc5NDQzMGIzZWZhMGFlOWI2M2EwYTg

Accessibility

https://accessibility.huit.harvard.edu/digital-accessibility-policy

Share Your Story

The Harvard community has made this article openly available.
Please share how this access benefits you. Submit a story

HARVARD
Kenneth C. Griffin

GRADUATE SCHOOL
OF ARTS AND SCIENCES

THESIS ACCEPTANCE CERTIFICATE

The undersigned, appointed by the

Department of Physics

have examined a dissertation entitled

A Quantum Memory Network Based on Diamond Nanophotonics

presented by Can-Paul Mithat Horst Knaut

candidate for the degree of Doctor of Philosophy and hereby certify that it is worthy of acceptance.

Signature _____

Typed name: Prof. Mikhail Lukin

Signature _____

Typed name: Prof. Philip Kim

Signature _____

Typed name: Prof. Marko Lončar

Date: October 4, 2024

A Quantum Memory Network Based on Diamond Nanophotonics

A DISSERTATION PRESENTED
BY
CAN-PAUL MITHAT HORST KNAUT
TO
THE DEPARTMENT OF PHYSICS

IN PARTIAL FULFILLMENT OF THE REQUIREMENTS
FOR THE DEGREE OF
DOCTOR OF PHILOSOPHY
IN THE SUBJECT OF
PHYSICS

HARVARD UNIVERSITY
CAMBRIDGE, MASSACHUSETTS
OCTOBER 4, 2024

©2024 – Can-Paul Mithat Horst Knaut
all rights reserved.

Thesis advisor: Professor Mikhail Lukin Can-Paul Mithat Horst Knaut

A Quantum Memory Network Based on Diamond Nanophotonics

Abstract

Quantum networks hold the potential to enable quantum-secured communication, distributed quantum computing, and non-local quantum sensing. To realize these applications, a versatile quantum network infrastructure must support entanglement between network nodes capable of storing, processing, and distributing quantum information, alongside high-fidelity photonic qubits that efficiently interface with these nodes. The silicon-vacancy (SiV) center in diamond, coupled to nanophotonic cavities, has recently emerged as a promising platform to meet these requirements. This system provides access to an electron spin as an optically active communication qubit and a ^{29}Si nuclear spin as a memory qubit, capable of storing quantum information for extended periods.

We first demonstrate that the SiV center's electron spin can efficiently generate single photons with complex spatiotemporal waveforms, facilitated by a novel asymmetric nanophotonic cavity design. We then establish a two-node quantum network between two SiV centers housed in separate laboratories and connected via optical fiber. To do so, we use photonic qubits to mediate entanglement between two spatially separated electron spins, as well as between two spatially separated nuclear spins. Finally, using bidirectional quantum frequency conversion, we convert the photonic qubits to telecommunication frequencies, enabling entanglement generation between the two nuclear spins via a 35 km fiber deployed in the Boston metropolitan area. These advancements mark progress toward large-scale, deployable quantum networks using SiV centers coupled to nanophotonic cavities.

Contents

Title Page **i**

Copyright **ii**

Abstract **iii**

Contents **iv**

Listing of Figures **vii**

Previously Published Material **ix**

Acknowledgments **x**

1 Introduction: Quantum Networks and Applications **1**
- 1.1 All-photonic quantum networks 2
- 1.2 Memory-based quantum networks 8
- 1.3 Thesis outline 13

2 Quantum Network Nodes Based on SiV Centers Coupled to Nanocavities **16**
- 2.1 The silicon-vacancy center in diamond 17
- 2.2 SiV centers coupled to nanophotonic cavities 20

3 Efficient Source of Shaped Single Photons Based on an Integrated Diamond Nanophotonic System **27**
- 3.1 Introduction 28
- 3.2 Single photon creation using SiV centers 29
- 3.3 Single-sided cavities for maximal efficiency 33
- 3.4 High-efficiency generation of shaped single photons 33
- 3.5 Towards generation of multi-photon entangled states 37

3.6 Theoretical description of single-photon generation . . . 39
3.7 Density matrix simulations of photon generation . . . 42

4 Entanglement of Nanophotonic Quantum Memory Nodes in a Telecom Network 48
4.1 Two-node quantum network using integrated nanophotonic systems . . . 50
4.2 Electronic spin entanglement . . . 53
4.3 Nuclear spin entanglement . . . 55
4.4 Entanglement distribution through 35 km of deployed fiber . . . 57
4.5 Outlook . . . 60
4.6 Spin-photon gates . . . 61
4.7 Experimental setup . . . 62
4.8 Frequency shifting . . . 64
4.9 Telecom frequency conversion . . . 65
4.10 Polarization stabilization . . . 67
4.11 Success rate . . . 69

5 Conclusion 71
5.1 Using single photons for entanglement distribution . . . 72
5.2 Nanofabrication and materials development . . . 72
5.3 Optimizing entanglement distribution . . . 73

Appendix A Supporting Material for Chapter 2 75
A.1 Nanophotonic cavity . . . 75
A.2 Experimental setup . . . 90
A.3 Experimental results . . . 94
A.4 Limitations . . . 97
A.5 High temperature operation . . . 99

Appendix B Supporting Material for Chapter 3 101
B.1 Control sequence . . . 101
B.2 Cavity-QED parameters . . . 103
B.3 Contrast error distillation . . . 104
B.4 Bell state fidelity and error calculation . . . 106
B.5 Fidelity budgets . . . 107
B.6 Efficiency breakdown . . . 109
B.7 System improvements . . . 111
B.8 SiV properties . . . 113
B.9 Entanglement results additional data . . . 114
B.10 Compatibility to true space-like separated nodes . . . 116

References 127

Listing of Figures

1.1 Bloch sphere and the BB84 protocol . . . 3
1.2 E91 quantum cryptography protocol . . . 6
1.3 Schematic depiction of memory-based quantum networks . . . 9
1.4 Basic functionality of a quantum repeater . . . 11

2.1 Subatomic- and level-structure of the ^{29}SiV center . . . 18
2.2 Nanophotonic system . . . 23
2.3 SiV-based quantum network node . . . 24

3.1 Photon creation and measurement setup schematic . . . 30
3.2 Photon extraction efficiency as a function of κ_w and κ_s . . . 32
3.3 Pulse-shaped single-photon generation . . . 32
3.4 n-photon stream detection . . . 35
3.5 Hyperfine splitting due to the ^{29}Si nuclear spin . . . 36
3.6 Level diagram of relevant electron-spin levels . . . 43
3.7 Gaussian photon model fit . . . 45
3.8 $g^{(2)}$ model prediction of Gaussian photon arrivals . . . 47
3.9 Simulated $g^{(2)}$ functions assuming various qubit decay rates γ_t . . . 47

4.1 A two-node quantum network of cavity-coupled solid state emitters . . . 51
4.2 Remote entanglement between two electronic spins . . . 54
4.3 Remote entanglement and long-lived storage using nuclear spins . . . 56
4.4 Nuclear spin entanglement distribution through 35 km of deployed fiber . . . 58
4.5 Spin-photon gate quantum circuits . . . 61
4.6 Schematic drawing of the two-node quantum network . . . 63
4.7 Optical resonance frequencies of 223 characterized cavity-coupled SiVs . . . 64
4.8 Frequency shifting/conversion setup . . . 66
4.9 Polarization stabilization . . . 68

A.1 Photonic cavity geometry . . . 79
A.2 Quasipotential and simulated bandstructure . . . 80

A.3 Mode volume trade-off 84
A.4 Reflection spectrum of overcoupled nanophotonic cavity 87
A.5 Reflection spectrum of cavity-coupled SiV center used to determine cooperativity . 90
A.6 Optical setup and control flow diagram 91
A.7 $g_{\Downarrow\Downarrow}{}^{(2)}$ auto-correlation measurements 97
A.8 Laser-induced reduction of T_1 99

B.1 Flow chart for experimental control sequence 102
B.2 Cavity-QED parameters 103
B.3 Average photon number per photonic qubit versus success rate 107
B.4 T_2 coherence times of the ^{29}Si nuclear spins 113
B.5 $|\Phi^-_{nn}\rangle$ Bell state fidelities for telecom conversion experiment 114
B.6 $|\Phi^+_{nn}\rangle$ Bell state fidelities for telecom conversion experiment. 115
B.7 $|\Phi^+_{nn}\rangle$ Bell state fidelities for decoupling experiment 115

Previously Published Material

Chapter 3, in its entirety, is published as:

Erik N. Knall, Can M. Knaut, Rivka Bekenstein, Daniel R. Assumpcao, Pavel L. Stroganov, Wenjie Gong, Yan Qi Huan, Pieter-Jan Stas, Bartholomeus Machielse, Michelle Chalupnik, David Levonian, Aziza Suleymanzade, Ralf Riedinger, Hongkun Park, Marko Lončar, Mihir K. Bhaskar, Mikhail D. Lukin, Efficient Source of Shaped Single Photons Based on an Integrated Diamond Nanophotonic System. *Physical Review Letters* **129**, 053603 (2022).

Chapter 4, in its entirety, is published as:

Can M. Knaut, Aziza Suleymanzade, Yan-Cheng Wei, Daniel R. Assumpcao, Pieter-Jan Stas, Yan Qi Huan, Bartholomeus Machielse, Erik N. Knall, Madison Sutula, Gefen Baranes, Neil Sinclair, Chawina De-Eknamkul, David S. Levonian, Mihir K. Bhaskar, Hongkun Park, Marko Lončar, Mikhail D. Lukin, Entanglement of nanophotonic quantum memory nodes in a telecom network. *Nature* **629**, 573–578 (2024).

Acknowledgments

A Ph.D. is often likened to a marathon. While there have undoubtedly been stretches of solitary and intense effort, this analogy captures only part of the journey. Unlike a marathon, my Ph.D. has not been a solitary pursuit. It has been shaped and sustained by the support and encouragement of many remarkable individuals. This section is dedicated to acknowledging them.

My deepest gratitude goes to my advisor, Misha Lukin. Working with Misha offered a remarkable balance of academic freedom and responsibility—a combination I thoroughly enjoyed and which has made me a better scientist. His intuition and experimental guidance, drawn from his unparalleled expertise in quantum optics and quantum information across various platforms, have been invaluable. I am especially grateful to Misha for fostering a culture of hard work while also taking the time to celebrate the achievements of his group members. Here's to many more years of successful developments. I am also deeply thankful to Marko Lončar for his significant contributions to my Ph.D. studies. As a dissertation committee member and key collaborator on the SiV project, his group's excellence in nanofabrication was essential to the success of my research. I also greatly valued Marko's personal and scientific insights shared over many chats throughout the years. Completing my thesis committee, Philip Kim has been a great source of an external perspective on my research and academic path, and I deeply appreciate him for this.

I would like to express my gratitude to the graduate students and postdocs in the Lukin group who mentored me over the past six years. Mihir Bhaskar was pivotal in teaching me experimental quantum optics techniques and played a key role in designing and building the newly commissioned

quantum network node used in my thesis experiments. Denis Sukachev was an invaluable mentor during my early years, guiding me in the art of setting up and debugging large-scale optical experiments. Bart Machielse, whose technological leadership over the nanophotonic platform was indispensable, deepened my understanding and appreciation of the platform and its strengths. He was also patient in mentoring me and other group members in nanofabrication techniques. As Mihir, Denis, and Bart transitioned from senior group members to industry collaborators, I was fortunate to continue benefiting from their insights and advice, both on scientific and personal levels.

I am also deeply grateful to David Levonian and Ralf Riedinger, whose work laid the foundation for my thesis experiments. Rivka Bekenstein was my partner in crime in building the newly commissioned quantum network node, and I am thankful for her hospitality in her new lab at the Hebrew University of Jerusalem. Pavel Stroganov deserves recognition for his foundational work on `pylabnet`, the experimental control software that became instrumental in my thesis. Lastly, I would like to thank Christian Nguyen and Ruffin Evans, whose brief overlap with my time in the group was filled with enjoyable and enriching interactions.

Building large-scale quantum network experiments requires teamwork across a wide range of disciplines. I was fortunate to work with a fantastic team of fellow graduate students and postdocs who made this endeavor both manageable and fun. Erik Knall was an essential collaborator, spearheading diamond nanofabrication efforts and contributing to multiple projects. Daniel Assumpcao was a vital partner during the early stages of my PhD, particularly in designing and building the entanglement generation experiment. His affiliation with Marko's group was an immense asset, bridging measurement goals with nanofabrication requirements. A big thanks goes to Pieter-Jan Stas and Yan Qi Huan, who joined the lab in the midst of the COVID-19 pandemic and quickly took ownership of our first quantum network node. Pieter-Jan's creativity and Yan Qi's merciless eye for detail have improved many experiments over the years. I had the privilege of working with Yan-Cheng Wei since his early years of grad school. Observing his journey—from his first splice to being the owner of a

complex multi-node experiment—was truly rewarding. Similarly, I owe big thanks to Aziza Suleymanzade, who accompanied me during the second half of my PhD. Her curiosity, scientific instinct, and rigor pushed me and my team to be better scientists. Gefen Baranes deserves recognition for providing valuable and theoretically sound applications of the SiV platform. I am also grateful for the opportunity to collaborate with Maddie Sutula, and I will never forget our brief stint as surface scientists. Moritz Merz, a visiting master's student, deserves recognition for his diligence and focus on iterative improvement, resulting in a time-delay interferometer of record stability. As I prepared to leave Harvard, the SiV team benefited from an influx of new members, and I'm grateful to have overlapped with Umut Yazlar, Maxim Sirotin, Eugene Knyazev, and Francisca Abdo Arias. With this top-notch team, I believe the SiV group is set up for continued success.

I also want to acknowledge my collaborators at Harvard. Neil Sinclair was an invaluable resource in bridging the quantum-classical gap and served as a great liaison with Marko's group, facilitating access to their state-of-the-art nanofabrication. Sophie Ding was instrumental in transferring nanofabrication knowledge to the SiV team. Hongkun Park supported the crucial diamond annealing process, while Evelyn Hu enriched my understanding of diamond surfaces and helped prepare me for my next chapter in Santa Barbara. I also thank Ben Dixon and Eric Bersin for benchmarking the quantum frequency conversion.

Next, my deepest thanks go to the members of the Lukin group. Every member I interacted with over the past five years enriched my experience in unique ways, and I am thankful for every single one. Special thanks to Brandon Grinkemeyer for his diligent bagel runs, Eric Peterson for many great conversations over the years, Tim Guo for being a fun office mate, and Nishad Maskara for being the perfect P271 co-TA. Marcin Kalinowski motivated me to pick up new hobbies (judo and poker—only the latter stuck), and Sasha Zibrov Sr. came to my rescue on numerous occasions. I would also like to thank Lukin group alumni Harry Levine, Trond Andersen, Leigh Martin, and Po Samutpraphoot for providing valuable career advice.

Harvard's dedicated staff played a crucial role in enabling my research. Sam Dakoulas and Elaine Mangelinkx were lifesavers, bringing structure to the sometimes chaotic day-to-day challenges. Special thanks also go to the graduate student support staff—Lisa Cacciabaudo, Jacob Barandes, and Silke Exner—for their unwavering support. Jim MacArthur deserves recognition for his contributions to our experimental control electronics.

My time in grad school was not all work— some play was involved. I am thankful for every brave participant of my regular poker nights. While many of the attendees were from my research group, I'm glad to have made many more friends at the table. I am particularly thankful to the regulars—Nathaniel, Axel, Katherine, Ariane, and Rome—who always kept the game going and made these gatherings so memorable.

Over the past five years, I've lived with various roommates. Each of them, in their own unique way, contributed to my grad school experience. I am especially thankful to those who shared the house with me during the depths of the COVID lockdown: Hannah, Charles, Christina, and Blanka. Together, we built a community that brought calm to a stressful time, and for that, I am grateful.

I also deeply appreciate my old-time friends, particularly Samuel, Theresa, and Roman. They supported me in my journey across the Atlantic, visited me, and always gave me something to look forward to on my trips back to Europe—or to wherever they happened to be living.

Finally, none of this would have been possible without the support of my family. I owe a special thanks to Yesim, who stepped in as my designated family member on the North American continent, and as a fellow physicist, offered invaluable wisdom on navigating grad school and research.

Above all, I deeply thank my parents, Dilistan and Christian, and my brother, Leon. I thank them for raising me with curiosity, encouraging me to chart my own path, and supporting me through all these years. This dissertation is dedicated to them.

To my parents, Dilistan and Christian, and my brother, Leon.

1

Introduction: Quantum Networks and Applications

Quantum mechanics, the fundamental theory describing the behavior of particles at atomic and subatomic scales, has profoundly impacted the modern technological era. It underpins the physics of semiconductors and was instrumental in the development of transistors and integrated circuits,

which form the backbone of modern electronics.

In 1981, Richard Feynman proposed using quantum computers to simulate quantum systems that are challenging to model classically [1,2]. Following this proposal, scientists began developing algorithms that could run on hypothetical quantum computers, leading to the creation of early quantum algorithms that demonstrated theoretical runtime advantages over the best-known classical algorithms [3,4,5]. The development of these algorithms spurred significant interest in realizing large-scale quantum computers, a field of research that remains highly active today [2].

Similar to the field of quantum computing, quantum networking also emerged shortly after Feynman's proposal. In 1984, Charles Bennett and Gilles Brassard introduced a method to utilize quantum-mechanical states of photons for distributing cryptographic keys in an information-theoretically secure manner—something unattainable through classical communication methods [6]. This scheme, known as BB84, marked the birth of quantum key distribution (QKD) and inspired researchers to explore the use of distributed quantum information in the context of all-photonic quantum networks.

1.1 All-photonic quantum networks

All-photonic quantum networks rely exclusively on photons to distribute quantum information. The BB84 protocol, the first proposal for a photonic quantum network application, serves as a foundational example. The fundamental unit of information in this field is called a quantum bit, or qubit. The possible states of a qubit are described by two basis states, denoted as $|0\rangle$ and $|1\rangle$, as well as any superposition of these states [7]. The Bloch sphere (Fig. 1.1 a) provides a convenient way to visualize single-qubit states. An arbitrary single-qubit state, $|\psi\rangle$ is represented as a point on the Bloch sphere. The intersections between the coordinate axes and the Bloch sphere define three orthogonal basis pairs. Specifically, the $|0\rangle$ / $|1\rangle$ basis corresponds to the poles of the Bloch sphere on

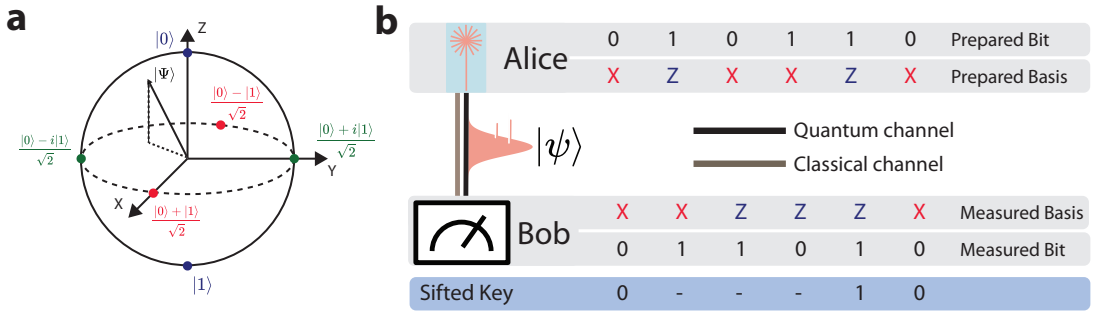


Figure 1.1: Bloch sphere and BB84 protocol **a.** The Bloch sphere, visualizing the quantum state of a single qubit. An arbitrary quantum state $|\Psi\rangle$ is described by a point on the Bloch's sphere. The z-, x-, and y-basis-vectors are highlighted in blue, red, and green, respectively. **b.** BB84 quantum cryptography scheme. Alice encodes a classical bit into the quantum state of a single photon $|\Psi\rangle$ by randomly choosing between bases Z, X, where Z corresponds to the z-basis $|0\rangle$, $|1\rangle$, and X to the x-basis $|+\rangle$, $|-\rangle$. Bob receives the encoded quantum states and randomly chooses between the same two bases for the measurement. Finally, Alice and Bob communicate the preparation and measurement bases and are able to distill a sifted key using the measurement results of the case where both measurement and preparation bases coincide.

the z-axis and is therefore referred to as the z-basis. The x- and y-bases are defined similarly.

With this notation at hand, we can introduce the BB84 protocol. Two parties named Alice and Bob want to securely exchange a cryptographic key. They have access to one authenticated classical channel, and one quantum channel. Alice now encodes the key into the quantum state of a photon, for example by using the polarization, or time-bin basis. For each bit, she randomly chooses between two possible bases, namely the z-basis,

$$|\Psi_0^z\rangle = |0\rangle \tag{1.1}$$

$$|\Psi_1^z\rangle = |1\rangle\,, \tag{1.2}$$

or the x-basis:

$$|\Psi_0^x\rangle = |+\rangle \equiv (|0\rangle + |1\rangle)/\sqrt{2} \tag{1.3}$$

$$|\Psi_1^x\rangle = |-\rangle \equiv (|0\rangle - |1\rangle)/\sqrt{2}. \tag{1.4}$$

Here, $|\Psi_i^j\rangle$, $i \in \{0,1\}, j \in \{z,x\}$ describe the quantum state encoding the bit i in the basis j, where z denotes the z-basis and x denotes the x-basis. Alice now sends the key encoded as described above via the quantum channel to Bob. Bob receives the quantum states and measures each bit using a randomly chosen basis z or x. As a last step, Alice and Bob use the authenticated classical channel to communicate the chosen measurement basis for each bit, which allows them to distill a shared key, called a *sifted* key, see Fig. 1.1 b.

The most general way an eavesdropper could compromise the security of the BB84 protocol is by intercepting the photons exchanged between Alice and Bob, attempting to clone their quantum states, storing one copy, and sending another to Bob. This strategy is known as the intercept-resend attack. After Alice and Bob communicate their measurement bases over an insecure public channel, the eavesdropper could then measure the stored copy and attempt to reconstruct the sifted key. However, the no-cloning theorem states that it is impossible to deterministically clone an arbitrary quantum state[8]. As a result, any cloning attempt by the eavesdropper will introduce errors in the sifted key. By comparing a subsection of the sifted key, Alice and Bob can obtain the sifted key error rate, known as the quantum bit error rate (QBER), to detect eavesdropping. Specifically, a QBER below 11% ensures that the information an eavesdropper can gain remains in a regime where the sifted key between Alice and Bob is secure[9]. This information-theoretical security is fundamentally different from the computational security provided by currently employed classical cryptography methods. Additionally, the relative simplicity of the BB84 protocol enabled its experimental realization just eight years after its proposal[10], making it an early example of experimentally demonstrated quantum advantage.

This early example of demonstrating the usefulness of distributed quantum information was followed by a proposal to use entanglement as a resource for quantum communication. Entangled composite quantum systems cannot be described by the individual quantum states of their constituents, but only on one global entangled state[7]. Specifically, for a two-qubit system, maximally

entangled states can be described by the following *Bell states*:

$$|\Phi^{\pm}\rangle = (|00\rangle \pm |11\rangle)/\sqrt{2} \tag{1.5}$$

$$|\Psi^{\pm}\rangle = (|01\rangle \pm |10\rangle)/\sqrt{2} \tag{1.6}$$

It is instructive to note that these entangled states cannot be written as product states of the form $|\Psi\rangle = |\alpha\rangle |\beta\rangle$, with $|\alpha\rangle$, and $|\beta\rangle$ being single qubit states. Moreover, upon measurement of one qubit, the quantum state of the other qubit collapses into a predetermined state, independent of the physical distance between the two qubits. These strong, non-local correlations are maintained in all qubit bases, which makes entanglement a unique feature of quantum mechanics, lacking an analog in classical physics. The non-locality of entanglement is also one of the key features that makes it a versatile resource in the field of quantum information.

For instance, an early QKD protocol named E91 protocol, after Artur Ekert, utilizes an entangled photon pair distributed between Alice and Bob to exchange a cryptographic key [11], see Fig. 1.2. An entangled Bell state $|\Psi^{-}\rangle$ of two photons is prepared and one photon is sent to Alice, and one to Bob. Alice now randomly chooses between three measurement bases in the x-y plane $\{\varphi_1^A = 0, \varphi_2^A = \pi/4, \varphi_3^A = \pi/2\}$, and Bob chooses between $\{\varphi_1^B = \pi/4, \varphi_2^B = \pi/2, \varphi_3^B = 3\pi/4\}$. Here, the angle φ is taken between the measurement basis and the x-axis. This procedure is repeated for each bit in the key, after which Alice and Bob use the classical communication channel to communicate the chosen measurement bases while keeping the measurement results secret. The measurements are then divided into two blocks: One block, corresponding to the measurements when the bases coincide, is used to distill a secret key, analogous to the case of the BB84 protocol demonstrated in Fig. 1.1 b.

The second block consists of measurements where Alice and Bob choose different bases, and its measurement results are openly communicated. These measurements are used to calculate the

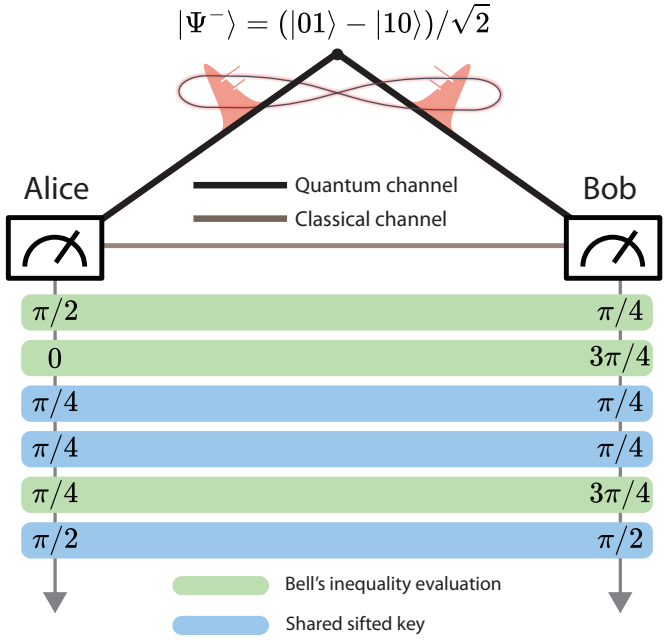


Figure 1.2: E91 protocol. A pair of photons is prepared in an entangled Bell state $|\Psi^-\rangle$. Using a quantum channel, one photon is sent to Alice, and one photon is sent to Bob. Alice and Bob measure the photons in randomly chosen bases and communicate the basis choice publicly via the classical channel. If the two bases coincide, Alice and Bob can use the results as a sifted key. If they are different, Alice and Bob communicate the measurement results and use them to calculate the value of S in Eq. (1.7). Verifying a violation of the CHSH inequality in Eq. (1.9) certifies the security of the transmission.

following metrics:

$$S = E(\varphi_1, \varphi_1) - E(\varphi_1, \varphi_3) + E(\varphi_3, \varphi_1) + E(\varphi_3, \varphi_3). \tag{1.7}$$

The quantity $E(\varphi_i, \varphi_j)$ is the correlation coefficient of the measurements performed by Alice along axis φ_i and Bob along axis φ_j, and is calculated as

$$E(\varphi_i, \varphi_j) = P_{++}(\varphi_i, \varphi_j) + P_{--}(\varphi_i, \varphi_j) - P_{-+}(\varphi_i, \varphi_j) - P_{+-}(\varphi_i, \varphi_j). \tag{1.8}$$

Here, $P_{\pm\pm}(\varphi_i, \varphi_j)$ describes the probability of Alice measuring $\pm$ in the basis φ_i, and Bob measur-

ing $\pm$ in the basis φ_j. Historically, quantities of the type S in Eq. (1.7) have been used to examine the question of locality and completeness of quantum mechanics. Specifically, it can be shown, that the value of S for a *local hidden-variable* theory is bound as follows [12]:

$$|S| \leq 2 \tag{1.9}$$

Equation (1.9) is known as the CHSH-inequality, and falls into the wider class of *Bell inequalities*. Calculating the metric S for the entangled state $|\Psi^-\rangle$, results in

$$S = -2\sqrt{2}, \tag{1.10}$$

which violates the CHSH-inequality. This observation led to Bell's theorem, a no-go theorem that states that if a hidden-variable theory is local it will not agree with quantum mechanics, and if it agrees with quantum mechanics it will not be local [13]. Since the formulation of this theorem in 1964, various experiments have demonstrated Bell's inequality violations, most notably 14 and 15, resulting in the conclusion that quantum mechanics is incompatible with a local hidden-variable theory.

Coming back to the description of the E91 protocol, these somewhat abstract results become very useful in certifying the security of quantum communication. Specifically, the value of S can be used to detect the presence of an eavesdropper. Assume an eavesdropper performs an intercept-resend attack on the photons distributed to Alice and Bob. The qubit measurement and subsequent state preparation of the cloned qubit introduces elements of a local, hidden-variable theory, which in turn results in a value of S obeying the CHSH inequality. Hence, by monitoring for a violation of the CHSH inequality, Alice and Bob can detect eavesdropping.

Both the BB84 and the E91 protocols are instructive examples of all-photonic schemes that

demonstrate how uniquely quantum mechanical properties like superposition and entanglement can be harnessed for secure communication. The fact that optical photons weakly interact with a room-temperature environment and each other makes them an ideal choice for so-called flying qubits. However, the difficulty of storing photons and non-destructively measuring them severely limits the functionality of all-photonic quantum networks. Extending the distribution of quantum information to a network that can not only distribute quantum information but also process and store it enables a host of new applications.

1.2 Memory-based quantum networks

Memory-based quantum networks can store, process, and distribute quantum information across different nodes [16,17]. Figure 1.3 shows a high-level schematic of a memory-based quantum network. Each quantum network node acts as a few-qubit quantum computer, containing two types of qubits, one communication qubit, and one memory qubit. The communication qubit contains a photonic interface that can be utilized while the memory qubit can store quantum information for extended periods. Photons act as flying qubits distributing quantum information throughout the network by traveling through photonic links, which connect the quantum network nodes. These links can be free-space, or optical fiber based. For the remainder of this thesis, we'll focus on optical-fiber-based networks. Within each node, single- and two-qubit gates are used to prepare the qubits in arbitrary quantum states, such as intra-node entangled states. The access to multiple types of qubits and the ability to store quantum information greatly extend the functionality of memory-based quantum networks. Three major applications of memory-based quantum networks are quantum repeaters [18,19], distributed quantum computing [20,21], and quantum-enhanced sensing [22,23], which will be introduced in the following.

Quantum repeaters address a fundamental challenge in quantum communication: photon loss.

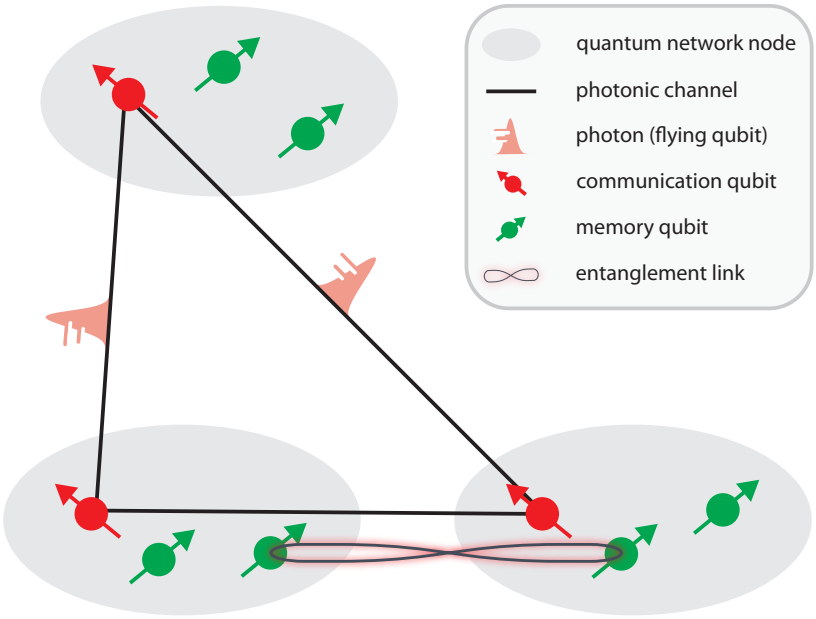


Figure 1.3: Schematic depiction of memory-based quantum networks. Each quantum network node contains two different types of qubits. One communication qubit interfaces with optical photons and one memory qubit stores quantum information for an extended time. The quantum network nodes are connected via photonic channels and carry optical photons, which act as flying qubits distributing quantum information throughout the network and establishing entanglement links between qubits.

Regardless of the type of photonic channel used, photon losses are inevitable. For fiber-based quantum networks, the lowest loss occurs in the telecom C-band, around 1550 nm. At this wavelength, light experiences attenuation of approximately 0.14 dB km^{-1} [2,4], which significantly limits the range of quantum communication. To illustrate this limitation, consider the BB84 protocol, where a quantum state $|\Psi\rangle$ is encoded at zero distance and then transmitted through an optical fiber of length l from Alice to Bob. Bob uses a realistic detector that, with each measurement attempt, has a probability p_d of registering a dark count—an erroneous detection event not caused by the transmitted photonic state. Additionally, Bob succeeds in measuring a photon from the distributed Bell pair with probability $p_s(l)$, which depends on the fiber distance l. The probability $p_s(l)$ can be expressed

as:

$$p_s(l) = p_s(0)10^{-\alpha_\lambda l}, \tag{1.11}$$

where $p_s(0)$ is the measurement success probability at zero distance, and α_λ is the wavelength-dependent attenuation coefficient in fiber in km^{-1}, with $\alpha_{1550\,\mathrm{nm}} = 0.014\,\mathrm{km}^{-1}$. The relationship between the dark count probability p_d and the measurement success probability $p_s(l)$ imposes a strict limit on the maximum fiber distance l. Specifically, when $p_d \geq p_s(l)$, Bob's measurements is dominated by dark counts, hindering his ability to distill a secure key. For a given ratio of $p_d/p_s(0)$, this imposes a maximal communication distance $l_{\max}$ of

$$l_{\max} = -\frac{\log_{10}\left(\frac{p_d}{p_s(0)}\right)}{\alpha_\lambda}. \tag{1.12}$$

This value for $l_{\max}$ is a theoretical upper bound. In practice, operating a quantum network at distances much lower than $l_{\max}$ is required to guarantee a reasonable key distribution rate. For current commercial QKD systems, the maximum fiber distance is around 150 km [25].

Note that the above argument also applies to classical communication. In classical systems, the distance limitation can be easily overcome by using classical signal repeaters, which are placed along the optical fiber path to periodically amplify the signal. However, when these repeaters are treated quantum mechanically, it becomes evident that this approach is not feasible for quantum networks. Specifically, perfect signal amplification in the quantum context involves measuring the quantum state of a photon and re-emitting the same state. This process closely resembles the intercept-resend attack in QKD. Consequently, the no-cloning theorem dictates that any attempt to reproduce a quantum state can only succeed probabilistically, making it unsuitable for a repeater. To address this limitation and extend the reach of quantum networks, the concept of quantum repeaters has been introduced [18].

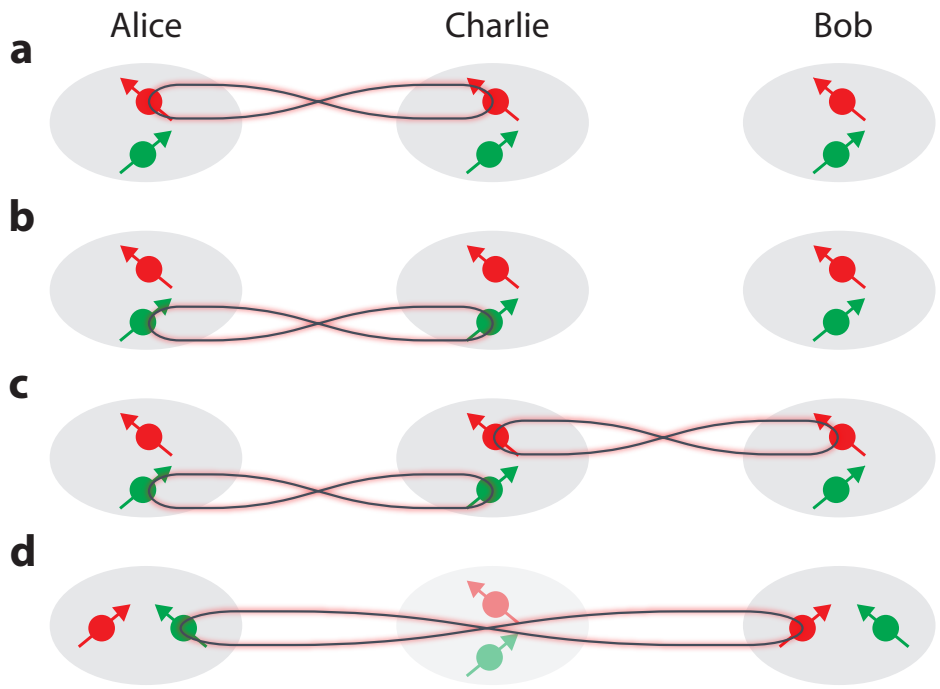


Figure 1.4: Basic functionality of a quantum repeater. Alice wants to share entanglement with Bob, however, the direct transmission distance between Alice and Bob is too high to directly transmit photons between them. An intermediate node Charlie is placed such that it's close enough to generate entanglement with both Alice and Bob. **a** The communication qubits of Alice and Charlie are entangled. **b** Alice and Charlie swap entanglement from the communication to the memory qubits. **c** While the quantum memories in Alice and Bob maintain the entangled state, entanglement between the communication qubits of Charlie and Bob is generated. **d** Once Charlie is entangled with both Alice and Bob, they perform a Bell State measurement on their two qubits, which teleports entanglement between Alice and Bob.

Consider two quantum network nodes, Alice and Bob, which are too far apart to establish direct entanglement, see Fig. 1.4. An intermediary node, Charlie, serves as a quantum repeater to extend the entanglement distance. The process begins by generating entanglement between Alice and Charlie, and separately between Charlie and Bob. A Bell state measurement performed by Charlie then teleports the entanglement and establishes it across the entire link from Alice to Bob. Constructing a quantum repeater network that surpasses direct transmission rates requires multi-qubit repeater nodes, high-quality intra-node gates between stationary qubits, and efficient coupling between photons and stationary qubits. Consequently, the development of quantum repeaters is a key

motivation for building memory-based quantum networks.

The quantum repeater protocol introduced here can be conceptualized as a distributed quantum circuit operating across multiple few-qubit quantum computers. This capability to distribute entanglement across a quantum computer network introduces an additional application for quantum memory networks: distributed quantum computing. By leveraging these networks, quantum computing modules can be interconnected, enhancing the computational power of the entire quantum computing cluster, akin to conventional high-performance computing systems[20]. This approach can preserve the fault tolerance of individual quantum computing modules, potentially enabling large-scale fault-tolerant quantum computing[26].

Modularizing quantum computing is likely to become crucial as all quantum computing platforms will inevitably encounter physical scaling limits as the number of qubits per quantum computer increases. For example, the number of qubits in a superconducting quantum computer[27] is limited by the space available within the cryostat required for cabling. Similarly, the number of trapped atoms (and hence qubits) in a neutral atom quantum processor[28] is constrained by the available laser power for atom trapping. Overcoming these physical limitations by creating entanglement links between modular quantum computers may be essential for scaling up the number of physical qubits to levels where useful quantum algorithms can be executed[29].

Furthermore, the combination of information-theoretical security in quantum communication with the capability to connect quantum computers opens up another unique application of quantum networks: distributed blind quantum computing[30]. In this scenario, a client can remotely access a quantum computer and securely delegate computations via the quantum network without needing to trust the quantum computer itself. Both distributed quantum computing and blind quantum computing underscores the need for quantum networks that not only distribute quantum information but also store and process it locally.

Besides being the key resource for quantum communication and distributed quantum comput-

ing, distributed quantum information also has the potential to enhance sensing measurements. Specifically, long-baseline optical interferometry has emerged as a candidate measurement to be enhanced by a quantum memory network [31,22]. In this application, two spatially separated optical telescopes intend to measure the phase difference between two photons emitted from a faint astronomical light source. By using entangled quantum memories as a resource, and mapping the photonic states onto quantum memories, a non-local Bell state measurement can be performed to measure the phase difference. This quantum-enhanced measurement circumvents direct transmission of weak photonic signals across long distances and could help increase the distance between telescopes, and hence the resolution of the measurement.

1.3 Thesis outline

The preceding examples illustrate that transitioning from all-photonic quantum networks to quantum memory networks unlocks a range of new applications, though it also introduces increased complexity. A few platforms have demonstrated various aspects of quantum memory network functionality, including neutral atoms [32,33,34,35], trapped ions [36,37], semiconductor quantum dots [38], nitrogen-vacancy (NV) centers in diamond [39,40], and atomic ensemble memories [41,42,43]. This thesis seeks to expand this list by demonstrating a quantum memory network based on silicon-vacancy (SiV) centers in diamond coupled to nanophotonic cavities.

Chapter 2 will introduce the quantum node technology used in this thesis. It focuses on a brief overview of the level structure of SiV centers coupled to ^{29}Si nuclei and the practical cooling requirements of SiV centers. It will furthermore present the cavity-quantum-electrodynamics (cavity-QED) platform utilized in this work, and highlight the strongly electron spin-dependent cavity reflectance as the backbone for all entangling operations.

In addition to the physical qubits that form part of the quantum network nodes, photonic

qubits, which act as flying qubits, are crucial for determining the network's performance. Chapter 3 will demonstrate that the quantum network platform introduced in Chapter 2 enables the high-efficiency generation of bandwidth-tunable single photons. This capability is verified by measuring the spatiotemporal distribution of the single photon wavepacket and the $g^{(2)}(\tau)$ autocorrelation function, demonstrating single photon purity. The results include the generation of photons with complex waveforms, ranging from a 1 μs long exponentially shaped photon to a 20 ns long Gaussian photon and a 700 ns long 10-peaked photon. The single photon purity was confirmed by observing a $g^{(2)}(0)$ value of 0.0168 for the Gaussian photon. Additionally, a high single photon detection efficiency of 14.9% was achieved. These results suggest that single photons generated by SiVs have the potential to replace weak coherent states as photonic qubits and could enhance entanglement rates in fully operational quantum networks.

Chapter 4 focuses on demonstrating the full quantum network functionality of the proposed platform in a realistic deployed fiber environment. Specifically, a two-node quantum network based on SiV centers coupled to nanophotonic cavities is constructed. This network comprises two quantum network nodes, each housed in a separate dilution refrigerator in different laboratories, connected via optical fiber. Using this network, entanglement between two spatially separated electron spins, which act as communication qubits, was demonstrated, achieving Bell state fidelities of up to $\mathcal{F} = 0.86(3)$. Similarly, two ^{29}Si nuclei, acting as memory qubits, were entangled with a Bell state fidelity of $\mathcal{F} = 0.77(5)$, with the entanglement preserved for up to 1 s. Finally, using bi-directional quantum frequency conversion, nuclear-nuclear entanglement was demonstrated over a 35 km long link of deployed fiber. These results mark the first realization of a quantum network based on SiV centers coupled to nanophotonic cavities and represent a significant step towards large-scale deployed quantum networks.

Chapter 5 will conclude the thesis by highlighting the upcoming challenges for the platform. Specifically, it will discuss the remaining challenges in incorporating the single photon source

demonstrated in Chapter 3 into a full quantum network, as well as the current limitations on rate and fidelity for the quantum network operations demonstrated in Chapter 4.

2

Quantum Network Nodes Based on SiV Centers Coupled to Nanocavities

2.1 The silicon-vacancy center in diamond

Quantum memory networks rely on an efficient matter-photon interface and require access to both communication and memory qubits. Solid-state systems based on spinful defects are a major candidate platform for large-scale quantum memory networks. When evaluating a material platform, several factors are crucial: a large bandgap to support optical transitions, the ability to deterministically generate defect centers with well-understood properties, and the achievement of long coherence times, among others. Various materials for spin defects are currently under active investigation, with host materials ranging from silicon[44], silicon carbide[45], and rare earths[46], to diamond[47]. Amongst this (non-exhaustive) list of host materials, diamond stands out as a material with a high bandgap of 5.5 eV and a robust industrialized manufacturing process of high-purity samples via chemical vapor deposition (CVD). This clean and transparent material platform allows for the deterministic creation of color centers, which are optically active point defects in the crystal structure.

The point defect utilized in this work is the silicon-vacancy (SiV) center in diamond. The SiV center is an inversion-symmetric point defect formed by an interstitial silicon atom positioned between a split vacancy site in the diamond lattice (see Fig. 2.1 a). SiV centers are created by implanting silicon ions into a high-purity diamond substrate and subsequent high-temperature annealing. The SiV center belongs to the D_{3d} symmetry group and is inversion symmetric with respect to the silicon atom[48]. Depending on the Fermi level of the surrounding diamond lattice, the SiV center can exchange charge with its environment, leading to various possible charge states. The prevalent charge state is the singly negatively charged SiV (SiV^-), where one additional electron is captured from the environment. In this thesis, unless otherwise specified, all SiV centers are assumed to be in the SiV^- state. The SiV^- center comprises 11 electrons: 6 contributed by the dangling carbon bonds, 4 from the silicon atom's valence electrons, and one captured from the environment. After filling up the available energy levels (which can be deduced by symmetry considerations, see 48), the electronic

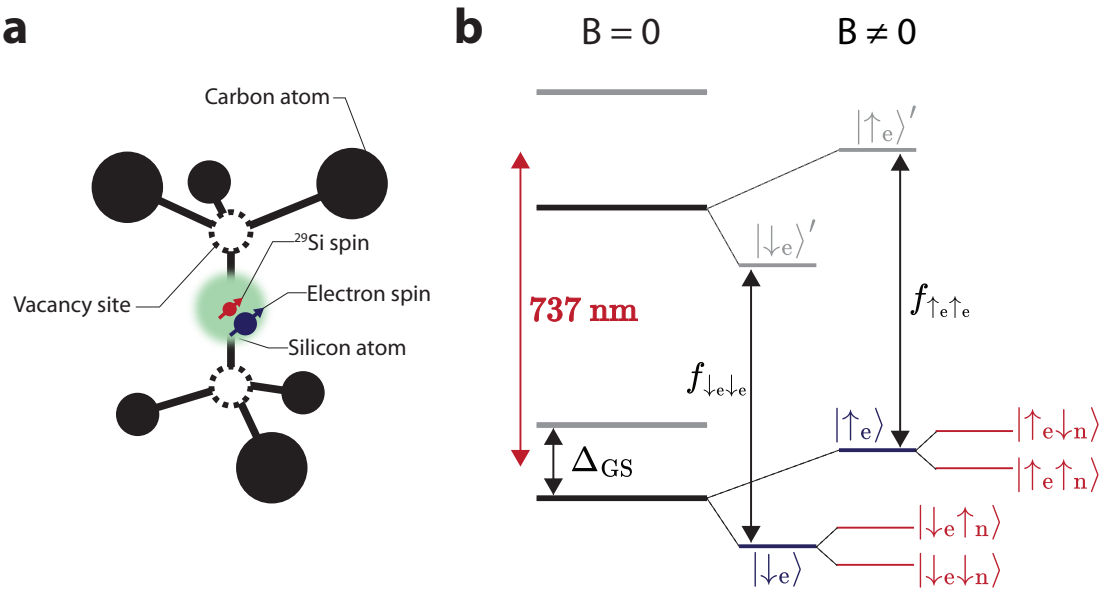


Figure 2.1: Subatomic- and level-structure of the ^{29}SiV center. **a** Schematic depiction of subatomic structure. The ^{29}SiV center is made up of a substitutional silicon atom sitting between a split lattice vacancy site in a diamond lattice. One free electron hole, commonly referred to as the electron spin, acts as the communication qubit. By selectively implanting the ^{29}Si isotope, an additional spin nuclear spin can be accessed, called the memory qubit. **b** Left: The SiV center's ground state manifold and excited state manifold are separated by 737 nm. This transition is used as a spin-photon interface. Both the ground- and excited state are split due to spin-orbit coupling and the Jahn-Teller effect. The splitting between the two ground states Δ_{GS} is strain-dependent. Right: After the application of an external magnetic field, the ground state splits into two Zeeman sublevels (blue), which are used as the communication qubit. Further splitting is due to the strong coupling between the electron spin and the nuclear spin (red).

structure can be simplified to one of an electron-hole, corresponding to a spin-1/2 system, with a ground and excited state separated by 737 nm, see Fig. 2.1 b, left.

This electronic degree of freedom is referred to as the SiV's electron spin, which, due to its optical transition, is used as a communication qubit interfacing with photons. The electron spin's ground and excited states exhibit orbital degeneracy, which is lifted by spin-orbit coupling and the Jahn-Teller effect. The splitting between the lower and the upper branches of the two ground states, Δ_{GS}, is known as ground-state splitting and, like the excited-state splitting, is dependent on the strain in the local diamond lattice environment.

The application of an external magnetic field lifts the spin-degeneracy of the energy levels of

the electron spin. It allows for the definition of the communication qubit states $|\downarrow_e\rangle$ and $|\uparrow_e\rangle$, see Fig. 2.1 b, right. The magnetic-dipole transition $|\downarrow_e\rangle \rightarrow |\uparrow_e\rangle$ can be driven with microwave (MW) pulses. When the external magnetic field is aligned with the symmetry axis of the SiV center, the optical transitions at frequencies $f_{\downarrow_e\downarrow_e}$ and $f_{\uparrow_e\uparrow_e}$ become spin-conserving, which allows for single-shot readout of the SiV center's electron spin state [49].

The orbital degeneracy and presence of an upper branch in the ground state manifold restrict the working temperature of the SiV center's electron spin to low temperatures. This is due to the thermal phonon population, which couples the two ground-state branches and results in the decoherence of the communication qubit. The exact operating temperature required for high-coherence operation depends on the value of the ground-state splitting Δ_{GS}. Specifically, the SiV center's temperature T should be much smaller than the temperature of the phonon bath at frequency Δ_{GS} [50]:

$$T \ll h\Delta_{GS}/k_B. \tag{2.1}$$

Here, h is the Planck constant, and k_B is the Boltzmann constant. For an unstrained SiV center, $\Delta_{GS} = 46\,\text{GHz}$, such that Eq. (2.1) reduces to $T \ll 2.2\,\text{K}$. This temperature constraint requires electron spins in unstrained SiV centers to be operated in dilution refrigerators, which allows cooling to temperatures well below 100 mK. At these temperatures, T_2 coherence times of around 10 ms in bulk [49], and around 1 ms [51] in nanostructures have been demonstrated. The low-temperature requirement can be alleviated by working with highly-strained SiV centers, which increases Δ_{GS} and thus the required operating temperature for high-coherence electron-spin operation [52,50]. Using highly strained SiV centers ($\Delta_{GS} = 554\,\text{GHz}$), electron-spin qubit operation at 1.5 K has been demonstrated [53].

As mentioned in Chapter 1, versatile quantum memory network operation requires not only communication qubits, which can interface with light but also memory qubits, which can store

quantum information for extended periods. In order to gain access to such a memory qubit, the ^{29}Si isotope is used during the implantation step, creating the ^{29}SiV center. Using this isotope gives access to an additional nuclear spin with spin-1/2. As this nucleus is part of the silicon atom and sits at the inversion center of the SiV center, the nuclear wavefunction has a large overlap with the wavefunctions of the electron in the ground and excited state, which results in strong coupling between the electron spin and the nuclear spin [54]. This results in an additional splitting of the electronic spin sublevels, see Fig. 2.1 b, right.

The entire two-qubit manifold can now be described by the four levels $|\downarrow_e\downarrow_n\rangle$, $|\downarrow_e\uparrow_n\rangle$, $|\uparrow_e\downarrow_n\rangle$, and $|\downarrow_e\downarrow_n\rangle$. Here, the subscript "e" indicates the electron spin, and the subscript "n" indicates the nuclear spin. The nuclear-spin flipping transitions $|\downarrow_e\downarrow_n\rangle \rightarrow |\downarrow_e\uparrow_n\rangle$ and $|\uparrow_e\downarrow_n\rangle \rightarrow |\uparrow_e\uparrow_n\rangle$ can be driven by radio-frequency (RF) pulses, while the electron-flipping transitions $|\downarrow_e\downarrow_n\rangle \rightarrow |\uparrow_e\downarrow_n\rangle$ and $|\downarrow_e\uparrow_n\rangle \rightarrow |\uparrow_e\uparrow_n\rangle$ are driven by MW pulses, as in the case without coupled ^{29}Si nucleus. Using this two-qubit system, it was possible to demonstrate T_2 coherence times of the ^{29}Si nucleus of over 2 s [53], making it a suitable memory qubit. Access to both communication and memory qubits is necessary for versatile quantum memory network operation. A strong interaction between the communication qubit and itinerant photons is also required. This thesis employs quantum network node technology that uses cavity-enhanced interactions to increase the matter-photon coupling strength.

2.2 SiV centers coupled to nanophotonic cavities

The key functionality of a quantum network node is to interface with light which is used to distribute quantum information through the network. In free space or in bulk material, the probability of interaction between a photon and an optically active emitter is limited by the ratio of the light's beam area A_B to the absorption cross-section the emitter σ_{Abs} [55]. Considering now an emitter

being placed in an optical cavity with a finesse $\mathcal{F}$. The cavity enhances the number of bounces of light by a factor of $\mathcal{F}/\pi$, which increases the interation-cross section of the emitter and hence the probability of absorption between the emitter and light. If the cavity-enhanced interaction cross-section is larger than the beam area, that is if

$$\sigma_{\text{Abs}} \times \mathcal{F}/\pi > A_B, \tag{2.2}$$

the interaction between light and emitter becomes deterministic. Equation (2.2) can we rewritten in terms of the parameters g, κ and γ, where g corresponds to the single photon Rabi frequency, κ_{tot} to the total cavity decay rate, and γ to the emitter's linewidth, all expressed as full widths at half max (FWHM). This results in

$$C = \frac{4g^2}{\kappa_{\text{tot}}\gamma} > 1. \tag{2.3}$$

The value C is referred to as cooperativity and is used as a figure of merit for cavity quantum electrodynamic (cavity QED) systems, with $C > 1$ being required for deterministic matter-photon interaction. The expression for the cooperativity can be rewritten as

$$C = \frac{3}{4\pi}\left(\frac{\lambda}{n}\right)^3 \left(\frac{Q}{V}\right)\left(\frac{\gamma_0}{\gamma}\right), \tag{2.4}$$

where n the index of refraction of the cavity material, $Q = \omega/\kappa_{\text{tot}}$ is the cavity's quality factor, ω is its resonance frequency, λ the corresponding wavelength in free space, V the cavity mode volume, and γ_0 the radiative emission line-width. Nanophotonic diamond cavities have achieved low mode volumes of $V \approx 0.5\left(\frac{\lambda}{n}\right)^3$, and quality factors of $Q > 10000$ [56], which in principle make color centers in diamond coupled to nanophotonics a promising platform for deterministic light-matter interaction.

When choosing the right emitter for integration into nanocavities, however, it is important to

consider the effect of the nanofabricated environment on the emitter. Compared to bulk-implanted color centers, emitters incorporated into nanostructures experience higher electric field noise. If an emitter has inequivalent permanent electric dipole moments in the ground and excited state, this field noise causes spectral diffusion. As the SiV center is inversion symmetric, it has a vanishing permanent electric dipole moment [57], making it first-order insensitivity to electric field noise. This noise insensitivity makes the SiV center a suitable candidate for integration into nanophotonic cavities. It also distinguishes the SiV center from the nitrogen-vacancy (NV) center, a diamond color center emitting at 637 nm, widely used in pioneering quantum memory network experiments [39,14,40]. The NV center, a spin-1 system with a non-degenerate ground state, exhibits millisecond-long electron-spin coherence times at room temperature [58]. However, despite its favorable spin properties, the NV center's lack of inversion symmetry results in significant spectral diffusion when integrated into nanocavities [59].

While the SiV^- is the naturally occurring charge state, recent work has focused on exploring the neutral SiV center, SiV^0, which shares certain similarities with the NV center. The SiV^0 center, with an optical transition at 946 nm, is a spin-1 system, and like the NV center, exhibits a non-degenerate ground state [60]. This results in T_2 coherence times of approximately 250 ms at 15 K [61]. Due to its maintained inversion symmetry, the SiV^0 center is theoretically a promising candidate for cavity-enhanced quantum network nodes at higher temperatures. However, practical utilization of the SiV^0 center is complicated by the need for Fermi-level pinning. Approaches to pin the diamond's Fermi level to a regime that favors the creation of SiV^0 over SiV^- include boron doping [61], surface engineering [62], and photoactivation of carriers [63], which are all challenging to integrate into a nanofabrication workflow. Hence, the negative SiV center is the currently preferred charge state for cavity-enhanced quantum network demonstrations.

The ability to integrate SiV centers into nanophotonic cavities is a key enabler for quantum memory networks based on SiVs. Figure 2.2 shows scanning electron micrographs of the type of

]

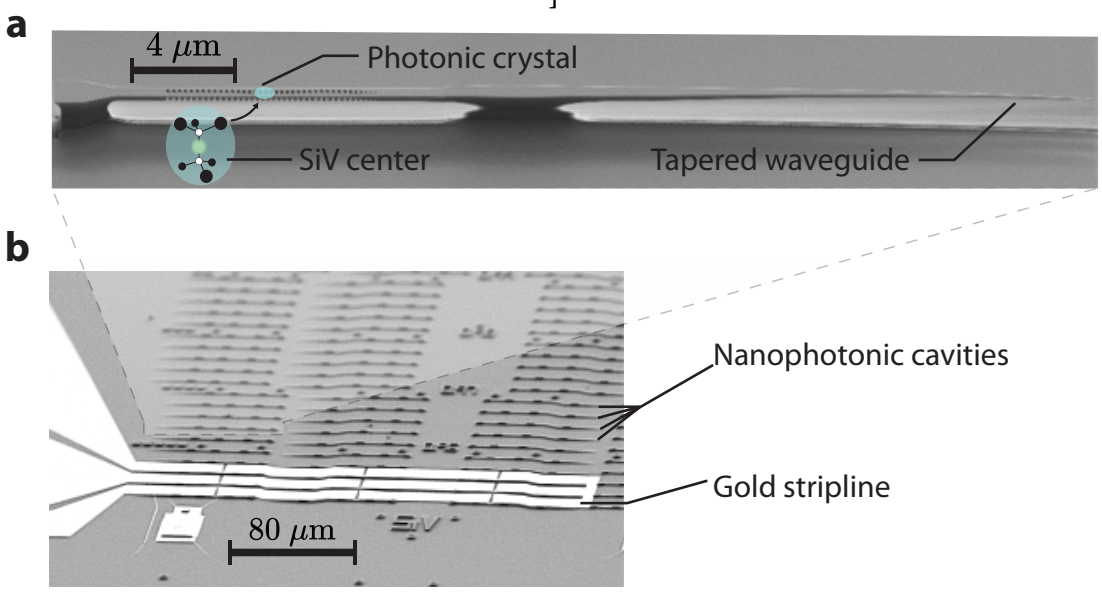


Figure 2.2: Scanning electron micrographs of diamond nanophotonic cavities coupled to SiV centers. **a.** Close-up of a single device, consisting of a free-standing diamond waveguide with a tapered section (right), and a photonic crystal section (left). By implanting silicon ions into the mode maximum of the nanophotonic cavities, SiV centers with strong coupling to the cavity can be created. **b.** Overview of the nanofabricated diamond chip, showing approximately 50 cavity devices, as well as a gold coplanar stripline, used to deliver MW and RF pulses to the SiV centers.

nanophotonic devices used in this thesis. They consist of diamond waveguides of triangular cross-section. One section of this waveguide contains periodically patterned elliptical holes that define a one-dimensional photonic crystal cavity. Silicon ions are implanted into the mode-maximum of this nanophotonic cavity and are used to create SiV centers which are strongly coupled to the cavity mode, with cooperativities up to around 100[64]. The cavity resonance wavelength can be tuned by depositing nitrogen gas onto the device, and selectively boiling it off. The waveguide contains a tapered fiber section used for photon outcoupling. A gold coplanar waveguide is patterned around the nanophotonic device and is used to deliver MW and RF pulses to the SiV center. For more details on the design and fabrication of the nanophotonic devices, see Chapter 3 and Appendix A.

The core of the quantum memory network node consists of a nanofabricated chip containing

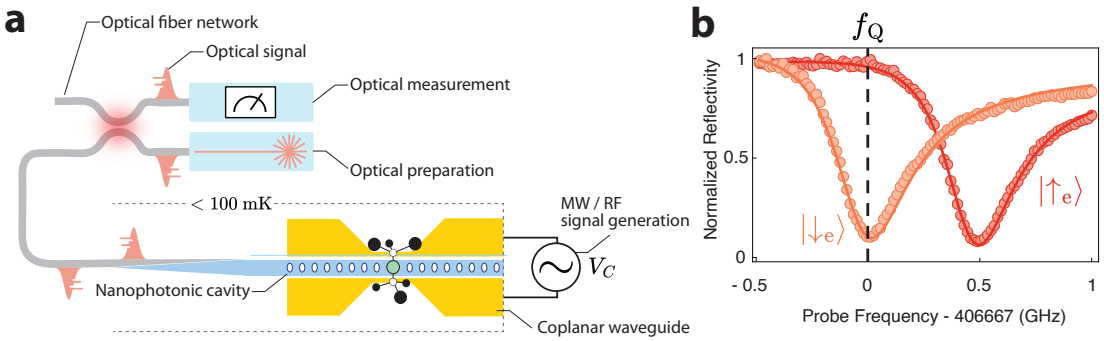


Figure 2.3: SiV center based quantum network node **a.** Schematic of a quantum network node. The nanophotonic cavity with an integrated SiV center is cooled down to below 100 mK by a dilution refrigerator. A tapered optical fiber is coupled to the nanophotonic cavity and connects it to a fiber network, which is used to send photonic signals into the cavity and to route photonic signals reflected off the cavity to an optical measurement setup. A coplanar waveguide is used to deliver MW and RF control signals V_C to the SiV center. **b.** Electron-spin-dependent reflectance of a SiV center coupled to a nanophotonic cavity in the entanglement generation regime. The nanophotonic cavity is detuned from the SiV center's optical frequency by approximately one cavity width κ_{tot}. The orange (red) data points correspond to the measured reflectance spectrum with the SiV center's electron spin initialized in the $|\downarrow_e\rangle$ ($|\uparrow_e\rangle$) state. The dashed line corresponds to the frequency f_Q of maximal reflectance contrast between the two spin states and is used for electron-spin state readout and entanglement generation. Solid curves correspond to a fit to Eq. (B.1). Figure b adapted from 65.

a cavity-coupled SiV center, addressed by a coplanar stripline, as schematically depicted in Fig. 2.3 a. The chip is housed in a dilution refrigerator that cools the device to below 100 mK, suppressing phonon-induced decoherence. A tapered optical fiber couples the tapered section of the waveguide, to a fiber network, with coupling efficiencies ranging from 70 % to 90 %. At the input of the fiber network, an optical preparation system equipped with lasers and pulse-shaping infrastructure prepares photonic qubits, control pulses, and electron-spin readout pulses. At the output, an optical measurement setup is employed. All optical measurements are performed in a reflection modality, where light is reflected off the cavity QED system and directed to the measurement apparatus. Depending on the specific measurement, this apparatus may include free-space optical filters, interferometers, single photon counting modules, and superconducting nanowire single-photon detectors. For details on the experimental setups used for single photon generation, refer to Section A.2.1, and for entanglement distribution, see Section 4.7.

A gold coplanar waveguide is used to manipulate the SiV center's electron and nuclear spins. This waveguide contains a narrowed section to concentrate the magnetic field near the SiV center and is connected via coaxial cables to a MW and RF preparation setup located outside the dilution refrigerator. The setup, comprising an arbitrary waveform generator, a frequency-mixing system, and a chain of MW switches and amplifiers, generates the qubit control signal V_C. Surrounding the nanophotonic cavity within the dilution refrigerator is a superconducting vector magnet, which enables the application of a low-noise magnetic field at arbitrary angles. At typical magnetic field strengths around 0.5 T, the electron-spin qubit operates at a frequency of approximately 12 GHz. The nuclear-spin qubit operates at around 30 MHz, determined by the ^{29}Si-electron hyperfine coupling strength.

The ability to adjust the magnetic field and tune the cavity position via gas-tuning allows for different modes of operation. In the single photon generation regime, further detailed in Chapter 3, the magnetic field is misaligned with the SiV center's symmetry axis, allowing spin-flipping optical transitions[48]. Simultaneously, the cavity is tuned into resonance with the SiV center to maximize photon extraction efficiency.

In the entanglement generation regime, discussed in Chapter 4, the magnetic field is aligned with the SiV center's symmetry axis, leading to highly cyclical spin-conserving transitions $f_{\downarrow_e\downarrow_e}$ and $f_{\uparrow_e\uparrow_e}$. Additionally, the cavity is detuned from the SiV center's optical frequency, resulting in a high-contrast reflection spectrum, as shown in Fig. 2.3 b. Probing at the point of maximum reflectance contrast f_Q between $|\downarrow_e\rangle$ and $|\uparrow_e\rangle$ yields highly spin-dependent reflection. An optical pulse at frequency f_Q is reflected with high probability if the electron spin is in the $|\uparrow_e\rangle$ state. Conversely, if the electron spin is in the $|\downarrow_e\rangle$ state, the optical pulse is transmitted to the unprobed cavity port, resulting in little to no reflection. This spin-dependent reflectance contrast enables single-shot spin-state readout and is the underlying mechanism of the spin-photon entangling gates discussed in Chapter 4. Thus, the strong coupling between the SiV center's electron spin and the cavity mode is a key

requirement for using the electron spin as a communication qubit capable of distributing quantum information across a network.

In summary, SiV centers coupled to nanophotonic cavities enable deterministic interactions between itinerant photons and an optically stable emitter, and efficient coupling to a fiber network. This platform also allows for direct MW and RF control of the electron spin, acting as optically active communication qubits, and the nuclear spin, acting as memory qubit. The ability to work in different magnetic field regimes and cavity detunings allows for flexible network node operation. The remaining chapters will demonstrate this versatility by demonstrating high-efficiency single photon generation and entanglement distribution through a 2-node quantum network.

3

Efficient Source of Shaped Single Photons Based on an Integrated Diamond Nanophotonic System

3.1 Introduction

Single optical photons play an essential role in quantum information tasks ranging from quantum communication [16] to measurement-based quantum computing [66,67]. Many protocols in quantum communication use single photons as information carriers between remote locations since photons experience little decoherence while propagating in an optical fiber or free space over long distances. An efficient, scalable source of single photons is therefore extremely useful in quantum information science and technology [68,69].

The most promising approaches for realizing single-photon sources are based on single atoms, ions [70,71,72], or artificial atoms [73,74,75] coupled to optical cavities. The underlying idea is that by promoting an atom to its excited state in a controlled way, only one photon is emitted per excitation cycle. Meanwhile, the encapsulating optical cavity ensures a high probability of photon collection into a well-defined optical mode. Numerous state-of-the-art demonstrations of single-photon sources have utilized solid-state, cavity-integrated self-assembled quantum dots [76,77,78,68,79], which have recently been used in an experiment demonstrating in-fiber single-photon detection efficiencies of above 50% [80].

However, in addition to single photons and linear optical elements, key quantum communication applications such as complex quantum networks will eventually require the use of more advanced components such as quantum memories and quantum repeaters to correct loss errors in communication channels [18,81] or serve as a deterministic nonlinearity to enable quantum logic gates between itinerant photons [82,83]. The necessity of integrating single photons with other components of future quantum networks creates additional requirements that many present-day single-photon sources do not meet: control over the photon frequency, bandwidth, and temporal profile. In particular, leading quantum memory systems have limited bandwidths, often on the MHz scale, which

is several orders of magnitude smaller than the bandwidths of typical state-of-the-art single-photon sources[84,85]. While bandwidth-tailored sources have been realized with neutral-atoms[86], trapped ions[87], and quantum dots[88,89], such systems with high end-to-end efficiencies, compatibility with scalable device fabrication, and photonic integration have yet to be demonstrated.

3.2 Single photon creation using SiV centers

In this chapter, we present a versatile, fiber-coupled single-photon source based on a silicon-vacancy center in diamond which features high efficiency, purity, temporal control, integrability, and access to auxiliary spin memory registers. It can also directly interface with existing quantum memories, enabling future compatibility with repeater-based quantum networks as well as protocols for generation of streams of entangled photonic graph states, which are key resources in rapid one-way quantum communication and measurement-based quantum computation protocols[90,91,92,93,94,95].

Our system consists of a single negatively charged silicon-vacancy center (SiV) in a diamond nanophotonic cavity. The SiV is an inversion-symmetric point defect which features an optically accessible quantum memory that can be embedded in nanofabricated structures while maintaining excellent spin and optical coherence[51,96]. Our cavity-quantum electrodynamics (CQED) system exhibits strong light-matter coupling, characterized by the single-photon Rabi frequency and cavity and atomic energy decay rates $\{g, \kappa, \gamma\} = 2\pi \times \{6.81\,\text{GHz}, 329\,\text{GHz}, 0.1\,\text{GHz}\}$, resulting in a cooperativity of $C \approx 6$, see Appendix A.1.4. Unlike in previous experiments where the magnetic field was oriented along the main symmetry axis of the SiV, we apply a magnetic field nearly orthogonal to the SiV's symmetry axis, giving rise to a four-level system corresponding to the ground ($|\downarrow\rangle$, $|\uparrow\rangle$) and optically excited ($|\downarrow'\rangle$, $|\uparrow'\rangle$) states of the SiV's electronic hole spin[48,57]. The orthogonal field orientation results in spin-flipping optical transitions becoming allowed, hence enabling fast spin initialization and photon generation[49,97].

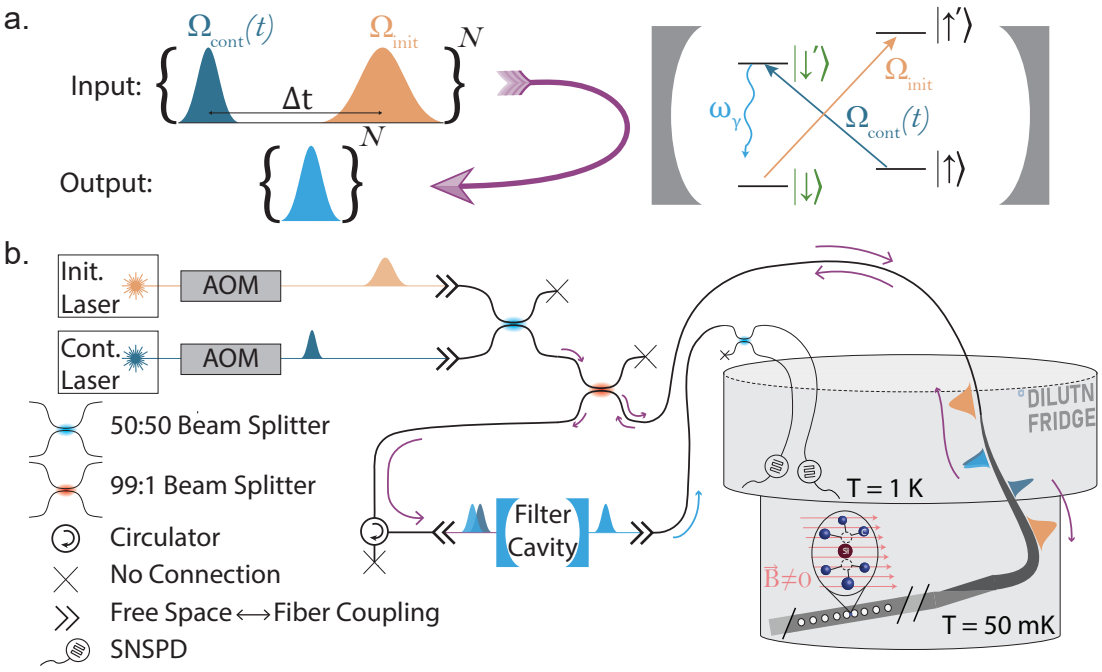


Figure 3.1: (a) Photon Creation Schematic. The four-level system of the SiV spin is coherently driven by alternating initialization (Ω_{init}) and photon generation (Ω_{cont}) optical pulses, producing a train of temporally shaped photons which are efficiently collected with an overcoupled nanophotonic cavity. (b) Measurement Setup Schematic. A nanophotonic cavity containing an SiV is cooled to 50 mK in a dilution refrigerator and pumped to coherently create single, arbitrarily-shaped photons. Pump pulses are shaped using an acousto-optic modulator, and pump light is filtered out of the single-photon stream by a free space Fabry--Pérot cavity.

The protocol for single-photon generation in this system is illustrated schematically in Fig. 3.1a. First, the four-level system is initialized in $|\uparrow\rangle$ by optically pumping the spin flipping transition $|\downarrow\rangle \rightarrow |\uparrow'\rangle$ using a classical driving field with Rabi frequency Ω_{init}. Then, the population is coherently transferred to a single photon using a control pulse with Rabi frequency Ω_{cont} to drive the transition $|\uparrow\rangle \rightarrow |\downarrow'\rangle$. Repeated application of this pulse sequence generates streams of single photons.

The temporal profile of the single-photon wavepackets can be tuned on timescales much longer than the excited state $|\downarrow'\rangle$ lifetime due to the long-lived quantum memory of the SiV spin. In the limit of weak driving $|\Omega_{\text{cont}}| \ll \Gamma$, where Γ is the cavity-enhanced decay rate along $|\downarrow'\rangle \rightarrow |\downarrow\rangle$, the dynamics of the excited state $|\downarrow'\rangle$ adiabatically follows the excitation process, see Section 3.6, and the photon linewidth is limited only by the coherence of the spin-levels $\{|\downarrow\rangle, |\uparrow\rangle\}$ and the control laser's linewidth, rather than the intrinsic lifetime of the SiV excited state $|\downarrow'\rangle$. By modulating the strength and shape of the control pulse $\Omega_{\text{cont}}(t)$, we temporally shape the single photon.

The schematic of our experimental setup is shown in Fig. 3.1b. Devices are placed in a dilution refrigerator at $T \approx 50$ mK to reduce the population of phonons which cause thermal mixing between orbital states[49,98]. This extends the coherence of the ground-state spin, enabling generation of temporally longer photon pulse shapes. Optical control pulses are delivered, and single photons are collected via a tapered optical fiber, which is coupled to the device[56]. On the return path, the generated single photons are filtered from the control pulses by a free space Fabry–Pérot cavity (linewidth = 160 MHz, finesse = 312) before being detected by superconducting nanowire single-photon detectors (SNSPDs).

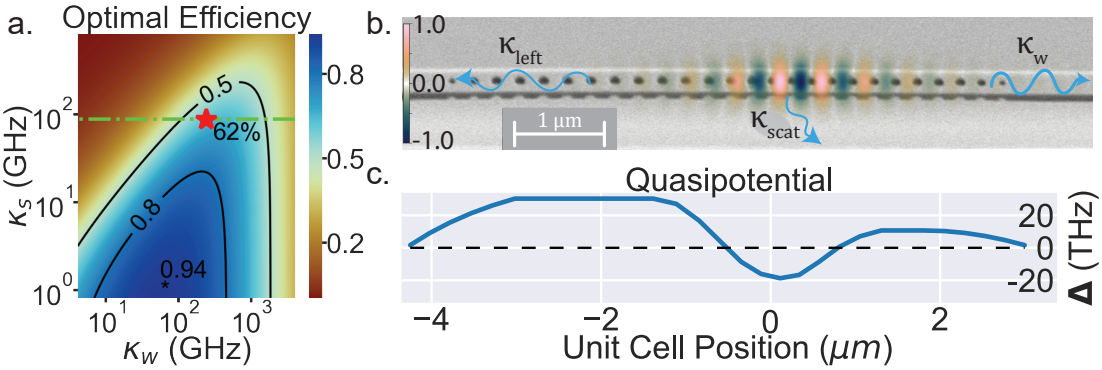


Figure 3.2: (a) Photon extraction efficiency is shown in the color plot as a function of cavity-waveguide coupling κ_w and unwanted cavity loss rate κ_s. Contours aid readability of color map. Optimal extraction efficiency is maximized by trading off atom-photon interaction probability, proportional to $(\kappa_s + \kappa_w)^{-1}$, for a higher cavity-waveguide coupling rate κ_w. The dashed-dot line cut corresponds to $\kappa_s = 89$ GHz, the unwanted loss rate of this device, which is determined by fabrication imperfections. The red star highlights this device with waveguide coupling rate $\kappa_w = 240$ GHz, which is nearly optimal for the given κ_s. (b) A scanning electron micrograph (SEM) of the nanophotonic cavity is overlaid with the simulated electric field, and loss rates are labeled, where $\kappa_s = \kappa_{scat} + \kappa_{left}$. (c) The simulated quasipotential shape of the cavity, see Appendix A.1.1, shows that there is a lower and shorter potential barrier on the weak mirror side. This corresponds to the coupling to the right waveguide being the dominant loss rate ($\kappa_w \gg \kappa_s$).

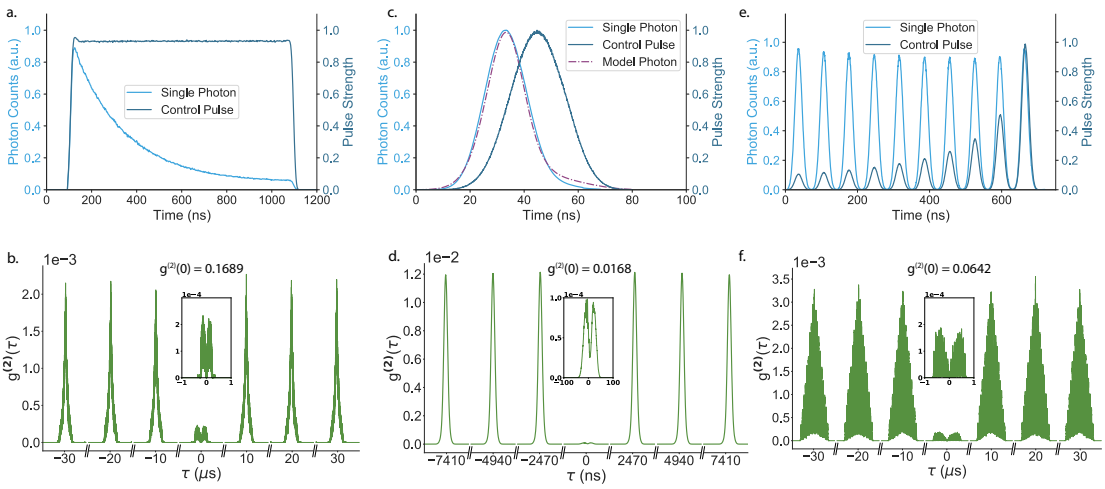


Figure 3.3: Pulse-shaped single-photon generation. Upper panels (a), (c), (e) display the temporal profile of the coherent control pulse and detected single photon. (a) A square control pulse produces an exponentially decaying photon. (b) A Gaussian single photon. (c) A single photon distributed over ten time bins (e). Lower panels (b), (d), (f) display the normalized second order correlation of photon arrivals for the exponential, Gaussian, and ten peaked photons respectively. The insets show a zoomed-in window around $\tau = 0$, which is integrated to calculate $g^{(2)}(0)$.

3.3 Single-sided cavities for maximal efficiency

In order to maximize the photon collection efficiency from the emitter, we implement a novel asymmetric nanophotonic cavity design which strikes a balance between high quality factor of the cavity and strong waveguide damping. In this design, for a given unwanted cavity loss rate κ_s set by fabrication imperfections, there is an optimal choice of waveguide coupling κ_w (Fig. 3.2a). We achieve this optimal trade-off in the asymmetric diamond nanophotonic cavity as pictured in the scanning electron micrograph (SEM) of Fig. 3.2b, which preferentially sends light to the coupling waveguide (i.e. to the right side).

These devices are designed using the analogy between a massive particle tunneling through a potential barrier and the evanescent decay of a photon in a photonic band gap[99]. The asymmetric "quasipotential" for a photon in this device is shown in Fig. 3.2c. It illustrates both the preferential coupling to the measurement port through the lower and narrower barrier on the right side of the cavity as well as a deep well needed for the tight confinement of the optical mode. The simulated electric field overlay in Fig. 3.2b illustrates this wavelength scale confinement (mode volume = 0.67 $\left(\frac{\lambda}{n}\right)^3$). An in-depth discussion of the new photonic crystal cavity design techniques used here is provided in Appendix A.1.

3.4 High-efficiency generation of shaped single photons

We demonstrate generation of bandwidth-tailored photons with this platform in Fig. 3.3. We start by applying a 1 μs square pump pulse (Fig. 3.3a), and observing an exponentially shaped emitted photon, directly illustrating the optical pumping dynamics from $|\uparrow\rangle$ into $|\downarrow\rangle$ expected from a time-independent pump pulse. The photon duration of $\sim$ 1 μs compared to the $\sim$ 1 ns excited state lifetime highlights the ability of this protocol to generate narrow-bandwidth photons, which is independently verified using a separate narrow filter cavity with linewidth below 5 MHz, see Appendix

A.2. To ensure the presence of only a single photon in each wavepacket, we measure the second order correlation, $g^{(2)}$, of the generated photon stream by using a beam splitter and recording the arrival times of photons on a pair of SNSPDs. The results of these measurements are shown in the lower panels of Fig. 3.3. A value of $g^{(2)}(0) = 0.1689 < 0.5$ (Fig. 3.3b) of the exponentially shaped photon confirms the quantum nature of the measured state of light and the presence of a single excitation.

Next, we apply shorter and more powerful Gaussian control pulses to create Gaussian single photons with full-width half-maxima of ~ 20 ns (Fig. 3.3c) and observe a substantially reduced $g^{(2)}(0) = 0.0168$ (Fig. 3.3d). We note that photons of this approximate duration are optimal for interfacing with existing SiV quantum memories[64].

We confirm our understanding of the system using a density matrix model, see Section 3.7.1, to predict the photon shapes resulting from the applied Gaussian control pulse. Fig. 3.3c confirms that our model matches the measured photon shape well. By inverting this model, we can calculate the control pulse $\Omega_{\text{cont}}(t)$ required to generate arbitrarily shaped photon wavepackets. For example, in Fig. 3.3e, we demonstrate a ten-peaked single photon, which could be useful for time-binned multiplexing[64] and efficient high-dimensional quantum communication[100,101]. Auto-correlation measurements again demonstrate the single-photon nature of the ten-peaked photon with a low $g^{(2)}(0) = 0.0642$. The difference in single-photon purity between the three generated photon shapes can be attributed to optically-induced heating, which results in a reduced spin lifetime and increased value of $g^{(2)}(0)$ for longer-duration photons, see Appendix A.4.2.

Next, we measure the total system efficiency by generating short Gaussian photons (as in Fig. 3.3c) continuously over a 24 hour period. The repetition rate of the pump pulses is 405 kHz. We record the number of consecutive n-photon streams detected (Fig. 3.4) as a proxy for the complexity of multi-photon states that are necessary for implementation of quantum information protocols such as one-way quantum communication or computing with photonic cluster states[90,91,92,93,94,95].

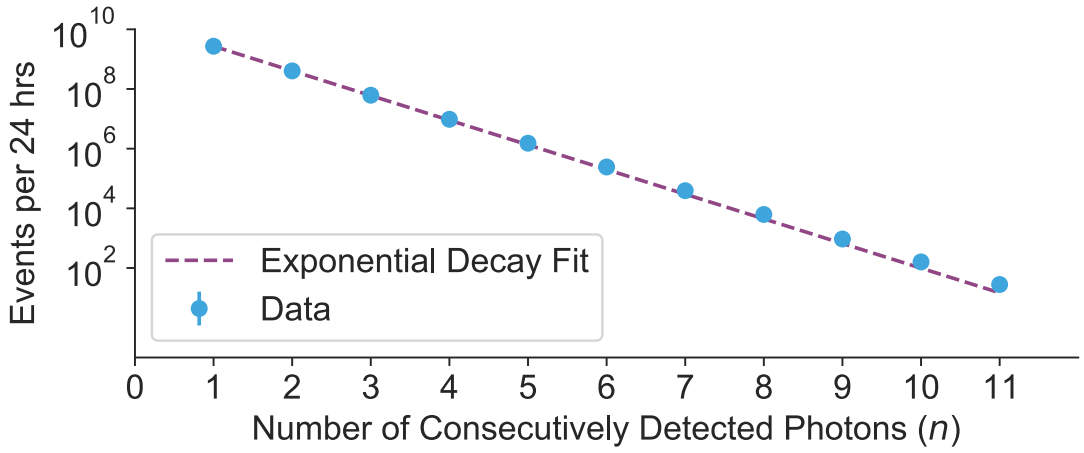


Figure 3.4: Statistics of consecutive n-photon streams detected during a 24-hour acquisition at a 405 kHz repetition rate and 57% average duty cycle, showing detection of up to 11 photons in a row. Exponential decay fit indicates a total source-to-detector efficiency of 14.9%.

Notably, the experiment was operating autonomously during this 24-hour run. Our experiment control software [102] automatically handles SiV ionization and spectral diffusion events, as well as filter cavity locking (see Appendix A.2), making this a realistic demonstration of a practical single-photon source.

The exponential decay fit to the n-photon event rates reveals a single-photon detection efficiency of 14.9%, see Appendix A.3.1. This decrease compared to the ideal photon extraction efficiency of 62% is primarily due to losses in the filtering setup (0.5-0.6), waveguide-fiber coupling efficiency (0.7), and finite detuning of the cavity, see Appendix A.2.3. Despite these extra losses, this single-photon efficiency is competitive with state-of-the-art single-photon sources [76,103,68]. A single-photon detection rate of 31 kHz is achieved, indicating an average duty cycle of 57%, which is primarily limited by ionization of the SiV and software overhead, see A.3.2.

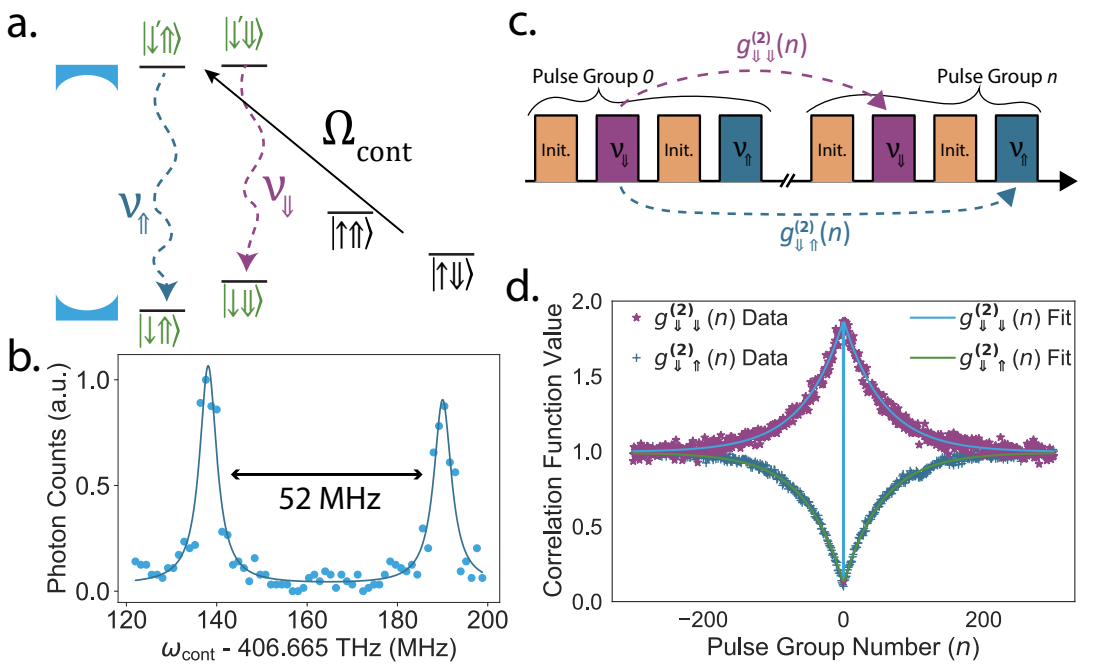


Figure 3.5: Hyperfine splitting due to the ^{29}Si nuclear spin (a) gives rise to a four-level ground state manifold. Pumping on the electron-spin flipping transition with Ω_{cont} results in the generation of photons with two nuclear-state dependent frequencies $\nu_{\Uparrow}$ and $\nu_{\Downarrow}$. (b) Sweeping the control pulse frequency selectively tunes $\nu_{\Uparrow}$ and $\nu_{\Downarrow}$ into resonance with the filter cavity, which enables the measurement of the spectrum of the emitted photons. (c) Pulse sequence for attempting to measure either two consecutive photons at nuclear-state dependent frequencies $\nu_{\Downarrow}$ and $\nu_{\Downarrow}$ or at nuclear-state dependent frequencies $\nu_{\Downarrow}$ and $\nu_{\Uparrow}$. (d) (Purple) $g_{\Downarrow\Downarrow}{}^{(2)}(\tau)$ auto-correlation measurements of the photons emitted at $\nu_{\Downarrow}$ show antibunching at zero time delay, and bunching after emission of 113.8 ± 3.8 photons (1.48 ms timescale). (Blue) $g_{\Downarrow\Uparrow}{}^{(2)}(\tau)$ cross-correlation function for the two consecutively emitted photons at $\nu_{\Uparrow}$ and $\nu_{\Downarrow}$ shows anti-bunching after emission of 110.6 ± 2.4 photons, suggesting that the nuclear polarization is preserved for repeated generation of up to 110 photons.

3.5 Towards generation of multi-photon entangled states

As a first step toward generation of spin-photon entangled states and more complex multi-photon entangled states, we next explore the light-matter interface with the auxiliary nuclear spin memory associated with the ^{29}Si isotope. The hyperfine coupling between the electronic hole spin and the nuclear spin additionally splits the electronic-hole Zeeman ground state manifold creating four levels in the ground-state manifold (Fig. 3.5a). As a result, the ^{29}SiV system can emit photons with two nuclear spin dependent photon frequencies, $\nu_{\Uparrow}$ and $\nu_{\Downarrow}$. Such a system can be used to generate complex multi-photon entangled states such as cluster states or graph states, as proposed in [93,95], by coherently manipulating the nuclear state in between emissions of subsequent photons.

In order to probe the nuclear spin dependent emission frequency of a cavity-integrated ^{29}SiV, we filter the single-photon signal using a significantly narrower 5 MHz linewidth filter cavity, locked close to the $|{\downarrow}'\rangle \rightarrow |{\downarrow}\rangle$ transition. The photons are generated via the same scheme as before, whereby a single initialization pulse is used to initialize the electron regardless of the initial nuclear spin state due to the small hyperfine splitting as compared to the optical transition bandwidth. The filter cavity frequency is held constant while the frequency of the pump laser is swept tuning the frequency of the emitted photons. This selectively tunes $\nu_{\Uparrow}$ and $\nu_{\Downarrow}$ into resonance with the filter cavity, enabling the measurement of the spectrum of the emitted photons. Two narrow peaks are observed in the detected single-photon spectrum with a splitting of 52 MHz (Fig. 3.5b), as expected from the hyperfine splitting from the ^{29}Si nuclear spin [54].

An initial step toward generating multi-photon states with entanglement mediated by the ^{29}SiV nuclear spin is to show that multiple photons can be generated while preserving the nuclear spin state. Therefore, we measure correlations between subsequently emitted photons at the two different nuclear spin dependent emission frequencies, $\nu_{\Uparrow}$ and $\nu_{\Downarrow}$ (Fig. 3.5c). We measure the degree of second-order correlations $g^{(2)}_{\Downarrow\Downarrow}(\tau)$ of photons emitted at frequency $\nu_{\Downarrow}$, observing bunching

on long timescales. We then measure the intensity cross-correlation ${g_{\Downarrow\Uparrow}}^{(2)}(\tau) = \langle I_{\Downarrow}(t) I_{\Uparrow}(t+\tau)\rangle / \langle I_{\Downarrow}(t) I_{\Uparrow}(t)\rangle$, where $I_{\Uparrow}$ and $I_{\Downarrow}$ are the intensities of the $\nu_{\Uparrow}$ and $\nu_{\Downarrow}$ emissions, respectively, and observe anti-bunching on the same timescale. These measurements indicate a 16-fold higher probability of detecting subsequently emitted photons at the same frequency, as opposed to opposite frequencies.

The bunching (antibunching) in $g^{(2)}_{\Downarrow\Downarrow}(\tau)$ (${g_{\Downarrow\Uparrow}}^{(2)}(\tau)$) decays after emission of 113.8 ± 3.8 (110.6 ± 2.4) photons. We attribute this decay to relaxation of the nucleus due to the single-photon generation process. Relaxation of the nucleus after emission of 113.8 ± 3.8 photons would correspond to each generated photon inducing a nuclear spin flip with a probability of $(0.9 \pm 0.03)\%$. These measurements directly demonstrate that classical correlations between the ^{29}Si nuclear spin state and the frequency of the emitted photon can persist for more than 100 consecutively emitted photons, making this a promising approach for the generation of large-scale photonic graph states[95].

Our experiments demonstrate an on-demand source of streams of shaped photons generated from a silicon-vacancy center in an asymmetric nanophotonic cavity in diamond. The challenge of producing a nanophotonic cavity in diamond with arbitrary coupling ratios was resolved through the development of a quasipotential design heuristic, which we believe will be of general use to the nanophotonics community. We showed that the system can generate single photons with highly tunable temporal wavepackets and high spectral purity, detecting streams of up to 11 sequential photons at experimentally useful rates due to a high source-to-detector efficiency and efficient fiber-nanophotonic integration. Given the measured $g^{(2)}(0) = 0.0168$, we estimate this source would provide more than a thirty-fold improvement in the single-photon detection rate when used as a replacement for a weak coherent source with equivalent two-photon detection infidelity, see Appendix A.3.3. Furthermore, this advantage results in an exponential improvement for higher n-photon stream events, as demonstrated by the detection of 28 total 11-photon events in a 24 hour period, which is comparable to state-of-the-art[104].

Additionally, this single-photon source should enable the generation of multi-photon entangled states when efficiently interfaced with a second cavity-coupled SiV[64], which would be used as a quantum memory to deterministically entangle subsequent photons[95]. By demonstrating classical correlations between the built-in ^{29}Si nuclear spin state and emitted photon frequency, we also illustrate the possibility to directly generate streams of entangled photons mediated by nuclear memory. In order to demonstrate quantum correlations (i.e. entanglement) between nuclear spin and photon frequency, additional coherent control of the nucleus would be necessary, which should be possible using RF fields supplied by on-chip coplanar waveguides[51,96]. Moreover, in order to realize large entangled states, mitigation of ^{29}Si memory decoherence arising from heating, which shortens the electron lifetime, will be required (see Appendix A.4.2).

This work builds on our previous demonstration of the SiV-based quantum memory node[64]. The photons generated by our source can be bandwidth and wavelength matched to existing SiV-nanophotonic quantum memory devices, which will be required for complex quantum networking schemes involving stationary repeaters or quantum memories. Combined with the demonstrated ability to create large multi-photon streams on demand, this method should enable the production and detection of high photon number linear cluster states with only moderate improvements to the setups demonstrated here and in[64]. For these reasons, our platform demonstrates promise as a versatile single-photon source which can be interfaced with quantum memories for the realization of quantum networking and quantum information processing tasks.

3.6 Theoretical description of single-photon generation

To gain intuition for single-photon generation by slow optical pumping, we model the SiV as a Λ-system coupled to a continuum of modes, neglecting the coupling to the nanophotonic cavity for now. In the rotating frame of the laser frequency ν of the control pulse, and by making the rotating

frame approximation, we can express the system Hamiltonian as

$$H = -\Delta \left|\downarrow', 0\right\rangle \left\langle\downarrow', 0\right| - \Omega \left|\downarrow', 0\right\rangle \left\langle\uparrow, 0\right| + \sum_k \left[\omega_k \left|\downarrow, 1_k\right\rangle \left\langle\downarrow, 1_k\right| - g_k \left|\downarrow', 0\right\rangle \left\langle\downarrow, 1_k\right|\right] + \text{h.c} \quad (3.1)$$

Here, Δ is the detuning of the control pulse from the $|\uparrow\rangle \rightarrow |\downarrow'\rangle$ transition, k indexes the environmental photon modes with energies ω_k (in the rotating basis) expressed as $\omega_k = \nu_k - \nu - \omega_{\uparrow\downarrow}$, with ν_k being the frequency of the environmental photon and $\omega_{\uparrow\downarrow}$ being the energy splitting between the $|\downarrow\rangle \rightarrow |\uparrow\rangle$ transition, and g_k is the single photon Rabi frequency.

Applying the Wigner-Weisskopf approximation for spontaneous emission [105] and writing out the equations of motion for the diagonal density-matrix element $\rho_{\downarrow',\downarrow'} = \left|\downarrow', 0\right\rangle \left\langle\downarrow', 0\right|$, $\rho_{\uparrow,\uparrow} = \left|\uparrow, 0\right\rangle \left\langle\uparrow, 0\right|$, we get

$$\dot{\rho}_{\uparrow,\uparrow} = i\Omega^* \quad (3.2)$$

$$\dot{\rho}_{\downarrow',\downarrow'} = i\Delta\rho_{\downarrow',\downarrow'} + i\Omega(t)\rho_{\uparrow,\uparrow} - \gamma\rho_{\downarrow',\downarrow'} \quad (3.3)$$

$$(3.4)$$

With the spontaneous emission rate

$$\gamma = 2\frac{\omega_{13}^3 |\mu_{\downarrow\rightarrow\downarrow'}|^2}{3\pi\varepsilon_0\hbar c^3} \quad (3.5)$$

Here, $\mu_{\downarrow\rightarrow\downarrow'}$ is the transition dipole element for the $|\downarrow\rangle \rightarrow |\downarrow'\rangle$ transition. We now assume that we drive the $|\uparrow\rangle \rightarrow |\downarrow'\rangle$ transition on resonance ($\Delta = 0$) and get

$$\dot{\rho}_{\downarrow',\downarrow'} = i\Omega(t)\rho_{\uparrow,\uparrow} - \gamma\rho_{\downarrow',\downarrow'} \quad (3.6)$$

If we now assume a time-independent Rabi drive $\Omega(t) = \Omega$ with $\Omega \ll \gamma$, we can adiabatically eliminate the time dynamics of the exited state $|\downarrow', 0\rangle$ and can write

$$\rho_{\downarrow',\downarrow'} = \frac{i\Omega}{\gamma}\rho_{\uparrow,\uparrow} \tag{3.7}$$

It should be noted that the adiabaticity condition can easily be fulfilled, since $\Omega \propto \mu_{\uparrow\to\downarrow'}$, and the cross transition $|\uparrow\rangle \to |\downarrow'\rangle$ is much weaker that the spin conserving transition $|\downarrow\rangle \to |\downarrow'\rangle$: $|\mu_{\downarrow\to\downarrow'}|^2 \gg |\mu_{\uparrow\to\downarrow'}|^2$.

Assuming $\rho_{\uparrow,\uparrow}(t = 0) = 1$, one can now define a modified fluorescence rate Γ_{fl} as

$$\Gamma_{\text{fl}} = \gamma|\rho_{\downarrow',\downarrow'}|^2 = \gamma\left(\frac{|\Omega|^2}{\gamma^2}\right) \ll \gamma \tag{3.8}$$

The photon emission now occurs at timescales dictated by Γ_{fl}, which are much slower than the spontaneous emission rate γ. Notably, the timescales are only limited by the coherence properties of the $|\uparrow\rangle, |\downarrow\rangle$ qubit levels and the noise of the drive laser.

So far, this treatment does not explicitly take the coupling between the SiV center and the nanophotonic cavity into account. Assuming a cavity decay rate κ, the Purcell regime [55] is characterized by:

$$\kappa \gg g \gg \gamma \tag{3.9}$$

In this regime, the linewidth of an SiV close to the cavity's resonance frequency broadens and becomes $\Gamma = (C + 1)\gamma$, with $C = 4\frac{g^2}{\kappa\gamma}$. Working with relatively broad cavities ($\kappa \approx 2\pi \times 300$ GHz) facilitates the satisfaction of Eq. (3.9) and motivates borrowing the intuition for scattering into a continuum of modes. For $C > 1$, the adiabaticity condition is thus relaxed to $\Omega \ll \Gamma$. Using our simulation results for the Gaussian photon, we can independently verify that the adiabaticity

condition is met, see Fig. 3.7 (b).

3.7 Density matrix simulations of photon generation

3.7.1 Model Setup

In the rotating frame of the frequency of the control pulse, we can express our Hamiltonian in the joint atom-cavity basis:

$$\mathbf{H}_S = \Delta \left|\downarrow', 0\right\rangle \left\langle\downarrow', 0\right| + (\Delta - \Delta_C) \left|\downarrow, 1\right\rangle \left\langle\downarrow, 1\right| + \Omega(t) \left|\downarrow', 0\right\rangle \left\langle\uparrow, 0\right| + g \left|\downarrow, 1\right\rangle \left\langle\downarrow', 0\right| + \text{h.c.} \quad (3.10)$$

Here, Δ is the detuning of the control pulse from the $|\uparrow\rangle \rightarrow |\downarrow'\rangle$ transition, Δ_C is the detuning between the $|\uparrow\rangle \rightarrow |\downarrow'\rangle$ transition and the cavity resonance, $\Omega(t)$ is the time-dependent Rabi drive induced by the control pulse, g is the coupling rate to the cavity mode, and $\hbar$ is set to 1.

The following Lindblad collapse operators are used to describe the interaction between the system and the environment:

$$\mathbf{L}_1 = \sqrt{\kappa} \left|\downarrow, 0\right\rangle \left\langle\downarrow, 1\right|, \mathbf{L}_2 = \sqrt{\gamma} \left|\downarrow, 0\right\rangle \left\langle\downarrow', 0\right|, \mathbf{L}_3 = \sqrt{\gamma_t} \left|\downarrow, 0\right\rangle \left\langle\uparrow, 0\right| \quad (3.11)$$

Here, κ is the rate at which the photon leaks out of the cavity. For the purpose of this model, we assume that we collect all photons emitted from the cavity, such that it is not necessary to distinguish between the cavity decay rate κ and the waveguide decay rate κ_w. γ is spontaneous emission rate for the optical $|\uparrow\rangle \rightarrow |\downarrow'\rangle$ transition, and γ_t is the decay rate within the spin-qubit. The level diagram for this system is shown in fig. 3.6.

We can now use the Lindblad-form of the Master equation to describe the time-dynamics of the

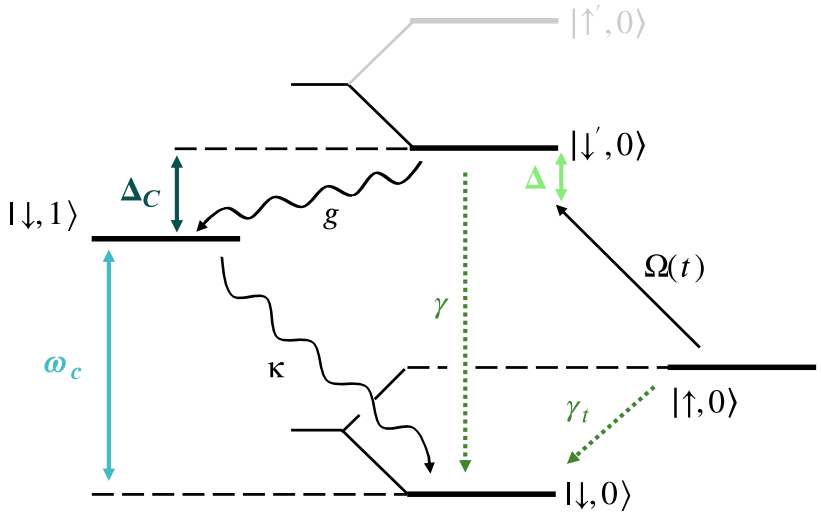


Figure 3.6: Level diagram of our system whose dynamics are encoded in Eq. 3.10. The Zeeman interaction lifts the degenracy of the $|\uparrow\rangle$ and $|\downarrow\rangle$ ($|\uparrow\rangle'$ and $|\downarrow\rangle'$) states.

the density operator of the system:

$$\dot{\rho} = -i[\mathbf{H}_S, \rho] + \sum_i (\mathbf{L}_i \rho \mathbf{L}_i^\dagger - \frac{1}{2}\mathbf{L}_i^\dagger \mathbf{L}_i \rho - \frac{1}{2}\rho \mathbf{L}_i^\dagger \mathbf{L}_i) \tag{3.12}$$

This master equation can be numerically evaluated using Python's `QuTip` package [106], an open-source software for simulating the dynamics of open quantum systems.

3.7.2 Simulation results: photon pulseshape

We encode our effective Hamiltonian (Eq. 3.10) and collapse operators (Eq. 3.11) with the appropriate parameters and simulate how the system evolves when being driven by an arbitrary time-dependent Rabi pulse $\Omega(t)$. For the example of the Gaussian photon depicted in the main text, fig. 3 (b), we can parameterize the Rabi drive as a Gaussian pulse:

$$\Omega(t) = \Omega_0 \exp\left[-\frac{1}{2}\left(\frac{t-\mu}{\sigma}\right)^2\right] \tag{3.13}$$

Variable	Description	Value
$\Delta_C/2\pi$	SiV - cavity detuning	19.88 GHz
$g/2\pi$	Single photon Rabi frequency	6.81 GHz
$\Omega_0/2\pi$	Rabi drive peak amplitude	194 MHz
$\kappa/2\pi$	FWHM of nanophotonic cavity	328 GHz
$\gamma/2\pi$	Spontaneous emission rate for $\|\uparrow\rangle \rightarrow \|\downarrow'\rangle$ transition	100 MHz
$\gamma_t/2\pi$	Decay rate of spin qubit	50 kHz

Table 3.1: Numerical vales of model parameters used in simulations results shown in Fig. 3.7

Using this expression for $\Omega(t)$, we can use the `mesolve` function in `QuTip` to solve the master equation and obtain the state of the system ρ at each given time step. To extract the intensity profile of the emitted photon, we then find $\sqrt{\kappa}\,\langle\downarrow,1|\rho|\downarrow,1\rangle$, where $\langle\downarrow,1|\rho|\downarrow,1\rangle$ is the population of the cavity $|\downarrow,1\rangle$.

This numerical model enables us to design pulse shapes to produce a desired photon waveform. By optimizing over pulse parameters to fit a target photon shape, we can use our dynamical model of the atom-cavity system to predict pulses that will generate a specific photon. We can also use our model to replicate experimentally obtained photon and pulse data, as shown in fig. 3.7 (a). This is accomplished by first fitting photon data to obtain a predicted pulse shape, then inputting the experimental pulse data into our model to generate a photon, and finally averaging the two results. Table 3.1 shows the numerical values of the CQED parameters for the simulation depicted in fig. 3.7.

Figure 3.7 (b) confirms through the results of a density matrix simulation with realistic parameters that the excited state is only slightly populated during the photon generation sequence as expected. The dominance of κ and g over the spontaneous decay rate γ allows coherent population transfer from the spin ground state to the single photon without suffering significant decoherence from γ.

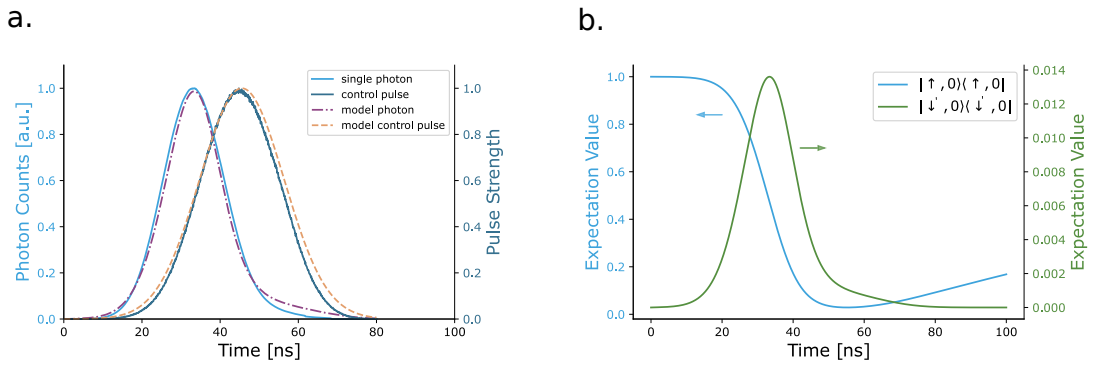


Figure 3.7: (a) Model fit of a Gaussian photon generated from the given pulse, including photon and pulse data also shown in main text fig. 3 (b) Simulated expectation values of operators for the same simulation as in (a). As population is fully transferred out of the initial spin state (blue curve), the population of the excited state (green curve) remains low. Arrows indicate relevant y-axis.

3.7.3 Simulation results for correlation functions

The second order correlation of photon arrivals, $g^{(2)}$, can be calculated using a slightly modified version of the numerical model. Measuring $g^{(2)}$ requires a re-initialization pulse $\Omega'(t)$ that pumps the population from $|\downarrow, 0\rangle$ to an additional energy level $|\uparrow', 0\rangle$. The population is then restored to the initial state $|\uparrow, 0\rangle$ through a spontaneous decay channel at a rate γ. Thus, the Hamiltonian becomes

$$\mathbf{H}_S = \Delta\,|\downarrow', 0\rangle\langle\downarrow', 0| + (\Delta - \Delta_C)\,|\downarrow, 1\rangle\langle\downarrow, 1| + \Omega(t)\,|\downarrow', 0\rangle\langle\uparrow, 0| + g\,|\downarrow, 1\rangle\langle\downarrow', 0| + \Omega'(t)\,|\uparrow', 0\rangle\langle\downarrow, 0| + \text{h.c.} \tag{3.14}$$

and another Lindblad collapse operator $\mathbf{L}_4 = \sqrt{\gamma}\,|\uparrow, 0\rangle\langle\uparrow', 0|$ is added to the calculation. The master equation can then be solved using the Monte Carlo (MC) method, which keeps track of the times at which a photon is emitted from the cavity ($\mathbf{L}_1$). The MC solver is encoded in the `solnmc` function of `QuTip`. Given the pulse sequence of a Gaussian pulse from $|\uparrow, 0\rangle \rightarrow |\downarrow', 0\rangle$, a re-initialization pulse from $|\downarrow, 0\rangle \rightarrow |\uparrow', 0\rangle$, and another Gaussian pulse from $|\uparrow, 0\rangle \rightarrow |\downarrow', 0\rangle$,

photon counts occurring after the initial (expected) photon contribute to the $g^{(2)}$-function. Thus, using the MC simulation results, a histogram of photon arrival times can be compiled. In this histogram, we measure photon arrival times relative to the arrival time of the primary photon. These simulations reproduce the experimental $g^{(2)}$-function, as shown in fig. 3.8.

The MC simulation can furthermore be used to investigate the influence of the qubit decay rate γ_t on the single-photon purity. As shown in Fig. 3.9, increased values of γ_t result in a higher contribution of coincidences for short time delays $\tau \approx 0$. This can be explained by the fact that a high coupling between the two qubit states can result in a re-initialization of the electron in the $|\downarrow\rangle$ state while the control pulse is still applied, which can result in the emission of a photon. Since this is the second photon emitted during the time-window of the first photon, the coincidence counts in this initial time-window around $\tau = 0$ are increased, and the single-photon purity is decreased. This is supported by our measurements, which show a significantly decreased single-photon purity for the exponentially-shaped photon (main text fig. 3 (a)) and the ten-peaked photon (main text fig. 3 (e)), which both are comparatively long compared to the Gaussian-shaped photon. Furthermore, the coincidence counts close to $\tau = 0$ mirror the temporal shape of the primary photon, which is indicative of a secondary photon emission. As discussed in A.4.2, we attribute the enhancement of the γ_t to instantaneous control laser induced heating.

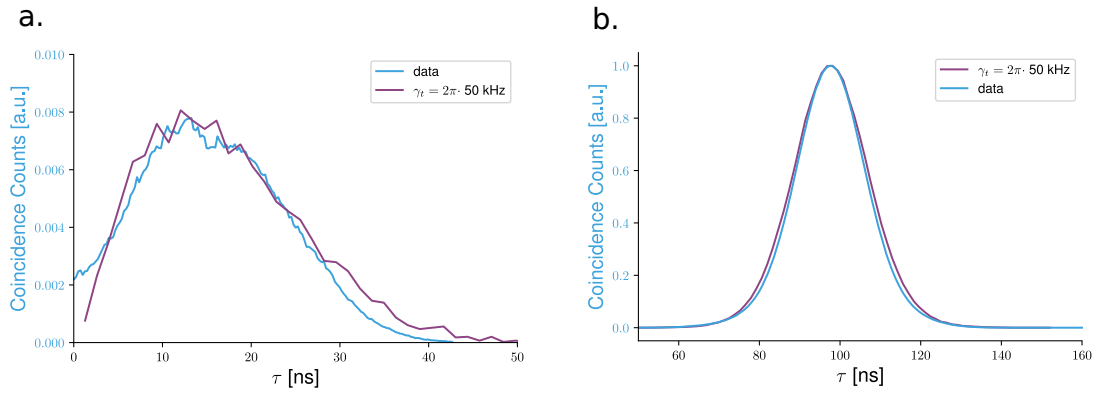


Figure 3.8: Experimental data and model prediction of the $g^{(2)}$ of Gaussian photon arrivals for the $\tau \approx 0$ region (a) and the first pulse region (b).

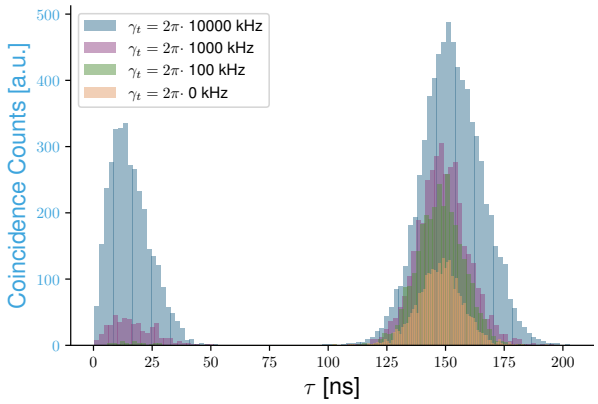


Figure 3.9: Simulated $g^{(2)}$ functions assuming various qubit decay rates γ_t and a control pulse separation of 150 ns. The initial peaks close to $\tau = 0$ are only observable for $\gamma_t \neq 0$ and increase in amplitude for larger γ_t. This is indicative of emissions of secondary photons due to repopulation. The peaks around 150 ns corresponds to the emission due to the second control pulse and also increases in amplitude for larger γ_t, which is again attributable to the emission of secondary photons.

4

Entanglement of Nanophotonic Quantum Memory Nodes in a Telecom Network

Distributing quantum entanglement between quantum memory nodes separated by extended distances [16,107] is a critical element for the realization of quantum networks, enabling potential applications ranging from quantum repeaters [18,19] and long-distance secure communication [9,11]

to distributed quantum computing[20,21] and distributed quantum sensing and metrology[22,23]. Proposed architectures require quantum nodes containing multiple long-lived qubits that can collect, store, and process information communicated via photonic channels based on telecommunication (telecom) fibers or satellite-based links. In particular, the abilities to herald on successful photon arrival events and to detect quantum-gate errors are central for scalable implementations. Since photons and individual matter qubits interact weakly in free space[55], a promising approach to enhance the interaction between light and communication qubits is to utilize nanophotonic cavity quantum electrodynamic (QED) systems, where tight light confinement inside the nanostructure enables strong interactions between the photon and the communication qubit[108,51,109,110]. Furthermore, nanophotonic systems offer a path towards large-scale manufacturing and on-chip electric and optical control integration[111,112,113]. Several experiments demonstrated remote entanglement in systems ranging from neutral atoms[32,33,34,35] and trapped ions[36,37] to semiconductor quantum dots[38] and nitrogen-vacancy (NV) centers in diamond[39,40]. Recently, two atomic ensemble memories have been entangled through a metropolitan fiber network[41,42,43]. However, real-world applications require a combination of efficient photon coupling, long-lived heralded memory, and multi-qubit operations with practical telecom fiber networks, which is an outstanding challenge.

Here, we report the realization of a two-node quantum network between two multi-qubit quantum network nodes constituted by silicon-vacancy (SiV) centers in diamond coupled to nanophotonic cavities and integrated with a telecom fiber network. SiVs coupled to cavities have emerged as a promising quantum network platform, having demonstrated memory-enhanced quantum communication[64] and robust multi-qubit single-node operation[53]. We extend these single-node experiments by demonstrating remote entanglement generation between two electron spins in two spatially separated SiV centers with a success rate up to 1 Hz. Our approach utilizes serial, heralded spin-photon gate operations with time-bin qubits for robust entanglement of separated nodes and does not require phase stability across the link. We further make use of the multi-qubit capabilities

to entangle two long-lived nuclear spins, using integrated error detection to enhance entanglement fidelities and dynamical decoupling sequences to extend the entanglement duration to 1 s. Both entanglement generation techniques rely on the strong light-matter interaction enabled by the SiV's coupling to the nanophotonic cavity. In order to demonstrate the feasibility of deployed quantum networks using our platform, we use bi-directional quantum frequency conversion (QFC) to convert the photonic qubits' wavelength to telecom wavelengths. Building on recently demonstrated compatibility of our platform with bi-directional QFC [114,115], we demonstrate remote entanglement generation through spools of up to 40 km of low-loss telecom fiber. Finally, we combine these techniques to demonstrate entanglement generation through a 35 km-long loop of fiber with 17 dB loss deployed in the Boston area urban environment.

4.1 Two-node quantum network using integrated nanophotonic systems

Our quantum network nodes consist of SiV centers in diamond that reside in individually operated dilution refrigerator setups in separate laboratories (Fig. 4.1 a). By selectively implanting the ^{29}Si isotope into the diamond substrate, each SiV deterministically contains two addressable spin qubits: one electron spin used as a communication qubit, which couples strongly to itinerant photons, and one long-lived ^{29}Si nuclear spin, used as a memory qubit to store entanglement. Under an externally applied magnetic field, Zeeman sublevels define the electronic spin qubits states ($|\downarrow_e\rangle$, $|\uparrow_e\rangle$) and the nuclear spin qubit states ($|\downarrow_n\rangle$, $|\uparrow_n\rangle$) [57,54] (Fig. 4.1 b, left). Microwave (MW) pulses are used to drive the electronic spin-flipping transitions, while radio-frequency (RF) pulses drive the nuclear spin-flipping transitions [53]. The SiV centers are embedded into nanophotonic diamond cavities, which enhance interactions between light and the electron spin [55,83]. The strong emitter-cavity coupling as characterized by the single-photon cooperativity in node A (node B) of 12.4 (1.5) (see Appendix B.2) results in an electron-spin dependent cavity reflectance (Fig. 4.1 b, right) [51]. This can be utilized

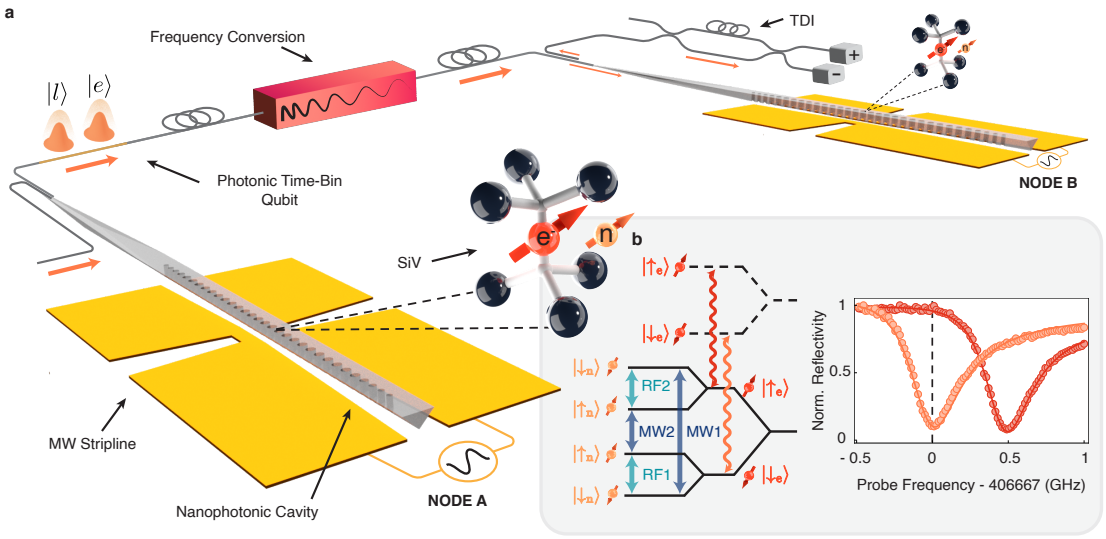


Figure 4.1: A two-node quantum network of cavity-coupled solid state emitters. **a.** Experimental setup. Each SiV is localized in a nanophotonic cavity within an individually operated cryostat held at temperatures below $200\,\mathrm{mK}$ in two separate laboratories. The line-of-sight distance between the two SiVs is $6\,\mathrm{m}$. A gold coplanar waveguide is used to deliver MW and RF pulses to the SiV. Both quantum network nodes are connected via a $\approx$ 20 m long optical fiber and frequency shifting setup to compensate for differences in the optical transition frequencies, or a long telecom fiber link using QFC (see Fig. 4.4 a). The measurement of the photonic time-bin qubit is performed at node B using a time-delay interferometer (TDI), which measures the time-bin qubit in the basis $|\pm\rangle \propto (|e\rangle \pm |l\rangle)$. **b.** Left: Energy levels of ^{29}SiV showing the MW and RF transitions in the two-qubit manifold (blue and turquoise arrows) and the spin-conserving optical transitions (red and orange). Right: The reflection spectrum of node A's cavity QED system shows the electron-spin-dependent cavity reflectance. The dashed line indicates the frequency of maximum reflectance contrast, which is used as the frequency for the electron spin state readout and the photonic entanglement.

to construct a reflection-based spin-photon gate ($e - \gamma$ gate), which contains a sequence of rapid MW gates generating entanglement between the SiV's electron spin and the photonic qubits [51]. Additionally, taking advantage of the strong coupling between the SiV's electron spin and the ^{29}Si nuclear spin, nucleus-photon entanglement can be created using the PHOton-Nucleus Entangling (PHONE) gate as demonstrated recently [53]. The two nodes are either connected directly via a $\approx$ 20 m long optical fiber (Fig. 4.1 a), or via a considerably longer telecom fiber link as discussed below (Fig. 4.4 a).

We use a serial network configuration to generate remote entanglement between the electron

spins in node A and node B, mediated by a time-bin photonic qubit (Fig. 4.2 a). We first use a $e-\gamma$ gate to generate an entangled Bell state between node A's electron spin $|\downarrow_e^A\rangle$, $|\uparrow_e^A\rangle$ and an incoming time-bin photonic qubit $|e\rangle$, $|l\rangle$ [51]. Here, $|e\rangle$ and $|l\rangle$ describe the presence of a photon in the early and late time-bins of the photonic qubit, which are separated by $\delta t = 142$ ns, respectively. The resulting photon-electron Bell state can be described as $|\text{Photon, SiV A}\rangle = (|e\downarrow_e^A\rangle + |l\uparrow_e^A\rangle)/\sqrt{2}$, see Section 4.6. After that, the photonic qubit travels via optical fiber to node B, where a second $e-\gamma$ gate entangles the photonic qubit with the electron spin in node B. In the ideal, lossless case, the resulting state is a three-particle Greenberger–Horne–Zeilinger (GHZ) state:

$$\begin{aligned}|\text{Photon, SiV A, SiV B}\rangle &= (|e\downarrow_e^A\downarrow_e^B\rangle + |l\uparrow_e^A\uparrow_e^B\rangle)/\sqrt{2} \\ &= \left(|+\rangle\,|\Phi_{ee}^+\rangle + |-\rangle\,|\Phi_{ee}^-\rangle\right)/\sqrt{2}.\end{aligned}$$

Here, $|\pm\rangle = (|e\rangle \pm |l\rangle)/\sqrt{2}$ describes two orthogonal superposition states of the photonic time-bin qubit, and $|\Phi_{ee}^{\pm}\rangle = (|\downarrow_e^A\downarrow_e^B\rangle \pm |\uparrow_e^A\uparrow_e^B\rangle)/\sqrt{2}$ describes the maximally entangled Bell states of the two spatially separated electron spins. The photonic qubit is measured in the $|\pm\rangle$-basis using a TDI to herald the generation of an electronic Bell state:

$$|\text{SiV A, SiV B}\rangle = \begin{cases} |\Phi_{ee}^+\rangle\,, & \text{if TDI measures } |+\rangle \\ |\Phi_{ee}^-\rangle\,, & \text{if TDI measures } |-\rangle\,. \end{cases}$$

Note that similar to the previously utilized single-node schemes [51], this method is robust to photon loss, as any losses of photons can be detected by a missing heralding event. Furthermore, the main advantage of our serial scheme is that both the early and late time-bins of the photonic qubit travel through the same path, so no phase or polarization-locking is necessary to guarantee high interference contrast at the TDI. This relaxes the requirements on system stability compared to one-photon

schemes, which typically require an interferometric measurement of two emitted photons traveling through two stabilized paths[40,43,38,35], and avoids the reduction in entanglement rate typically present in two-photon schemes[116,39]. Furthermore, extending the number of network nodes to more than two can be achieved by either connecting more than two nodes in series, or by employing a switch network between multiple nodes to generate pairwise connectivity.

Since cavity-coupled ^{29}SiV centers possess an inhomogeneous distribution of optical transition frequencies of around $\pm$ 50 GHz centered around 406.640 THz (737.2 nm) (see 52 and Section 4.8), the frequency difference between the nodes needs to be coherently bridged. For node B used in this work, for instance, the SiV's optical frequency ω_B is detuned from that of node A (ω_A) by $\Delta_\omega = 13$ GHz. To address this, we prepare the photonic qubit at frequency ω_A and then coherently shift its frequency by Δ_ω after it has interacted with the SiV at node A, either using electro-optic frequency shifting or via bi-directional QFC[114,115].

4.2 Electronic spin entanglement

To demonstrate the basic principles of network operation, we first focus on the nodes connected directly via a $\approx$ 20 m long optical fiber and employ electro-optical frequency shifting (see Section 4.8 for more details). The above protocol is applied using weak coherent states (WCS, with mean photon number $\mu = 0.017$) to encode time-bin qubits. After the TDI measurement heralds the generation of a Bell state, single qubit rotations and subsequent readout of the electron spin at each node implement the measurement of the correlations $\langle \sigma_i^A \sigma_i^B \rangle$, $i \in \{x, y, z\}$, which we abbreviate as XX, YY, and ZZ, respectively. Fig. 4.2 b shows the results of the correlation measurements, from which we extract the fidelities of the resulting electron-electron state with respect to the maximally entangled Bell states $\mathcal{F}_{|\Phi_{ee}^-\rangle} = 0.86(3)$ (if the TDI measured $|-\rangle$), and $\mathcal{F}_{|\Phi_{ee}^+\rangle} = 0.74(3)$ (if the TDI measured $|+\rangle$), unambiguously demonstrating entanglement between the two nodes. The ob-

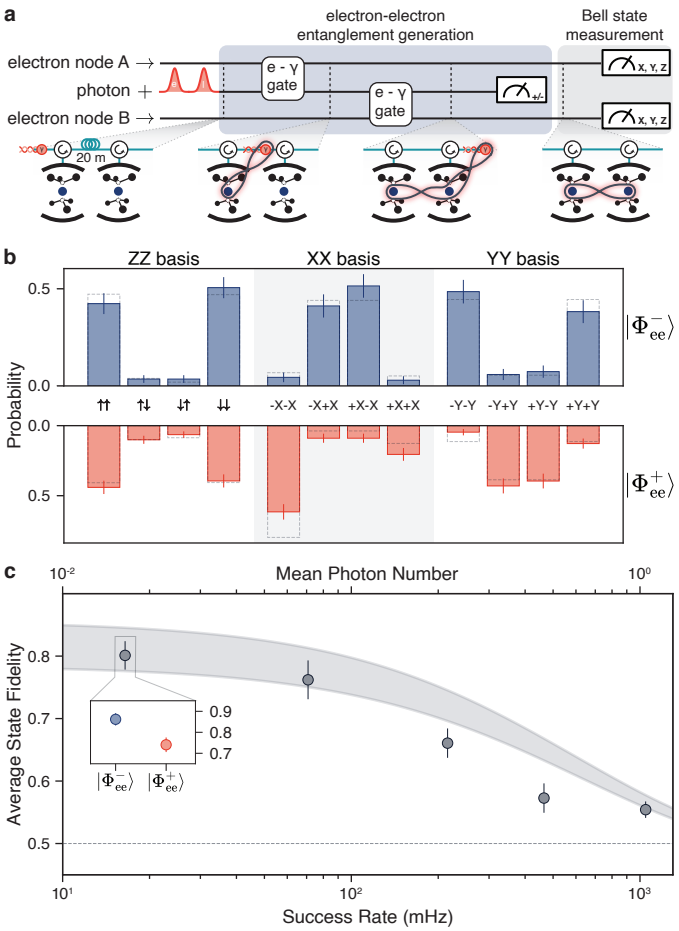


Figure 4.2: Remote entanglement between two electronic spins. **a.** Entanglement generation sequence. A photonic qubit is entangled with the electron spin in node A using the $e-\gamma$ gate. A second $e-\gamma$ gate entangles the photonic qubit with node B, generating a GHZ state among the two electronic qubits and the photonic qubit. A measurement of the photonic qubit in the $|\pm\rangle$ basis heralds the generation of an electronic Bell state $|\Phi^{\pm}_{ee}\rangle$. **b.** Measurement results of Bell state measurement. Measured correlations in the ZZ, XX, and YY bases of the electronic spin corresponding to a Bell state fidelity of $\mathcal{F}_{|\Phi^-_{ee}\rangle} = 0.86(3)$ (blue) and $\mathcal{F}_{|\Phi^+_{ee}\rangle} = 0.74(3)$ (red). Dashed bars show correlations predicted by a theoretical model using independently measured performance parameters of our system. **c.** Sweep of mean photon number of the photonic qubit showing that the success rates can be increased by sending photonic qubits with a higher mean photon number. The average fidelity of the generated $|\Phi^+_{ee}\rangle$ and $|\Phi^-_{ee}\rangle$ states is plotted. Inset shows fidelities of states shown in b. Entanglement is shown to persist above the classical limit (dashed line) for success rates up to $1\,\mathrm{Hz}$. Filled curves show predictions by a theory model using independently measured performance parameters of our system, see Appendix B.5.1. Error-bars in b. and c. are one s.d.

served difference in fidelity is due to one source of infidelity associated with the imperfect reflection contrast of the two cavity-coupled SiVs. This results in reflection of the photonic qubit even when

the electron spin is in the low-reflectivity $|\downarrow_e\rangle$ state. For our system configuration, this type of error accumulates preferentially for the $|\Phi_{ee}^{+}\rangle$ state, which is why $\mathcal{F}_{|\Phi_{ee}^{+}\rangle}$ is consistently lower than $\mathcal{F}_{|\Phi_{ee}^{-}\rangle}$, see Appendix B.3. Further error sources include contributions from 2- or higher photon number Fock states of the WCS used as time-bin photonic qubits. By varying the mean photon number μ in the WCS, we can increase the entanglement generation rate at the cost of reduced fidelity of the generated state. We explore this trade-off in Fig. 4.2 c, where we show that we are able to operate at success rates of 1 Hz while maintaining entanglement.

4.3 Nuclear spin entanglement

Extending remote entanglement to larger distances requires the ability to preserve entanglement long enough such that the heralding signal obtained at node B can be classically relayed to node A. The coherence times of the electron spins in Node A and B are 125 µs and 134 µs, respectively. Assuming classical communication via optical fibers in the telecommunication band, the electron spin's decoherence would limit the distance between the nodes to approximately 25 km. To overcome this limitation, we demonstrate remote entanglement generation between two ^{29}Si nuclei, which are long-lived quantum memories with storage times of over 2 s [53]. Analogously to the generation of electron-electron entanglement, remote nuclear entanglement is mediated by the photonic time-bin qubit (Fig. 4.3 a). Thus, the first step of the remote entanglement generation sequence is creating entanglement between a photonic time-bin qubit and the ^{29}Si nuclear spin at node A. This is achieved using the recently demonstrated PHOton-Nucleus Entangling (PHONE) gate, which only uses microwave pulses to directly entangle the ^{29}Si nuclear spin with the photonic qubit [53], without the need to swap quantum information from electron to nuclear spin. After applying the PHONE gate on the SiV in node A and the photonic qubit, in the ideal limit, their quantum state

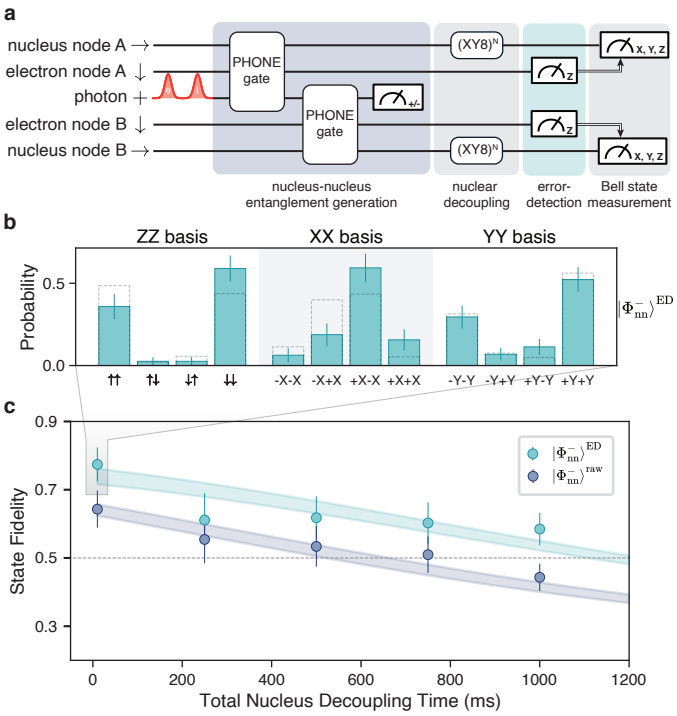


Figure 4.3: Remote entanglement and long-lived storage using nuclear spins. **a.** Entanglement generation and subsequent dynamical decoupling using nuclear spin qubits. Nuclear-nuclear entanglement is created by sequentially entangling a time-bin photonic qubit with the ^{29}Si nuclei at nodes A and B using two PHONE gates. Measurement of the electron spin qubits allows for integrated error detection by flagging MW gate errors occurred during the PHONE gate. **b.** Results of Bell state measurement of $|\Phi^-_{\mathrm{nn}}\rangle$ after performing error detection, resulting in a Bell state fidelity of $\mathcal{F}^{\mathrm{ED}}_{|\Phi^-_{\mathrm{nn}}\rangle} = 0.77(5)$. Dashed bars show correlations predicted by a theoretical model using independently measured performance parameters of our system. **c.** Decoherence protection of remotely entangled nuclear-nuclear Bell states, both with (turquoise) and without (blue) error detection. By performing XY8 dynamical decoupling sequences on the two nuclei, entanglement can be preserved for up to 1 s. Filled curves show predictions by a theory model using independently measured performance parameters of our system, see Appendix B.5.2. The XY8-1 decoupling sequence was used for the datapoint with 10 ms decoupling time while the XY8-128 sequence was used for all other measurements. The dashed line indicates the classical limit. Error-bars in b and c are one s.d.

is:

$$|\text{Photon, SiV A}\rangle = \left(|e\downarrow^A_{\mathrm{n}}\rangle + |l\uparrow^A_{\mathrm{n}}\rangle\right)|\downarrow^A_{\mathrm{e}}\rangle\,/\sqrt{2}.$$

This implies that unless a microwave gate error has occurred, the electron spin is disentangled from the nuclear spin and is in the $|\downarrow^A_{\mathrm{e}}\rangle$ state. Thus, the electron spin can be used as a flag qubit to perform error detection by discarding a measurement when the electron spin is measured in $|\uparrow^A_{\mathrm{e}}\rangle$. By

performing a second PHONE gate between the ^{29}Si nuclear spin of Node B and the time-bin qubit, and by subsequently measuring out the photonic time-bin qubit in the $|\pm\rangle$ basis, the nuclear Bell states $|\Phi^{\pm}_{\mathrm{nn}}\rangle$ are created. Following the entanglement generation, we perform XY8-type decoupling sequences on both nuclei to protect the nuclear-nuclear Bell state from decoherence caused by a quasi-static environment. Fig. 4.3 b shows the probability correlations of the resulting $|\Phi^{-}_{\mathrm{nn}}\rangle$ state using a XY8-1 decoupling sequence with a total nuclear spin decoupling time of 10 ms. After using error detection by discarding measurements where the electronic flag qubit is measured in the $|\uparrow^{A}_{\mathrm{e}}\rangle$ state, the Bell state fidelity is $\mathcal{F}^{\mathrm{ED}}_{|\Phi^{-}_{\mathrm{nn}}\rangle} = 0.77(5)$, which is an improvement from the directly measured value of $\mathcal{F}^{\mathrm{raw}}_{|\Phi^{-}_{\mathrm{nn}}\rangle} = 0.64(5)$ without error detection. Similar to $|\Phi^{+}_{\mathrm{ee}}\rangle$, the generated $|\Phi^{+}_{\mathrm{nn}}\rangle$ state accumulates errors due to imperfect reflectance contrast, see Appendix B for more information. Fig. 4.3 c shows Bell state fidelities for longer total nuclear decoupling times. By performing XY8-128 decoupling sequences, entanglement can be preserved for up to 500 ms, with the application of error detection further extending this to one second.

4.4 Entanglement distribution through 35 km of deployed fiber

Light at the SiV's resonant wavelength (737 nm) experiences a high in-fiber loss of $> 4\,\mathrm{dB\,km^{-1}}$, which limits the range of remote entanglement distribution at this wavelength. In order to make our quantum network compatible with existing classical communication infrastructures that utilize low-loss optical fibers, we employ bidirectional QFC to and from the telecom O-band (Fig. 4.4 a)[114], see also Appendix B. After the photonic qubit at 737 nm is reflected off node A's SiV, a fiber-coupled, periodically poled lithium niobate (PPLN) waveguide pumped with 1623 nm light converts the photonic qubit's wavelength to 1350 nm. This frequency lies in the telecom O-band and shows low attenuation ($< 0.3\,\mathrm{dB\,km^{-1}}$) in conventional telecom single-mode fiber. After downconversion, the photonic qubit is sent through telecom fiber of varying length before a sec-

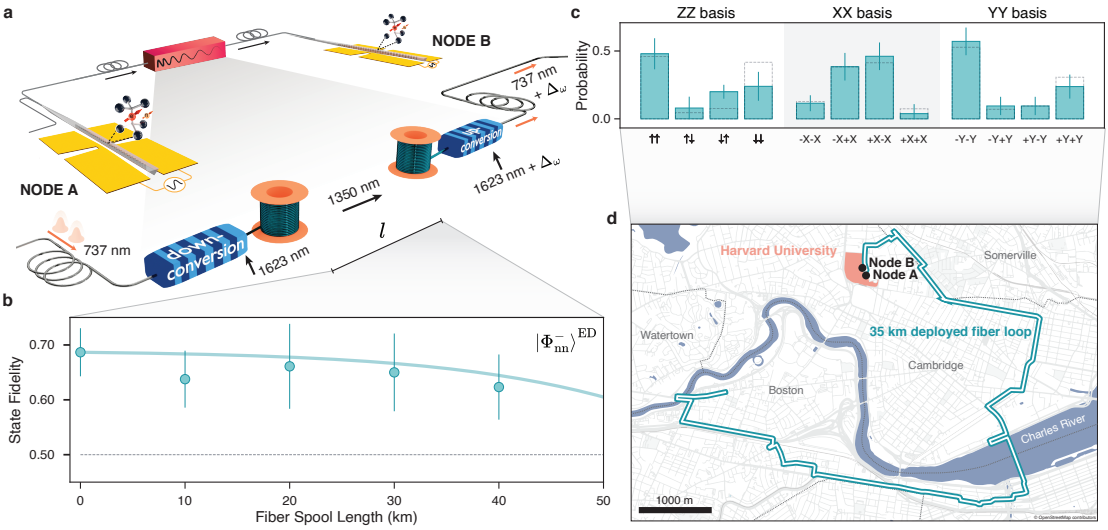


Figure 4.4: Nuclear spin entanglement distribution through 35 km of deployed fiber. **a.** Schematic of quantum frequency conversion setup. At node A, the photonic qubit is downconverted from 737 nm to 1350 nm, which can propagate with low loss in telecom single mode fibers. At the node B, it is upconverted back to 737 nm. The pump laser frequencies in the up- and downconversion setups are detuned by $\Delta_\omega = 13\,\mathrm{GHz}$ to compensate for the difference in optical frequencies of the two SiVs. **b.** Nuclear spin Bell state fidelities for varying lengths of telecom fiber spools between the two nodes. Entanglement persists for fiber lengths up to 40 km. Bell state decoherence can be explained by a model incorporating a decrease in signal-to-noise ratio due to dark counts at 2.7 Hz and conversion noise photons at 2.5 Hz (solid line). The dashed line shows the classical limit. **c.** Measurement results of Bell state measurement of $|\Phi^-_{\mathrm{nn}}\rangle^{\mathrm{ED}}$ state created through a 35 km long deployed fiber link shown in d., resulting in a fidelity of $\mathcal{F}^{\mathrm{ED}}_{|\Phi^-_{\mathrm{nn}}\rangle} = 0.69(7)$. Dashed bars show correlations predicted by a theoretical model using independently measured performance parameters of our system, see Appendix B.5.2. **d.** Route of the deployed fiber link connecting node A and node B. It consists of 35 km deployed telecom fiber routed towards and back from an off-site location, crossing four municipalities in the greater Boston metropolitan region. Error-bars in b. and c. are one s.d.

ond PPLN upconverts the photonic qubit back to 737 nm. This bi-directional frequency conversion allows for straightforward bridging of the frequency difference Δ_ω of the two SiVs: the pump laser's frequency of the upconversion setup is offset by Δ_ω from the downconversion pump laser's frequency. The total efficiency of the bidirectional QFC, including a final filter cavity, is 5.4 %, while the noise counts at node B's superconducting nanowire single-photon detector (SNSPD) are 2.5 Hz.

Using this frequency conversion scheme together with the entanglement method described above (Fig. 4.3 a), we remotely entangle two ^{29}Si nuclei through spools of low-loss telecom fiber up to

40 km in length (Fig. 4.4 b). For future repeater node applications of truly space-like separated quantum network nodes, it is important that entanglement persists until all nodes have received the classical heralding signal. To account for this effect, we execute an XY8-1 decoupling sequence for a total duration of 10 ms before performing the Bell state measurement. The decoupling duration is much larger than the classical signal traveling time $\Delta t(l) \approx 200\,\mu s$ for the maximal fiber length of $l = 40$ km. Thus, for the measured fiber distances, Bell state decoherence does not impact the measured Bell state fidelities. Instead, we find that the fiber-distance-dependence of the nuclear-nuclear entanglement fidelities is well described by SNSPD dark counts and telecom conversion noise photons, which reduce the signal-to-noise ratio at high fiber attenuation (solid line in Fig. 4.4 b).

In a practical setting, large-scale quantum networks can strongly benefit from existing fiber infrastructure to allow for long-distance entanglement distribution. Deployed fibers are subject to added noise, and excess loss, as well as phase- and polarization drifts [115,114]. We demonstrate that our system is compatible with conventional fiber infrastructure and is resilient to these error sources by generating nuclear entanglement through a 35 km loop of telecom fiber deployed in the Boston area urban environment (see Fig. 4.4 d). The overall measured loss in the loop (17 dB at 1350 nm) exceeds the nominal fiber attenuation of 11 dB at this wavelength, indicative of excess loss typical to deployed environments. Since the input polarization of the up-converting PPLN needs to align with the dipole moment of the crystal, polarization drifts introduced by the deployed fiber are actively compensated in order to prevent a loss in conversion efficiency, see Section 4.10. Using the deployed link, we generate entanglement with a fidelity of $\mathcal{F}^{\mathrm{ED}}_{|\Phi^-_{\mathrm{nn}}\rangle} = 0.69(7)$ (Fig. 4.4 c), demonstrating the quantum network performance in a realistic fiber environment.

4.5 Outlook

Our experiments demonstrate key ingredients for building large-scale deployed networks using the SiV-based integrated nanophotonic platform. They open the door for exploration of a variety of quantum networking applications, ranging from distributed blind quantum computing [117] and non-local sensing, interferometry and clock networks [22,118], to the generation of complex photonic cluster states [119]. Extension to entanglement distribution between true space-like separated nodes using deployed fiber requires only relatively minor experimental modifications and is not limited by the performance of the quantum nodes, see Appendix B.10. The success rate of the entanglement generation is currently limited by losses in the bi-directional QFC, which can be minimized by improving mode-matching into the PPLN and the efficiency of the filtering setup [120]. Furthermore, in-fiber attenuation could be further reduced to 0.2 dB km^{-1} by using two-stage QFC to 1550 nm [121]. The use of WCS also reduces the success rate and fidelity, which could be avoided by using SiV-based single photon sources [122] combined with active strain tuning of the nanophotonic cavities for wavelength matching [52,123]. Efficient coupling between the fiber network and the nanophotonic cavity could be improved by recently demonstrated cryogenic packaging techniques [124], while cooling requirements of the repeater nodes could be eased by deterministic straining of SiVs [125]. Entanglement fidelities could be improved by working with previously demonstrated nanophotonic cavities with higher cooperativity [64]. Implementing the above improvements, electron-electron entanglement fidelities of $\sim$ 0.95 with success rates of $\sim$ 100 Hz could be achieved, see Appendix B.7. Finally, the number of accessible qubits could be increased by addressing weakly coupled ^{13}C spins [126], allowing for more flexible multi-node network configurations. Combining these advances with the potential ability to create a large number of cavity-QED systems fabricated on a chip, this approach can eventually result in large-scale, deployable quantum networking systems.

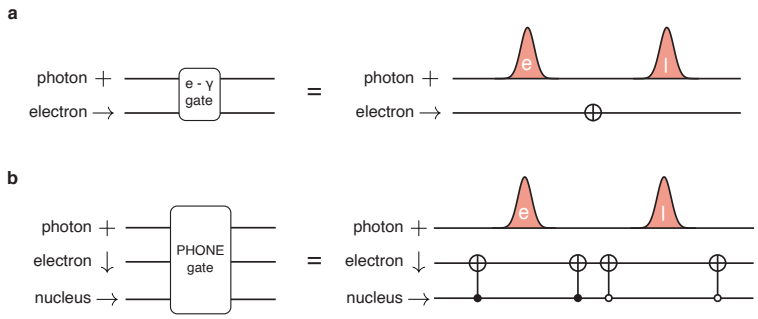


Figure 4.5: Spin-photon gate quantum circuits. **a.** Gate representation of the e-γ gate, entangling a time-bin photonic qubit with the SiV's electron spin. **b.** Gate representation of the PHONE gate, entangling a time-bin photonic qubit with the SiV's ^{29}Si nuclear spin.

The electron spin-dependent cavity reflectance is the building block of the photon-electron entangling gate (e - γ) gate, and the photon-nucleus entangling (PHONE) gate. The functionality of the two gates can be described in a single node configuration, where a TDI measurement is performed after the node. For the e - γ gate (see Fig. 4.5 a), the electron is initialized in the $|\text{SiV}\rangle = |\rightarrow_e\rangle = (|\downarrow_e\rangle + |\uparrow_e\rangle)/\sqrt{2}$ state, and a photonic time-bin qubit $|+\rangle = (|e\rangle + |l\rangle)/\sqrt{2}$ tuned to the frequency of the maximum reflectance contrast point between $|\downarrow_e\rangle$ and $|\uparrow_e\rangle$ is prepared and sent into the cavity-coupled SiV system. The early time-bin is only reflected off the cavity-QED system if the SiV's electron is in the high-reflectivity state $|\uparrow_e\rangle$, and the state proportional to $|e\downarrow_e\rangle$ is traced out:

$$|\text{Photon, SiV}\rangle = |l\rangle\,(|\downarrow_e\rangle + |\uparrow_e\rangle)/\sqrt{3} + |e\uparrow_e\rangle/\sqrt{3}. \tag{4.1}$$

A NOT$_e$ pulse is applied to the electron between the two time-bins, and the subsequent reflection of the late time bin results in a Bell state between the electron spin and the time-bin photonic qubit:

$$|\text{Photon, SiV}\rangle = (|e\downarrow_e\rangle + |l\uparrow_e\rangle)/\sqrt{2} \tag{4.2}$$

The spin-photon entanglement generation is heralded by the successful detection of a photon during the TDI measurement, such that single photons lost in transmission do not degrade the fidelity of the entangled state. The PHONE gate (Fig. 4.5 b) uses the electron spin to mediate entanglement between the nucleus and the photonic qubit. Before sending the time-bin qubit, the electron-nucleus register is initialized in the $|\downarrow_e \rightarrow_n\rangle$ state. A conditional electron spin flipping MW gate C_nNOT_e then prepares the following electron-nucleus entangled state: $|SiV\rangle = (|\downarrow_e\downarrow_n\rangle + |\uparrow_e\uparrow_n\rangle)/\sqrt{2}$. The remaining sequence is similar to the $e-\gamma$ gate, except with the addition of an unconditional NOT_e-pulse being applied to the electron between the two time-bins. A final conditional electron spin flipping MW gate $\overline{C_nNOT_e}$ disentangles the electron- and the nuclear spin and results in a Bell state between the nuclear spin and the time-bin photonic qubit:

$$|\text{Photon, SiV}\rangle = (|e\downarrow_n\rangle + |l\uparrow_n\rangle)\,|\downarrow_e\rangle\,/\sqrt{2}. \tag{4.3}$$

4.7 Experimental setup

The optical path of the experiment consists of multiple stages shown in Fig. 4.6 and Fig. 4.8. A laser table (Fig. 4.6 a) prepares all the required optical fields for control and feedback, as well as for the photonic qubits. The photonic qubit is sent to node A (Fig. 4.6 b) where it interacts with the SiV-cavity system. The photonic qubit then continues to the frequency shifting stage (Fig. 4.8 a) or telecom frequency conversion stage (Fig. 4.8 b) depending on the specific experiment, after which it travels to node B (Fig. 4.6 c) to interact with the second SiV-cavity system. Finally, the photonic qubit is measured in the $|+\rangle$ / $|-\rangle$ basis with the TDI (Fig. 4.6 d). Each SiV at nodes A and B is located in a separate dilution refrigerator (BlueFors BF-LD250) with a base temperature below 200 mK. The SiV–cavity system is optically accessed through a tapered fiber. Lasers at 532 nm are used to stabilize the charge state of the SiVs at each node. The SNSPDs (Photon Spot) are used for

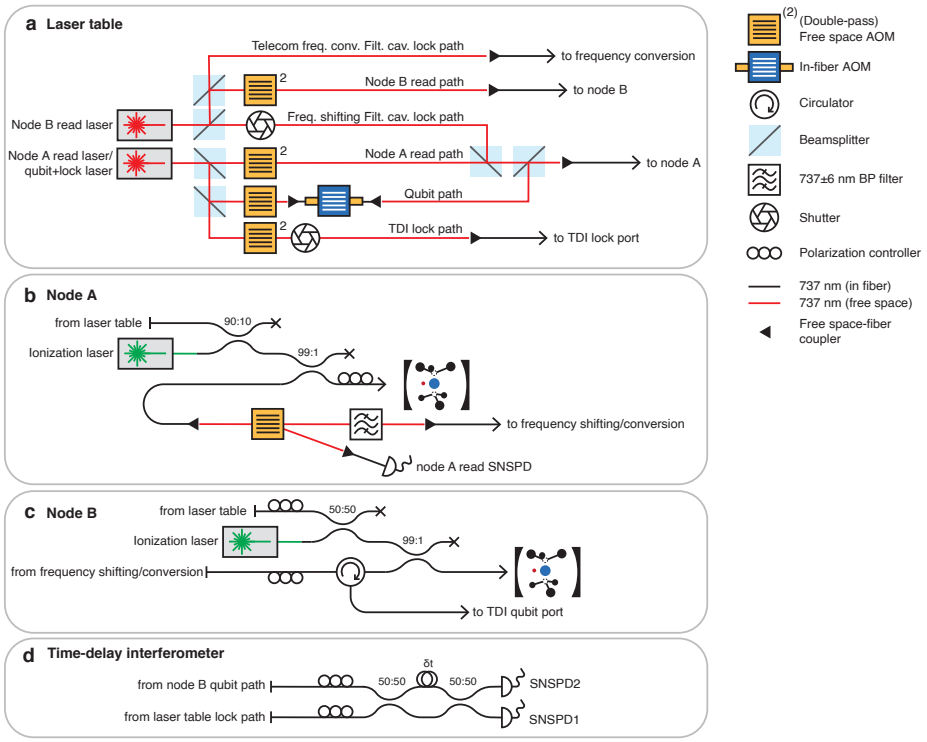


Figure 4.6: Schematic drawing of the two-node quantum network. **a.** Laser table. Here, all the optical fields are prepared for node A and B readout, filter cavity, and time-delay interferometer (TDI) locking, and the photonic qubits are shaped by an in-fiber AOM. **b. and c.** Node A and B. The nodes contain the photonic qubit travel path and a readout path for individual spin readout, as well as an insertion port for a green laser stabilizing the SiVs' charge state. **d.** Time-delay interferometer. The TDI allows measurement of the photonic qubits in superposition bases.

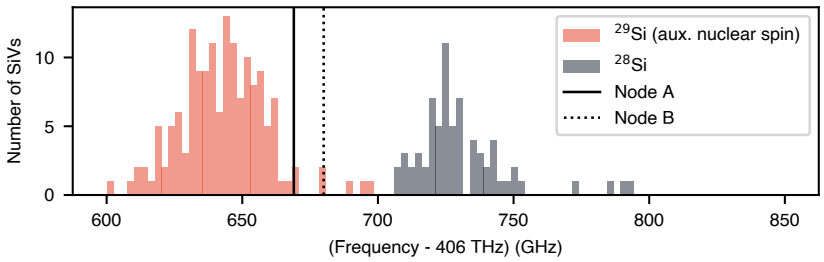


Figure 4.7: Optical resonance frequencies of 223 characterized cavity-coupled SiVs. The results of this work were produced with SiVs with the ^{29}Si isotope of silicon, which have a deterministic auxiliary nuclear spin memory. The optical resonance frequencies of the specific SiVs used in this work are given by the solid (node A) and dashed (node B) vertical lines.

SiV state readout, filter cavity locking, and TDI locking. Counts from the SNSPDs are recorded on a time-tagger (Swabian Instruments Time Tagger Ultra). A Zurich Instrument HDAWG8 2.4 GSa/s AWG is used for sequence logic, control of the acousto-optic modulators (AOMs) and phase electro-optic modulators (EOMs), as well as microwave (MW) control. The MW and RF chain is identical for node A and B and is described in 53.

4.8 Frequency shifting

SiVs, like all solid-state qubits, display an inhomogenous distribution in their transition frequencies due to sensitivity to their local environment. In the case of the devices used in this work, we typically see a variation of roughly ± 50 GHz for a SiV formed with a given Si isotope (Fig. 4.7). In particular, the two SiVs used in this work have a difference in their optical transition frequency $\Delta_\omega = \omega_B - \omega_A = 13$ GHz, where $\omega_{A/B}$ is the frequency of the SiV in Node A/B respectively.

In order to bridge this frequency difference and generate entanglement between the SiVs, electro-optic frequency shifting is used (Fig. 4.8 a). Briefly, the initial time-bin photon is generated at a frequency of ω_A. After interacting with the SiV in node A, it is sent through a phase EOM which is driven by a signal generator at a microwave frequency of Δ_ω. As the bandwidth of the optical

photon is much narrower than Δ_ω of the modulator, the frequency spectrum of the output photon can be approximated as a series of optical harmonic frequencies with intensity given by:

$$I(\omega_A + k\Delta_\omega) \propto J_k^2(V_0/V_\pi) \tag{4.4}$$

where k is an integer of the frequency harmonic used, J_k is the k-th Bessel function of the first kind, V_π is the half-wave voltage and V_0 is the voltage applied to the modulator. As we are interested in shifting the output photon to a frequency ω_B, which corresponds to the $k = 1$ harmonic of the output frequency spectrum, the power of the microwave drive of the EOM is set such that this harmonic is maximized. To filter out unwanted harmonics, the phase EOM's output is sent through a free space Fabry-Pérot cavity (linewidth = 160 MHz, finesse = 312) locked at frequency ω_B. The overall efficiency is approximately $\sim 7.4\%$, given by the product of the maximum EOM sideband power occupancy (34%), the insertion loss of the EOM ($\sim 50\%$), and the insertion loss of the filter cavity including transmission through the cavity and free-space to fiber losses ($\sim 40\%$). We note that this method can be used to shift photons across much larger frequency differences without any additional degradation of efficiency, only limited by the bandwidth of practically available microwave sources and EOMs, and even beyond that using higher harmonics of the output frequency spectrum at the expense of efficiency.

4.9 Telecom frequency conversion

To operate over long distances, it is beneficial to transmit photons over lower-loss telecom frequencies. Since SiVs have a natural optical transition at 737 nm, which has an in-fiber loss of $>$ 4 dB km^{-1}, we use quantum frequency conversion to convert it to 1350 nm, which is in the telecom O-band and has a loss of < 0.3 dB km^{-1} in SMF28 fiber.

The conversion was performed using fiber-coupled RPE (reverse photon exchange) LN (Lithium

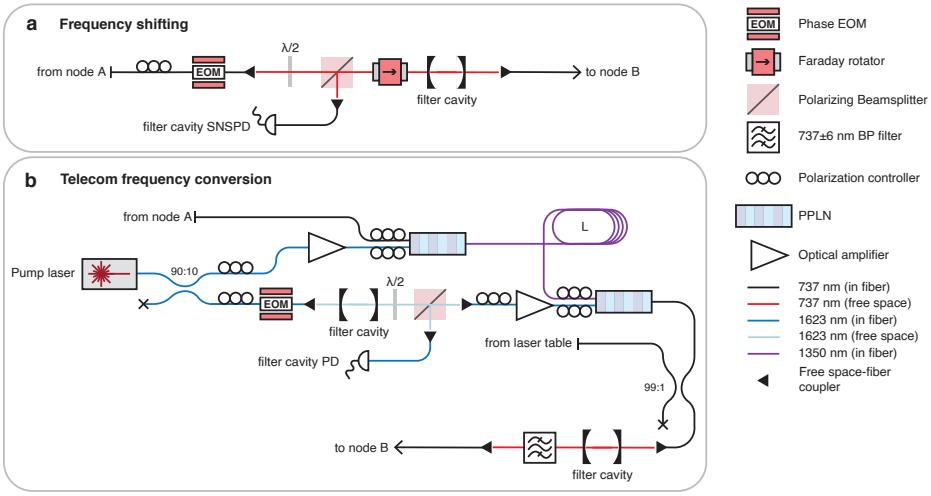


Figure 4.8: Frequency shifting/conversion setup. **a.** Frequency shifting. This setup is used to directly bridge the frequency difference between the two nodes while staying in the visible light range. **b.** Telecom frequency conversion. This setup is used for long-distance entanglement generation. It contains two frequency conversion stages: one from visible to telecom, and one from telecom to visible. The two stages are separated by a variable amount of fiber spools of total length L, or a field-deployed $35\,\mathrm{km}$ fiber.

Niobate) waveguide devices (AdvR) with a pump at 1623 nm. For down-conversion 737 nm + 1623 nm $\rightarrow$ 1350 nm, a Difference Frequency Generation (DFG) device was used with a pump power of 23 dBm at saturation, resulting in overall 33% conversion efficiency. The up-conversion 1350 nm+1623 nm $\rightarrow$ 737 nm used a Sum Frequency Generation (SFG) device with a pump power of 25 dBm at saturation, resulting in overall 30% conversion efficiency. The conversion efficiency in both directions is limited by impedance mismatch between the fiber and waveguide modes. The same pump laser is used for DFG and SFG processes with a frequency offset created by an EOM to compensate for frequency differences $\Delta_\omega = 13$ GHz of the SiVs in two nodes. A home-built Fabry-Pérot cavity (linewidth = 160 MHz, finesse = 312) is used to filter excess noise from the pump at the output of the SFG device. For more details about the telecom setup, see Fig. 4.8 b.

4.10 Polarization stabilization

In-field deployed fibers experience polarization drifts, which need to be compensated due to the polarization sensitivity of the up-converting PPLN used after the deployed fiber link. Fig. 4.9 a shows the setup used to characterize and stabilize the change in the degree of polarization (DOP) introduced by the deployed fiber. At the input of the fiber link, a classical signal from a linearly polarized laser at 1350 nm is sent through the deployed link. At the output of the link, a polarimeter measures the DOP as expressed by the two degrees of freedom ellipticity $\chi \in (-\pi/4, \pi/4)$ and azimuth $\psi \in (-\pi/2, \pi/2)$. Optical switches are used to connect the deployed fiber link to either the full experiment or the polarization stabilization setup. Fig. 4.9 b shows the histogram of measurements of χ and ψ over a period of 5 days, without polarization stabilization, showing that the DOP traces out the full phase space over this period. To stabilize the polarization at the output of the fiber link to a well-defined DOP (arbitrarily chosen to be $\chi = \psi = 0$), a fiber-squeezer-based polarization controller is used. During the polarization stabilization sequence, the value of the following cost

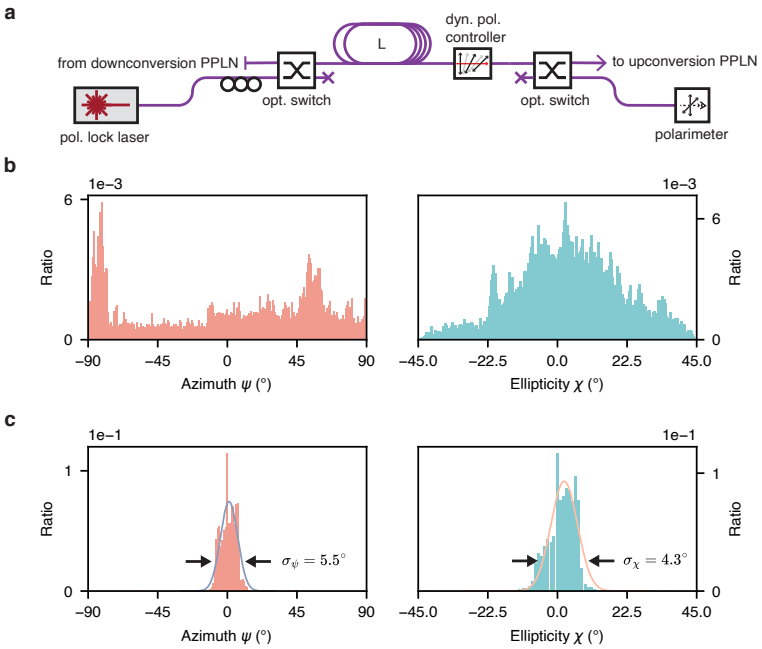


Figure 4.9: Polarization stabilization. **a.** Experimental setup used to measure and stabilize the change of the DOP introduced by the $35\,\mathrm{km}$ fiber link. A linearly polarized lock laser can be launched into the fiber link. After the fiber link, the DOP is measured using a polarimeter. A fiber-based polarization controller is used to stabilize the DOP. **b.** DOP measurement during 5 hours through the $35\,\mathrm{km}$ fiber link, not using polarization stabilization. During the measurement period, the initially linearly polarized light traces out the full phase space of the DOP. **c.** DOP during 5 days of nuclear-nuclear entanglement generation, with polarization stabilization enabled. The DOP can be stabilized around $\chi = \psi = 0$.

	Electron-Electron Entanglement	Nucleus-Nucleus Entanglement (ED)
Repetition Rate R	10 kHz	1.4 kHz
Success Probability η	7.7×10^{-6} - 2.5×10^{-4}	2.0×10^{-5}
Duty Cycle D	34 %	20 %
Success Rate r_{suc}	16 mHz - 1050 mHz	6 mHz

Table 4.1: Success rates. Average values for repetition rate, success probability, and duty-cycle for electron-electron entanglement generation, shown in Fig. 4.2, and nucleus-nucleus entanglement generation, shown in Fig. 4.3. For the nucleus-nucleus entanglement generation, values have been averaged across all decoupling times and $|\Phi_{\text{nn}}^{-}\rangle^{\text{ED}}$ and $|\Phi_{\text{nn}}^{+}\rangle^{\text{ED}}$. For the electron-electron entanglement generation, the success probabilities vary due to varying mean photon numbers in the photonic qubit.

function is evaluated:

$$C(\chi, \psi) = \sqrt{(\cos(\chi) - 1)^2 + (\cos(\psi) - 1)^2} \tag{4.5}$$

By employing a gradient-descent algorithm, the optimal control voltages of the polarization controller are determined. The results of this polarization stabilization are shown in Fig. 4.9 c, which shows a histogram of the DOP measured during 5 days of nuclear-nuclear entanglement generation via the deployed fiber. The polarization stabilization routine is interleaved with the entanglement generation experiment and runs during 3 % of the experimental time, minimally impacting the overall duty cycle. The insertion loss of the polarization stabilization setup is approximately 1.5 dB.

4.11 Success rate

The success rate r_{suc} of heralded entanglement at the TDI can be described as: $r_{\text{suc}} = \eta R D$, where η is the success probability of a heralding event, R is the repetition rate of the experiment and D is the duty cycle of the experiment. The success probability is limited by the photonic link efficiency and protocol-specific loss channels, such as the mean photon number $\mu < 1$ of the photonic qubit's

WCS (see Appendix B for more information). The repetition rate R is limited by the readout time for the two nodes' electron spin, which is 67 μs and 17 μs for node A and node B, respectively. The duty cycle D is reduced from its ideal value of 1 by periodic locking of the TDI and the filter cavity after the frequency shifting or telecom conversion setup, active tracking of the SiV's optical frequency, and, in case of the entanglement generation experiment through the deployed fiber link, polarization stabilization. Furthermore, the application of the green ionization laser to reset the SiV's charge state additionally reduces D. By discarding measurements where the spin-dependent reflectance contrast falls below a certain threshold, indicative of large spectral diffusion, D is further reduced. On average, this contrast threshold for the SiV in node A was set to 1:16, while for the SiV in node B it was set to 1:8. These thresholds resulted in an average rejection of 23% of datapoints per dataset. Table 4.1 shows average values for R, η, D, and r_{suc} for electron-electron entanglement generation, and nuclear-nuclear entanglement generation.

5

Conclusion

This thesis presents two major applications of quantum memory networks: the high-efficiency preparation of bandwidth-tailored single photons and the distribution of entanglement over 35 km of deployed fiber. These results highlight the potential of SiV centers coupled to nanophotonic cavities as a promising platform for large-scale, deployed quantum networks. The final chapter will conclude by exploring strategies to enhance the platform's performance and scale the system.

5.1 Using single photons for entanglement distribution

Using single photons as qubits in entanglement distribution experiments holds the potential to overcome the fidelity-rate tradeoff caused by the Poissonian photon statistics of weak coherent states. In order to implement the single photon source demonstrated in Chapter 3 for entanglement distribution experiments, two main challenges must be addressed.

First, the experimental footprint of a SiV-based single photon source must be considered. Currently, the source operates in a separate dilution refrigerator. By employing cryogenic fiber-packaging methods [124] and positioning the chip within the stray field of the vector magnet, it may be possible to integrate the single photon generation chip into the same dilution refrigerator setup used as a quantum network node, making it more space- and cost-efficient. Alternatively, deterministic straining of the SiV centers via thin films [125] could increase the SiV's ground-state splitting, enabling coherent single photon generation above liquid helium temperatures, and significantly reducing the cooling requirements.

Another limiting factor is the need for frequency shifting. The frequency of the emitted photons must match the optical frequency of the SiV centers used for entanglement generation. The loss introduced by conventional electro-optic frequency shifting methods would reduce overall single photon generation efficiency to the point where weak coherent states again become preferable. A potential solution is to use active strain-tuning techniques [123] to bring the emitted photons into resonance with the communication qubits used in the quantum memory network.

5.2 Nanofabrication and materials development

A major driver of future improvements to the SiV-based quantum network platform lies in the progress of materials engineering and nanofabrication techniques. The currently utilized nanofabrication stack relies on creating free-standing nanophotonic cavities from bulk diamonds using angled

reactive ion-beam etching[127]. This method limits device geometries, making features like closely placed waveguides challenging to achieve. Furthermore, this process's high sensitivity to fabrication parameters, such as the thickness of electron-beam resists, reduced the yield. Moving away from angled-etching and transitioning to a platform that requires only top-down patterning of nanostructures could improve yield and enable more complex device architectures. This would open doors for the multiplexing of multiple nanophotonic cavities coupled to one waveguide, which could increase entanglement generation rates. Two fabrication methods show promise in realizing a top-down-only patterning approach. First, recently optimized thin films of high-purity diamond offer a path to high-Q nanocavities with integrated color centers[128,129]. Second, quasi-isotropic undercutting can produce thin diamond slabs, which can then be patterned using top-down etching techniques[130]. Besides optimizing the diamond platform, heterogeneous integration of diamond with high-performance optical platforms such as thin-film lithium niobate (TFLN) could be pursued[111]. This could enable offloading active switching to an integrated TFLN chip, which could be done at low loss and would be particularly useful for device multiplexing.

5.3 Optimizing entanglement distribution

Future quantum network applications require high-fidelity entanglement, fast entanglement generation rates, and versatile memory qubits. The long coherence time of the ^{29}Si nucleus makes it an effective memory qubit for extending fiber distances between quantum network nodes. However, more advanced distributed quantum protocols, such as the quantum repeater protocol[18] and entanglement purification[131], require that the memory qubit stores quantum information while the communication qubit is reset multiple times. Due to differential hyperfine electron-nucleus interaction in the ground and excited state, the ^{29}Si nucleus experiences decoherence during electron-spin state readout[53]. This could be circumvented by using ^{13}C spins[51], which, combined with advanced

control sequences [126,132], could be used as a memory qubit robust to electron-readout-induced decoherence.

Further improvements to entanglement fidelities could focus on mitigating optical contrast errors and microwave gate errors. Optical contrast errors could be reduced by systematically eliminating stray reflections in the fiber network or through interferometric cancellation of these reflections. Reducing microwave gate errors could be achieved by improving the spectral stability of SiV centers, which would minimize the need for active qubit frequency tracking and mitigate errors caused by off-resonant driving of the SiV center's electron spin due to qubit frequency diffusion. Enhancing the stability of SiV centers could potentially be achieved by optimizing the implantation dose and performing annealing at higher temperatures [133,134].

There are several strategies to enhance entanglement generation rates. Multiplexing, as described earlier, could significantly increase entanglement generation rates. Additionally, optical losses at the tapered fiber interface might be reduced by employing advanced cryogenic packaging methods [124]. Shifting to a phase-based spin-photon gate scheme could circumvent the intrinsic 50 % loss of amplitude-based gates. Moreover, transitioning from serial to parallel entanglement schemes could increase generation rates, at the expense of required phase-locking. Lastly, moving from time-bin qubits to qudits, along with developing efficient qudit interferometers, could enable the simultaneous generation of both nuclear-nuclear and electron-electron entanglement.

The efficient generation of tailored photonic qubits and successful demonstration of entanglement distribution in a two-node quantum network helped lay the groundwork for system-level quantum network experiments with SiV centers coupled to nanophotonic cavities. Implementing even a subset of the abovementioned advancements could unlock a wide range of practical quantum network applications, including long-distance quantum communication, distributed (blind) quantum computing, and quantum-enhanced non-local sensing, positioning SiV-based quantum networks as a promising platform for the years to come.

A

Supporting Material for Chapter 2

A.1 Nanophotonic cavity

In order to be widely useful, the high-purity single photons must be generated and outcoupled efficiently, ideally into a single-mode fiber. This is especially true when generating large multi-photon states for which generation probability scales exponentially with single-photon efficiency. Single photon generation and outcoupling efficiency for an atom-cavity system η is determined by both the

atom-cavity cooperativity C as in $p_c = \frac{C}{C+1}$ and the overcoupling of the cavity to the waveguide as in $p_w = \frac{\kappa_w}{\kappa_w+\kappa_s}$, as well as additional system losses from imperfect optical elements:

$$\eta = p_c * p_w * p_o \tag{A.1}$$

Where p_c is the probability of emission into the cavity, and p_w is the probability that a photon in the cavity couples into the probe waveguide. Systemic optical losses (p_o), although crucial in practical systems and often dependent on the physical platform, are not fundamental to the cavity quantum electrodynamics (CQED) system design, so we do not include them in our optimization of source efficiency η_s. Instead, we focus on the first two terms, $\eta_s = p_c * p_w$.

When the emitter is close to resonance with the cavity, the probability of emission of a single photon into the cavity is given by the cooperativity as $p_c = \frac{C}{C+1}$ [55] with $C = \frac{4g^2}{\kappa\gamma}$ where g is the atom-cavity coupling rate, κ is the full width at half max (FWHM) cavity energy decay rate, and γ is the quantum emitter's spontaneous decay rate (FWHM). Meanwhile, the probability that a photon in the cavity will decay into the waveguide is given by $p_w = \frac{\kappa_w}{\kappa_w+\kappa_s}$, where κ_s represents all unwanted cavity loss, such as scattering into free-space or coupling into the unprobed waveguide. In terms of CQED parameters, the source efficiency is

$$\eta_s = \frac{4g^2\kappa_w}{(\kappa_s+\kappa_w)(4g^2+(\kappa_s+\kappa_w)\gamma)} \tag{A.2}$$

Maximizing this function optimizes the photon generation efficiency. Thus, the optimal decay rate into the waveguide is given by

$$\kappa_w^{(opt)} = \sqrt{\frac{\kappa_s(4g^2+\kappa_s\gamma)}{\gamma}} \tag{A.3}$$

Notably, device performance, in this case single-photon generation efficiency, is not maximized by simply maximizing device cooperativity, as is often the case in other CQED protocols [135,136,137].

In fact, as illustrated by equation A.3 and fig. 2a in the main text, optimal overall photon generation efficiency is achieved by trading off some cooperativity for a better balance between relative cavity coupling rates κ_w and κ_s. This underscores the importance of creating a cavity with well-controlled coupling rates.

The nanophotonic cavities used in this experiment are similar to those used in the previous CQED experiments with silicon-vacancy centers in diamond (SiV)[64,51,96,137]. However, while previous generations of cavities were designed to maximize cooperativity (or equivalently Purcell enhancement), these nanophotonic cavities were designed to balance maximizing cooperativity with ensuring directional waveguide coupling. This additional constraint forced us to expand the design parameter space. The resulting design is asymmetric throughout the cavity, which is different from traditional photonic crystal cavity design. We discuss the subtle but fundamental difference below after some brief background on photonic crystal cavities.

The original concept of a photonic crystal cavity was realized as a defect within an otherwise perfect Bragg mirror. For example, so-called L3 cavities in air hole-based photonic crystals create a defect by replacing three adjacent air holes with completely filled dielectric (fig. A.1a)[99]. The defect region supports optical modes that are forbidden elsewhere in the photonic crystal by a photonic band gap, thus a symmetric cavity is formed. In 1-D nanophotonic cavities (fig. A.1b), index guiding confines the light in y and z while the one-dimensional photonic crystal acts as a cavity along x, but the fundamental principle is identical to the L3 case. Most modern nanophotonic cavity designs exchange the abrupt introduction of a defect in favor of smoothly deforming the mirror region to create an extended defect that allows for gentle confinement and reduces scattering losses (fig. A.1c)[138]. Additionally, to further reduce scattering in 1-D nanophotonic cavities, a region that transitions from the cavity mirrors to the coupling waveguide is typically appended to the cavity. The smooth defect and waveguide transitions are the essential elements of the modern nanophotonic cavity that offers a high Quality factor and wavelength scale mode volume $V \sim (\frac{\lambda}{n})^3$ in many

material platforms. If an undercoupled or overcoupled cavity is desired, "mirror" unit cells are added or removed on each side of the defect, allowing for directional coupling. Importantly, while this modern design differentiates the device into characteristic regions (mirror region, waveguide transition region, defect region) (fig. A.1d), it still relies on the original concept of a defect in an otherwise perfect Bragg mirror to create a cavity.

The nanophotonic cavities used in this experiment go beyond this "three-region" design by allowing the mirror regions and their corresponding transition regions to be different on the left and right sides of the defect region. Figure A.2c depicts a top-down view of this cavity. Since the mirror regions do not have identical unit cells, the defect region serves both as a localizing defect and a transition between the different mirror regions. Furthermore, the cavity is no longer simply a defect in an otherwise perfect Bragg mirror. Instead, each side of the cavity is a different Bragg mirror. This is similar to a Fabry-Perot cavity with different mirror strengths on either side, but the cavity mode is still determined by the supported modes of the defect regions is in traditional photonic crystal cavities.

While our asymmetric cavity design does not correspond to the traditional picture of a defect in an otherwise perfect Bragg mirror, the additional design freedom proves useful for designing high cooperativity overcoupled nanophotonic cavities. Specifically, as we explain in the next section, we are able to create a mirror region that is effectively weaker for the cavity mode due to its relative detuning. Moreover, the quasipotential description we use to understand this unorthodox design reveals new insights into the limitations of the traditional approach.

A.1.1 Quasipotential

This asymmetric cavity is best understood by analogy to a quantum particle in a finite potential well. The idea is based on the similarity between a massive particle tunneling through a potential barrier and the evanescent decay of a photon in a photonic band gap[99]. For our cavity design, the trans-

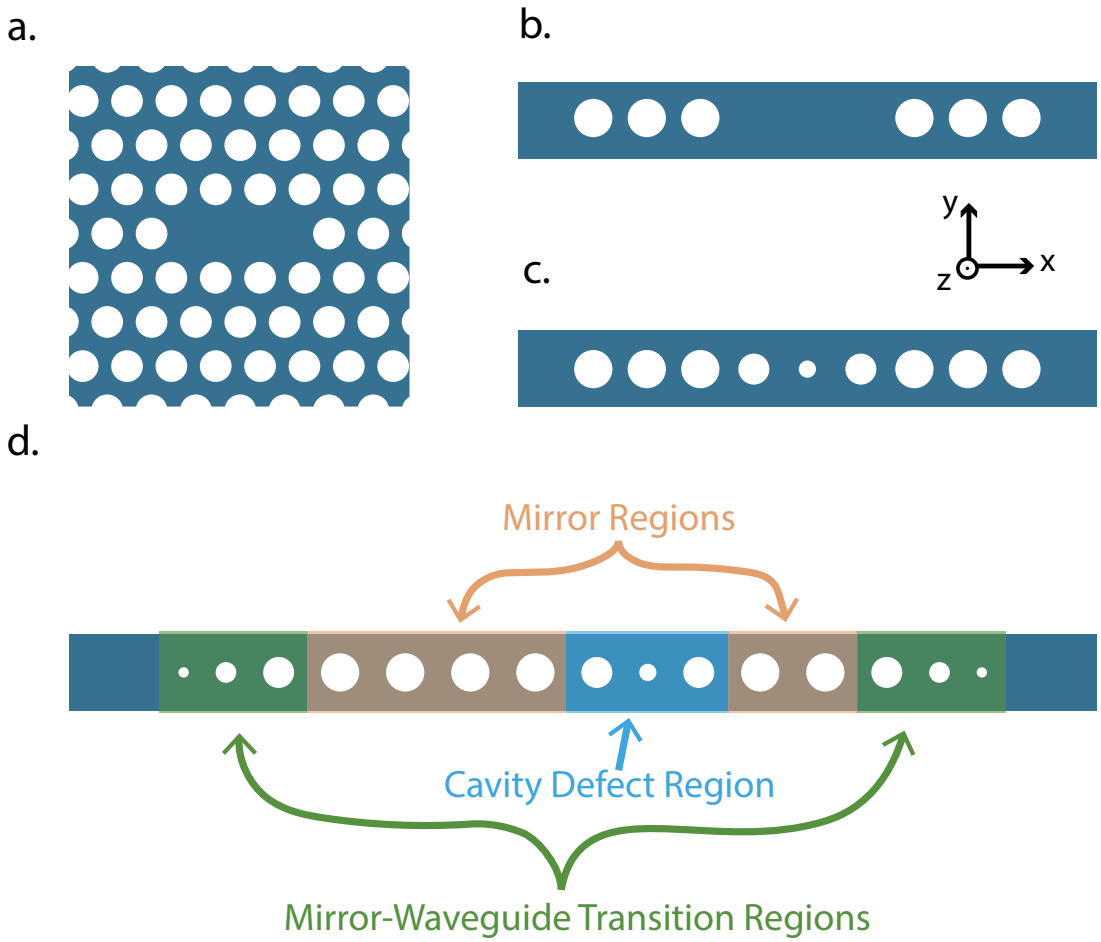


Figure A.1: Photonic Cavity. (a) An L3 cavity in a 2-Dimensional photonic crystal exemplifies the original concept of a cavity formed by a defect in an otherwise perfect photonic crystal. (b) The same concept is used in 1-Dimensional photonic crystal cavities in nanobeams. Transverse confinement is provided by index guiding, and the cavity is formed by a defect in the photonic crystal. (c) Smoothly transitioning from the perfect crystal to the defect reduces scattering, increasing the quality factor of the cavity. (d) Modern nanophotonic cavities can be understood as being composed of three functionally distinct regions.

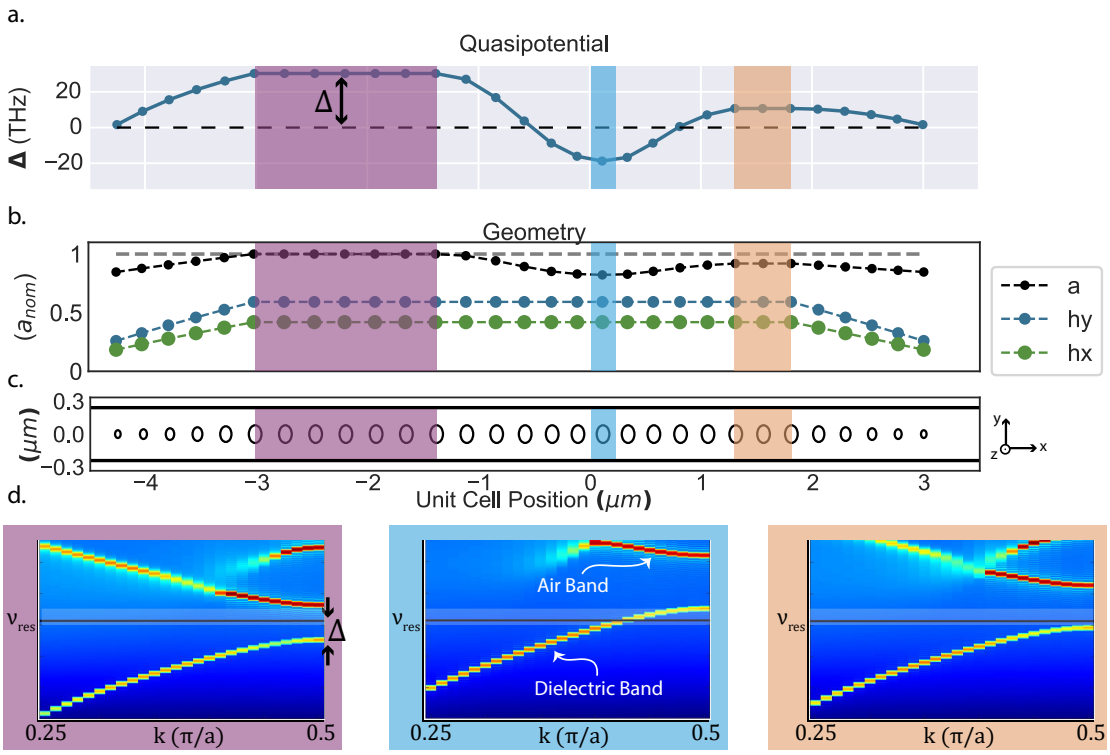


Figure A.2: (a) Quasipotential for this device (b) Relative hole geometry parameters in units of the nominal lattice constant, a_{nom}. hy_{nom} = 161 nm, hx_{nom} = 114 nm, a_{left} = 272 nm, a_{right} = 250 nm. hy_{nom} and hx_{nom} correspond the cavity and mirror region holes' major and minor axes respectively. a_{left} and a_{right} are the lattice constants of the mirror regions on the left and right side of the cavity respectively. (c) Scale depiction of cavity top view. Waveguide width = 482 nm, triangle apex half-angle = 50°, maximum defect = 0.1392. (d) Simulated photonic bandstructure diagrams for representative unit cells from each cavity section. The color code indicates where the corresponding unit cell is located in the cavity. Quasipotential barrier height is defined as the detuning, Δ, of the cavity resonance frequency (horizontal black lines) from the dielectric band edge at $k = 0.5$. Note the low potential barrier on the right side (orange) is due to the proximity of the dielectric band to the optical mode and *not* a smaller band gap between the dielectric and air bands. Light white shaded regions represent the frequencies which would evanescently decay in both mirror regions.

missivity of a mirror region is analogous to the tunneling probability through a potential barrier. The barrier height is given by the detuning of the mode from the dielectric band edge of each unit cell, and the barrier width is given by the number of unit cells in the mirror region. In this picture, important design targets like overcoupling and mode volume are made intuitive by the shape of the quasipotential. For example, the asymmetric quasipotential of the cavity used in these experiments is shown in fig. A.2a, and it illustrates that the optimal cavity has both a lower and narrower barrier on the side which preferentially couples to the waveguide while maintaining a deep potential well necessary for the tight mode confinement characteristic of nanophotonic cavities. The simulated electric field overlay in fig. 2b of the main text illustrates this wavelength scale confinement (mode volume = $0.67\left(\frac{\lambda}{n}\right)^3$).

On one side, we create an unusually weak mirror region to achieve good waveguide damping, while the other side has a strong mirror region with a high barrier to maintain low mode volume and effectively eliminate coupling to the unprobed waveguide. Using different unit cells in each mirror region is a departure from the traditional idea of a defect region contained within a uniform Bragg mirror[99], but it enables the cavity parameters to approach the best possible efficiency as defined by eqn. A.3 and maintain the same small mode volumes seen in previous device designs.

We design the cavity to support a dielectric mode. (The electric field is concentrated in the diamond, not in the air). Therefore, we define the quasipotential barrier as the detuning of the dielectric band (lower band) from the resonance frequency of the cavity. Then, using Lumerical FDTD, we simulate the photonic band structure for each unit cell. We plot the detuning at each unit cell to reveal the quasipotential landscape of the nanophotonic cavity (fig. A.2).

In fig. A.2, we see the band structures corresponding to representative unit cells from the left mirror region, the defect region, and the right mirror region. Traversing the cavity from right to left, we see that the dielectric band starts very close to the optical mode. This small detuning corresponds to the low potential barrier visible in the orange section of fig. A.2a, and it enables the tunneling

that gives rise to the high coupling rate into the waveguide on this side of the cavity. Moving left to the blue indicated unit cell, the lattice constant decreases (fig. A.2b), which shifts the bands to a higher frequency. This causes the dielectric band to overlap the resonant frequency of the cavity. Thus, the unit cells in the defect region support a propagating mode. Finally, we get to the purple, left mirror region. Here, the lattice constant has increased, shifting the bands down which results in the resonance frequency being far from the dielectric band near the center of the band gap. Thus, only evanescent modes are supported in this region, and they decay quickly. Similar to a particle in a finite well, the decay constant is proportional to the square root of the detuning.

Importantly, the detuning which weakens the mirror on the right side is only possible because the mirror region on the left side is significantly red detuned relative to the right mirror region, as illustrated by fig. A.2d. Traditionally, a cavity's resonant frequency is near the center of the band gap of the mirror regions, as this is where the mirrors are strongest. In that case, the band structure for both mirror regions would be similar to the purple highlighted band structure in fig. A.2d. On the other hand, in this cavity, modes that would have frequencies near the center of the band gap for the mirror region on the right side approach the air band for the mirrors on the left side. This is illustrated by the white shading in the three panels of fig. A.2d. The upper edge of this shading is defined by the lowest air band in the mirror regions, that of the left side mirror cells, and the lower edge of this shading is defined by the highest dielectric band in the mirror regions, that of the right side mirror cells. Thus, any mode that could be formed by this combination of mirror cells would have to have a frequency in the white shading. In other words, the only modes which are allowed by the band structure of the left side force the mirrors of the right side to be weaker. This fine-tuning of the barrier height by tuning the frequency of the bands relative to the resonant mode is a novel and useful feature of this asymmetric design approach.

While the quasipotential is a useful tool for understanding an optimized design, it's important to note that it is a simplification of the nanophotonic cavity that neglects important degrees of free-

dom, namely, it does not capture information about the transverse mode profile. Therefore, a cavity should not be designed solely by concatenating unit cells to create a desired quasipotential. Care should also be taken to ensure that the transverse mode profile of each subsequent unit cell does not differ significantly from its neighbors as this would induce significant scattering, reducing the cavity quality factor. In our cavity design, we ensure this smooth changing mode profile by smoothly changing the unit cell parameters.

A.1.2 Mode Volume Trade-off

In a highly overcoupled cavity, the coupling rate to one side is much higher than the coupling rate to the other side and to free space. In traditional nanophotonic cavities, this coupling rate difference is achieved simply by putting a different number of mirror unit cells on each side of the defect region. This approach was used successfully in [139]. However, there is a minimum number of mirror unit cells below which the cavity suffers increased scattering losses. (In our system, the minimum number is typically three unit cells.) Therefore, if the directional coupling rate is too low at the minimum barrier width, the barrier height of the mirror unit cells needs to be lowered. Lowering the barriers increases the mode volume of the cavity, as illustrated in fig. A.3e.

Atom-Cavity cooperativity depends on both the cavity quality factor Q and the mode volume V as given by the Purcell enhancement $\frac{Q}{V}$. Thus, in order to maximize cooperativity, one must maximize the cavity quality factor and minimize the mode volume. Conversely, for a given quality factor, a cavity with a larger mode volume will have lower cooperativity, and, in this case, a lower single-photon generation efficiency.

In a cavity with the same height barrier on each side of the defect region, there is an intrinsic trade-off between overcoupling and mode volume. This trade-off is intuitively obvious from the fact that the field decay is stronger in a high barrier (fig. A.3c) than in a low barrier (fig. A.3d). Thus, when using lower barriers to allow for better waveguide coupling, mode confinement is worse, caus-

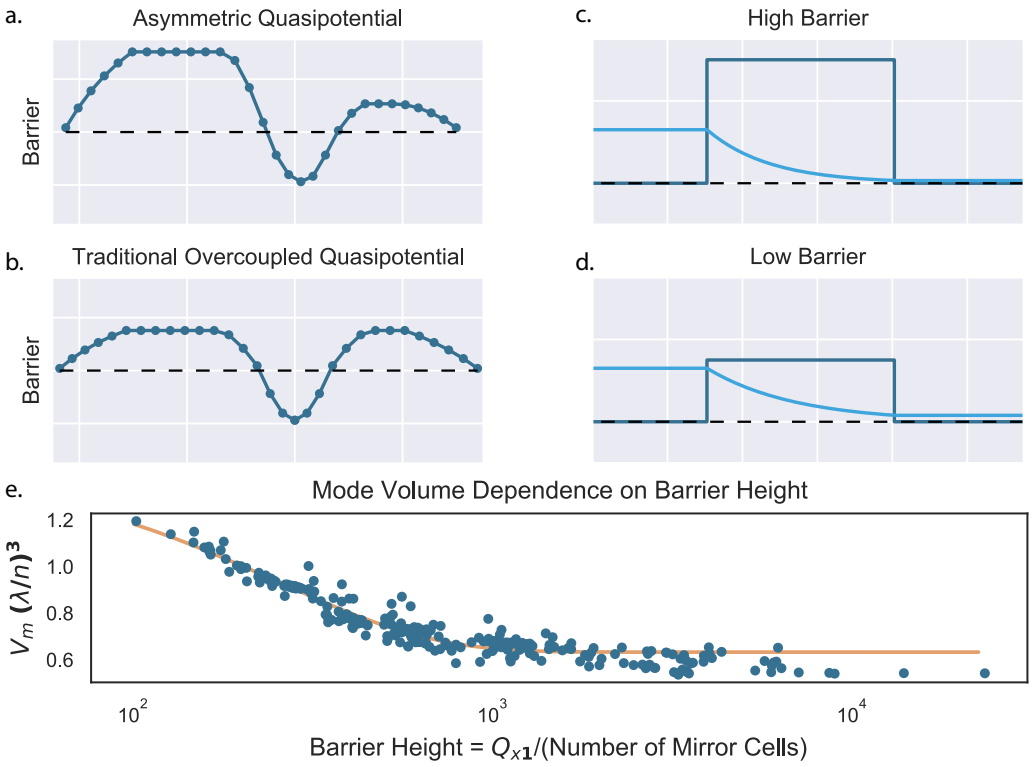


Figure A.3: Mode volume increases for lower potential barriers due to slower decay within the mirror region. (a) The asymmetric quasipotential of the cavities used in this experiment takes advantage of both the tight confinement of a high barrier on the left-hand side for low mode volume and the fast coupling of a low barrier on the right-hand side for good overcoupling. (b) In order to make an overcoupled cavity with identical unit cells in each mirror region, the barrier must be low, to allow for good waveguide coupling, but long on one side to enable asymmetric coupling. This restrictive design creates a trade-off between overcoupling and mode volume because a high barrier (c) strongly suppresses the evanescent field, while a low barrier (d) suppresses the field more weakly. (e) Simulation data of many cavities accumulated during a geometry optimization sweep illustrate that low barrier heights correspond to larger mode volumes.

ing an increase in mode volume.

The quasipotential of this cavity (fig. A.3a) compared with that of a traditional overcoupled cavity (fig. A.3b) shows that allowing the cavity to have different barrier heights on each side of the defect enables both small mode volume (due to the strong mode confinement of the high barrier) and good overcoupling (due to the low barrier on the coupling side). On the other hand, the traditionally designed cavity must sacrifice confinement on the strong mirror side in order to enable good coupling on the weak mirror side.

In fig. A.3e, simulation data from cavities from several optimization runs illustrate the increasing mode volume for lower barriers. Each of the data points represents a single cavity with seven mirror unit cells on the left side of the cavity and between one and five mirror unit cells on the right side of the cavity. Given that the field decay rate is determined by the total barrier area, we define an effective barrier height as the directional quality factor Q_{x1} (dimensionless inverse coupling rate to the right) divided by the number of mirror unit cells.

A.1.3 Fabrication and Design Details

The nanophotonic cavities used for this work were fabricated with the methods described in [96]. One notable subtlety is that the fabrication procedure of a new cavity design must be tuned up for optimal resist thickness. The resist has to be thin enough to allow the holes to completely clear during the top-down etch but thick enough that the holes are protected during the angled etch. Historically, we found that fabrication of cavities with wildly varying hole sizes was challenging because the appropriate resist thickness for holes of a particular size would not work for holes of different size in the cavity. With this in mind, we restricted our design space to maintain identical hole dimensions throughout the defect and mirror regions. Then, the defect and mirror asymmetry were facilitated by a changing lattice constant.

As in [96], the cavity design is optimized using gradient ascent. However, the figure of merit in

this case is more complicated than simple Purcell enhancement so that cavity fitness additionally accounts for the cavity overcoupling. Therefore, the figure of merit used in the optimization which produced this experiment's design is

$$\text{Fitness} = \sqrt{\frac{Q_{\text{scat}}}{Q_{\text{wvg}}} * \frac{Q_{\text{left}}}{Q_{\text{right}}} * \frac{Q * Q_{\text{scat}}}{V^2} * e^{-(5^{-2}(\lambda_0 - \lambda)^2)}}$$

Here, $\frac{Q_{\text{scat}}}{Q_{\text{wvg}}}$ captures the relative waveguide damping rate versus scattering loss rate, with $Q_{\text{wvg}} = (Q_{\text{left}}^{-1} + Q_{\text{right}}^{-1})^{-1}$. $\frac{Q_{\text{left}}}{Q_{\text{right}}}$ captures how directional the waveguide damping is. $\frac{Q * Q_{\text{scat}}}{V^2}$, with $Q = (Q_{\text{wvg}}^{-1} + Q_{\text{scat}}^{-1})^{-1}$ is effectively Purcell enhancement but weighted to value improvements in scattering quality factor as well as total quality factor. Finally, $e^{-(5^{-2}(\lambda_0 - \lambda)^2)}$ is a smooth penalty that restricts the optimizer to find results near the target resonance wavelength. Although ad hoc, it was necessary to add the Gaussian resonance penalty to constrain the optimizer to produce useful results. Without the resonance penalty, the cavity mode volumes would artificially be reduced to zero because the optimizer would create cavities with resonances outside of the source bandwidth. Similar Gaussian penalties may be promising in future work for targeting specific cavity parameters, for example, a specific value of Q_{right}.

The cavity geometry parameters varied during optimization were the lattice constant on the left side (aL), the lattice constant on the right side (aR), the hole height in the mirror regions (hy), the hole width in the mirror region (hx), and the maximum defect (max_def). The functional form of the defect is identical to that described in[96] except we multiply the defect by a linear slope term to make a smooth transition between the different lattice constants on each side of the cavity.

The design and optimization process is computationally very expensive. Each full 3D cavity simulation is performed in Lumerical FDTD with a manual 12 nm resolution mesh region around the whole cavity as well as a high auto mesh accuracy = 5 for the remainder of the cavity simulation region. Simulations were performed using the Harvard University Research Computing cluster

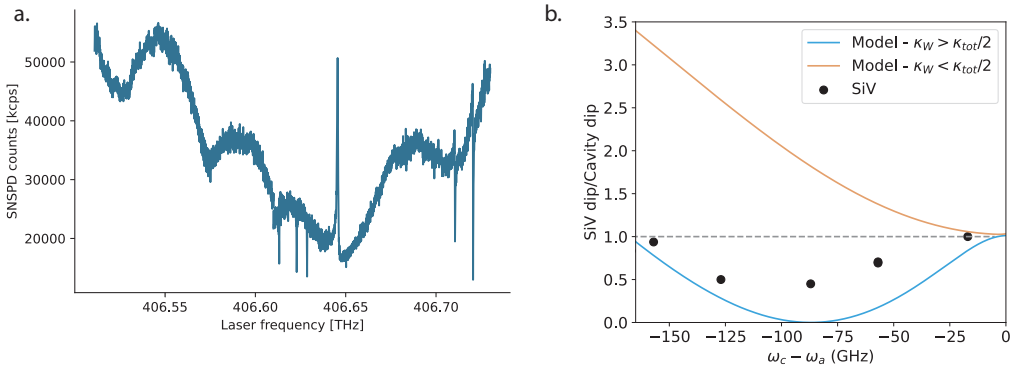


Figure A.4: (a) Reflection spectrum of the nanophotonic cavity coupled to six SiV centers. The fact that some SiV features dip below the cavity minimum is a signature feature of an overcoupled cavity. The slow modulation of the cavity reflection is due to interference created by reflections within the fiber network. (b) Measured minimum reflection of the SiV spectral feature normalized to the cavity dip versus its detuning from the cavity resonance. Dips below the cavity minimum (grey dashed line) are again observed, demonstrating overcoupling of a cavity. For comparison, theoretical SiV to cavity dip ratios, as obtained by fitting Eq. (A.4), for an equivalent overcoupled (blue) or undercoupled (orange) cavity are shown.

ODYSSEY (now known as CANNON). Though the gradient ascent proceeds serially, the time for each cavity simulation step is greatly reduced by exploiting the FDTD MPI. Typical optimizations are performed with 64 GB of RAM and up to 50 cores, reducing individual cavity simulation times from $\sim$ 20 minutes on a typical laptop to $\sim$ 3 minutes.

A.1.4 Cavity Fit / Overcoupling

Evidence of Overcoupling

In CQED, whether the cavity is undercoupled, critically coupled, or overcoupled qualitatively changes how the cavity interacts with incident light and thus how a coupled emitter can modify the cavity's spectrum. In this experiment, we probe the cavity in reflection, monitoring the intensity of the light that returns from the cavity. Of the three regimes, a critically coupled cavity is easiest to distinguish because it exhibits a characteristic full contrast reflection dip, a Lorentzian feature that

goes from the cavity reflection maximum when the probe light is off-resonant with the cavity to approximately zero photons reflected when the probe light is resonant with the cavity. This dip results from the destructive interference between the light directly reflected from the front mirror of the cavity and the reemitted cavity field. In reflection, a bare overcoupled and bare undercoupled cavity can have the same intensity spectrum, a Lorentzian dip that does not go to zero. However, the cause of the partial contrast dip is different for these complementary regimes. In the undercoupled cavity, the reflection dip does not go all the way to zero because the reemitted cavity field is always *weaker* than the directly reflected light. Thus, perfect destructive interference can never occur. On the other hand, for an overcoupled cavity, the reemitted cavity field always has a *larger* amplitude than the directly reflected light, and thus perfect destructive interference can never occur. Importantly, these distinct mechanisms result in different reflection spectra for overcoupled and undercoupled cavities coupled to emitters. Namely, only emitters in overcoupled cavities can produce spectral features that dip below the cavity minimum.

It is instructive to consider the electric field of resonant light reflected from a cavity. The reflected field of the bare cavity is $E_{\text{refl}} = 1 - \frac{2\kappa_w}{\kappa_w+\kappa_s}$. Thus, when $\kappa_s \neq \kappa_w$, there is not a full contrast dip. Putting an emitter in the cavity introduces a new loss channel which is g^2/γ when the emitter is resonant with the cavity. Then, the reflected field is $E_{\text{refl}} = 1 - \frac{2\kappa_w}{\kappa_w+\kappa_s+g^2/\gamma}$, and full contrast is possible when the cavity is overcoupled ($\kappa_w > \kappa_s$).

Figure A.4a shows a reflection spectrum of the nanophotonic cavity used for this experiment. Sharp reflection dips due to SiVs which dip below the cavity minimum are clearly observed. Thus, we conclude that this cavity is, in fact, overcoupled.

To provide further evidence of cavity overcoupling, the SiV's minimum reflection dip was measured as a function of its detuning from the cavity for a different device (Figure A.4b). The detuning was varied via gas tuning of the cavity[96]. In addition to observing the SiV dip below the cavity dip, we observe that the SiV reflection dip is minimized at a finite detuning away from the

cavity. This behavior is also indicative of an overcoupled cavity (see calculated model curves in Figure A.4b). We note the discrepancy between the theoretical overcoupled cavity dip versus detuning and the measured values is due to a combination of spectral diffusion, stray reflections, and dark counts limiting the minimum reflection observable in our system.

Estimation of Cooperativity

The total cavity damping rate κ_{tot} along with the waveguide damping rate κ_w were determined by fitting a broad cavity reflection spectrum taken with a spectrometer (Horiba iHR-550). For this fit, we assume the cavity is overcoupled (see section A.1.4). The single photon Rabi rate g was determined by fitting the reflection spectrum of the atom-cavity system near the frequency of the SiV's to the following intensity reflection coefficient expression. This expression is derived using input-output formalism applied to our Jaynes-Cummings Hamiltonian[55]:

$$\mathcal{R}(\omega) = \left| 1 - \frac{2\kappa_w}{2i(\omega - \omega_c) + \kappa_{\text{tot}} + 4g^2/(2i(\omega - \omega_a) + \gamma)} \right|^2 \tag{A.4}$$

Here, ω_C is the resonance frequency of the nanophotonic cavity, ω_a is the SiV resonance frequency, and γ is the linewidth of the SiV (FWHM). The complete set of cavity-QED parameters

$$\{g, \kappa, \gamma\} = 2\pi \times \{6.81(6)\,\text{GHz}, 328.00(343)\,\text{GHz}, 100\,\text{MHz}\} \tag{A.5}$$

gives rise to the fit shown in Fig. A.5 and results in cooperativity $C = \frac{4g^2}{\kappa\gamma} = 5.64 \pm 0.12$.

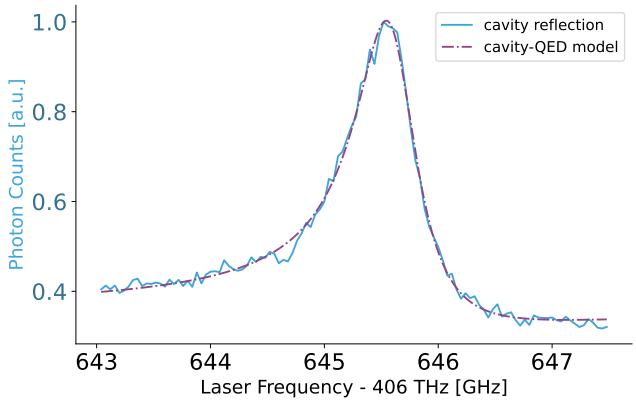


Figure A.5: Reflection spectrum of nanophotonic cavity coupled to a single SiV center and fit to Eq. (A.4).

A.2 Experimental setup

A.2.1 Hardware overview

The full system is detailed in Fig. A.6. Three primary lasers are used (2 Toptica DLC DL PRO, M Squared SolsTiS-2000-PSX-XF). Two lasers are used to resonantly drive the initialization and photon generation optical transitions, while the third is used to lock the filter cavity. All three were locked to a wavemeter (High Finesse WS7).

The nanophotonic cavity is situated in a dilution refrigerator (DR, BlueFors BF-LD250) with a base temperature of 50 mK. The DR is equipped with a superconducting vector magnet (American Magnets Inc.), a home-built free-space wide-field microscope with piezo positioners (SmarACT SLC-2430 and SLC-1720 series) and fiber feedthroughs. Tuning of the nanocavity resonance is performed using a gas condensation technique [137]. The SiV-cavity system is optically interrogated through the fiber network without any free-space optics [51].

Pulsing of the lasers is done via acousto-optic modulators (AOMs) controlled by a 2.4 GSa/s arbitrary waveform generator (AWG, Zurich Instruments HDAWG). The digital output lines of the

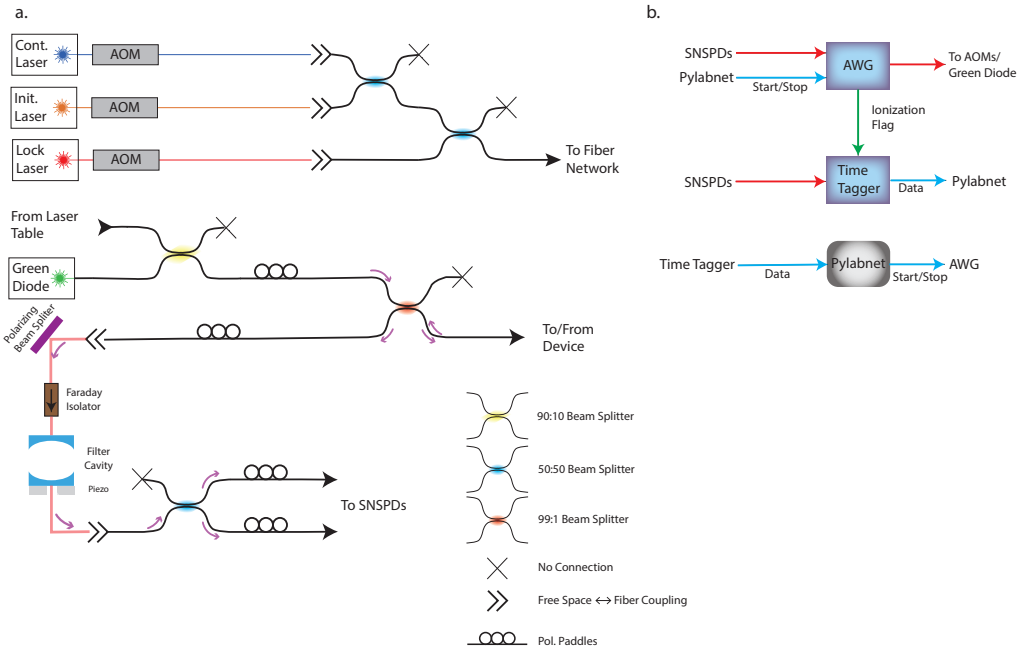


Figure A.6: Diagram of the (a) optical setup and (b) control flow used in this experiment.

AWG are connected to a custom buffer box to buffer the digital signals, which then modulate the AOMs.

To detect and process single photon events, superconducting nanowire single-photon detectors (SNSPDs, Photon Spot) are used. The outputs of the SNPSDs are routed to a time tagger (Swabian Instruments Time Tagger Ultra). The time tagger is used not only to count photon detection events but also to perform real time calculations of the cross-correlation of detection events between the two SNSPDs.

A.2.2 Software overview/24 hours run

In order to run the sequence for generating photons at a high duty cycle and process the data in real-time with a minimum software overhead, a hybrid approach using the custom python suite `pylabnet` [102] and logic on the AWG is performed. First, the python program locks the filter cavity to our desired transmission wavelength by turning on (via an AOM) a heavily attenuated lock laser tuned to our single photon frequency and modulating the voltage of the piezo in the cavity until a transmission maximum is achieved as measured by counts on the SNSPDs. The python program then signals to the AWG to run the single-photon generation sequence.

When signaled, the AWG applies the initialization and control pulses to the device via the AOMs. The AWG applies the pulses 250 times for a given sequence. In order to check if the SiV ionized during the applied pulses, a built-in counter gated to the single photon in the AWG is used to count the number of actually detected single photons within that sequence and compare to a minimum ionization threshold. If the number of detected single photons is below the ionization threshold, the SiV is assumed to be ionized, and a green diode laser is applied to the device for $500\mu s$ to return the SiV to the negative charge state. This enables ionization events to be detected quickly and have minimal impact on the total duty cycle of the source. The number of pulses within a given sequence is optimized to maximize the total duty cycle while still quickly catching ionization events to prevent

artificial degradation of the efficiency. This entire sequence is repeated 10000 times before the AWG finishes.

In order to communicate to the time tagger whether the last sequence of data passed the ionization check or not, a digital bit sent from the AWG to the time tagger is used as an ionization flag. The time tagger gates the incoming single photon counts based on the ionization flag, with an appropriate digital delay of approximately a full sequence length added onto the photon click events within the time tagging module so that the AWG will have updated the ionization flag for a given sequence before the events are processed by the time tagger.

Once the AWG runs the 10000 sequences, control is returned to the python program, which then polls the time tagger for the data, updates the GUI with the new data, and periodically relocks the filter cavity.

This enables real-time processing of the single photon events and autocorrelation measurements by the time tagging module without significantly impacting the duty cycle.

A.2.3 Systemic loss

The estimated losses in our system are listed in Table A.1. The initialization probability is estimated based on the ratio of the maximum single-photon efficiency achieved to twice the single-photon efficiency when no initialization is performed, where we assume the electronic-hole spin is thermalized to a 50-50 mixed state between each photon run.

The SiV to waveguide efficiency is calculated based on the Cavity QED parameters (see main text) estimated from fits of the cavity and SiV lineshapes as described previously. Namely, $\eta_s = p_c * p_w$ where $p_c = \frac{C}{C+1}$ is the probability of emission of a single photon into the cavity, and $p_w = \frac{\kappa_W}{\kappa_{tot}}$ is the probability that a photon in the cavity is coupled out to the waveguide. Note, that p_c assumes that the SiV is resonant with the cavity, which is acceptable given the small detuning used in this experiment. (See table 3.1 for cavity linewidth and detuning.)

Initialization probability	$0.8 - 1$
SiV to Waveguide Efficiency	0.62
Tapered Fiber Coupling Efficiency	0.7
Filtering Setup Efficiency	$0.5 - 0.6$
Fiber Network Efficiency	0.92
Detector Efficiency	$0.85 - 0.9$
Overall photon detection efficiency	$0.13 - 0.22$

Table A.1: Summary of system losses.

The tapered fiber coupling efficiency was measured directly by comparing the reflected power off of the device to the incident power, which is calibrated in the fiber network by substituting the nanophotonic cavity for a fiber coupled retroreflector.

The filtering setup efficiency and fiber network efficiency were measured directly. The uncertainty in the filtering setup efficiency is due to imperfect alignment, drifts in the cavity lock position between cavity relocking sequence, and spectral diffusion of the SiV.

A.3 Experimental results

A.3.1 Single Photon Efficiency Metric

Two different methods can be used to compute the efficiency of the single photon source. First, the ratio of detection events versus the total number of single-photon generation attempts made (i.e., number of times the control pulse was applied) can be used. Alternatively, as in fig. 4 of the main text, an exponential decay fit to the multi-photon event rates can be used.

In our experiment, the ratio gives an efficiency of 13.5%, whereas the exponential decay fit gives a slightly higher efficiency of 14.9%. This discrepancy can be explained by the fact that an ideal exponential decay relationship assumes that each photon detection event is mutually independent and uncorrelated with the other detection events. However, in this system, there is a slow MHz scale diffusion of the SiV qubit splitting over time. Due to the narrow filter cavity, this diffusion results

in changes to the detection efficiency. Therefore, there are short term correlations in the detection efficiencies of subsequent photons, making multi-photon detection events more likely than if there was no diffusion. Nevertheless, the efficiency value as determined by the exponential decay fit is the useful metric here because it better represents the multi-photon event rates which is a key figure of merit in photonic quantum information applications.

A.3.2 Experimental duty cycle

Given a control pulse repetition rate of 405 kHz, an average single-photon efficiency of 13.5%, and a single photon rate of 31 kHz, an average duty cycle (defined as the portion of time which single photons are actually being generated) of 57% is extracted.

We estimate that 56% of the down-time is due to the ionization of the SiV. This relatively long portion is due to the comparatively long pulse of green required to deionize the SiV (500μs). This can be improved in the future, potentially through the use of higher green power or using SiVs less prone to ionization.

Of the rest, we attribute a small portion (9%) to relocking of the Fabry Perot filter cavity. This can be improved through using persistent locking techniques at a detuned wavelength or through optimizing the stability of the cavity and its surrounding environment. The rest (35%) is attributed to the software overhead for the python portion of the experimental software, which is responsible for initially starting the sequence, reading the photon detection data from the time tagging module, and updating the GUI appropriately. This can be further improved through software optimization, particularly of the data transfer between the time tagger and the software through performing local processing of the data prior to transfer to the computer running the GUI.

A.3.3 Comparison to Weak Coherent States

To benchmark the gain from using the single photons generated in this work as opposed to a weak coherent source, we compared the gain in rate when using this source as opposed to a weak coherent source with a 100% duty cycle and an equivalent repetition rate and two photon-infidelity to our source, where the latter is defined by the ratio between the $n = 2$ and $n = 1$ components of the wavepacket. This gain is given by $D/g^2(0)$, where D is the duty cycle of the source demonstrated here, which gives a 35x enhancement.

To explicitly derive this, we note that for a coherent source, the probability of detection of two photons in the wavepacket is given by $P(n = 2)_{wcs} = \frac{1}{2}P(n = 1)^2_{wcs}$ where $P(n = 1)_{wcs}$ is the probability of detecting 1 photon in the wavepacket. Thus, we can estimate the infidelity from the higher order component (where we assume the source is weak enough such that higher photon number detection probabilities can be neglected) to be $1 - \mathcal{F}_{wcs} = \frac{P(n=2)}{P(n=1)} = \frac{1}{2}P(n = 1)_{wcs}$.

Similarly, for a single photon source with purity $g^2(0)$, the two photon component can be written as $P(n = 2)_{sps} \approx \frac{1}{2}g^2(0)P(n = 1)^2_{sps}$ [140], thus giving a corresponding infidelity of $1 - \mathcal{F}_{sps} = \frac{P(n=2)}{P(n=1)} = \frac{1}{2}g^2(0)P(n = 1)_{sps}$. We again note that we assume that higher photon component probabilities are negligible.

We now observe that setting $P(n = 1)_{wcs}$ so that the infidelity of the weak coherent source is equal to that of the single photon source ($\mathcal{F}_{wcs} = \mathcal{F}_{sps}$), requires that $P(n = 1)_{wcs} = g^2(0)P(n = 1)_{sps}$.

From this, if we assume a weak coherent source operated at the same repetition rate as the single photon source, a single photon rate enhancement of our single photon source versus a comparable weak coherent source could be estimated as $\frac{P(n=1)_{sps}}{P(n=1)_{wcs}} = 1/g^2(0)$. However, in order to provide a fair comparison, we note that our single photon source has a non-unity duty cycle D due to a variety of experimental imperfections (see A.3.2), whereas as typical coherent sources can be operated con-

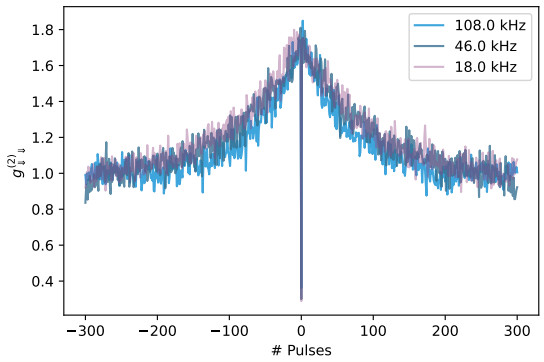


Figure A.7: ${g_{\Downarrow\Downarrow}}^{(2)}$ auto-correlation measurements of the photons emitted at frequency $\nu_{\Downarrow}$ at varying repetition rates, showing an approximately constant bunching time scale.

tinuously. Thus, a better estimation of the rate enhancement provided by the single photon source is given by $D\frac{P(n=1)_{sps}}{P(n=1)_{wcs}} = D/g^2(0)$. From this expression, we estimate the 35x gain reported in the main text.

A.4 Limitations

A.4.1 Si^{29} Readout Limited Lifetime

In the main text, a decay of the nuclear spin population after photon generation is observed through the photon autocorrelation measurements. The observed nuclear spin lifetime is significantly shorter than the expected. This suggests a shortening of the nuclear spin lifetime due to the photon generation process.

To further verify this, the photon bunching curve is measured at varying photon generation repetition rates (Fig. A.7). We see that despite the varying time between generated photons involved, the bunching decay constant is more or less constant as a function of the number of photons. This indicates that the photon generation process itself is inducing the nuclear spin flip.

The exact mechanism for this shortening of the nuclear spin lifetime via the generation of pho-

tons is still under investigation. Despite this, we note that the number of scattered photons is significantly higher than the largest measured multi-photon stream, and thus in the near term, the limit to generating large multi-photon entangled states will be efficiency as opposed to the lifetime of the nucleus.

A.4.2 Heating limited electron T_1

The photon generation scheme relies on applying a strong control pulse Ω_{cont} along the weak spin-flipping transition. Our nanophotonic cavity is embedded in a free-standing waveguide. It was shown previously that this free-standing structure is prone to microwave-driving induced heating[96]. In order to analyze the impact of the strong control pulse Ω_{control} on the lifetime of the excited state $|\uparrow\rangle$, we first carry out a optical-pumping based lifetime measurement[98]. This is done by applying a pulse along the $|\downarrow'\rangle \rightarrow |\downarrow'\rangle$ transition, which optically pumps the electron into the $|\downarrow\rangle$ state (Fig. A.8 (a)). After a dark time τ, this optical pumping pulse is repeated. The timetrace of the SNSPD counts during this sequence (Fig. A.8 (b)) show a fluorescence peak, which decays over the course of the pulse. This decay is indicative of the optical pumping from $|\downarrow\rangle$ to $|\uparrow\rangle$. If the electron spin has relaxed back to $|\uparrow\rangle$ during the dark period, the second application of the optical pumping pulse will show a similar decaying fluorescence feature. Thus, by plotting the ratio of the counts of the first and second optical pumping pulse, the lifetime of the excited state $|\uparrow\rangle$ can be extracted (Fig. A.8 (c)).

To analyze the impact of a strong control pulse Ω_{control} on the electron lifetime, we re-run the T_1 measurement while applying a strong pulse during the dark time. This pulse is identical to the Ω_{control} pulse used to generate single photons with the exception of the frequency, which is detuned from any optical SiV transition. This is done to ensure that the strong pulse does not resonantly interact with the SiV. We can see that upon application of this strong pulse, the measured T_1 decreases more than three-fold. This decrease in T_1 persists even if the repetition rate is lowered by an order

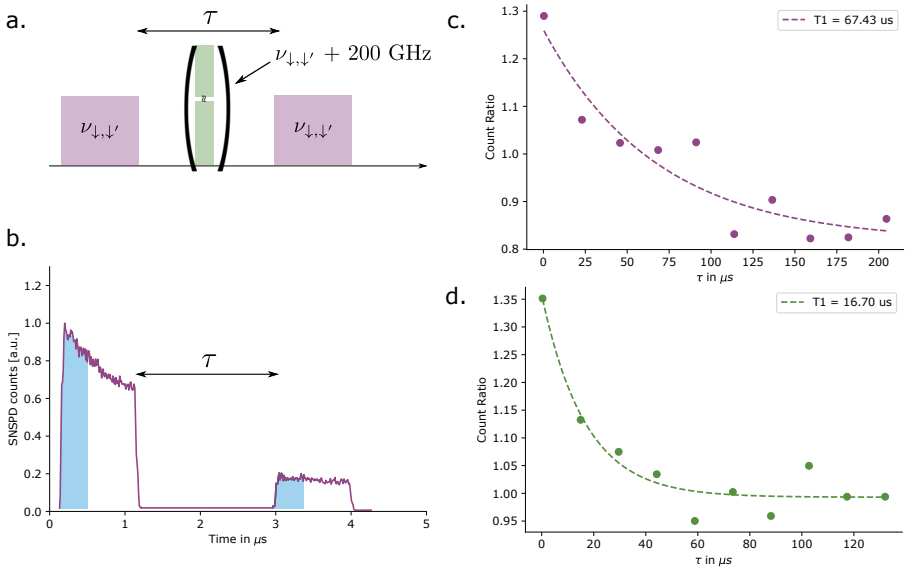


Figure A.8: (a) Pulse sequence used for T_1 measurements. A pulse along the optical spin-conserving transition optically pumps the electron spin from the $|\downarrow\rangle$ to the $|\uparrow\rangle$ level. After a dark period τ, the same pumping pulse is applied. An optional strong off-resonant pulse is applied to emulate the heating induced by the strong control pulse Ω_{control}. (b) Exemplary time trace resulting from the pulse sequence in (a). To probe relaxation from $|\uparrow\rangle$ to $|\downarrow\rangle$, the ratio of the two shaded regions is plotted for different dark times τ both assuming no heating pulse (c) and with applied heating pulse (d). The spin-lifetime T_1 is extracted by fitting the obtained data to an exponential proportional to $\exp(-t/T_1)$.

of magnitude. Since we can exclude resonant interactions, we attribute this decrease in T_1 to instantaneous heating induced by the control laser pulse. During single-photon generation, this decrease in T_1 can be overcome by ensuring the single photon is generated on timescales faster than T_1 (see discussion in 3.7.3). For application where radio-frequency control of the ^{29}Si nucleus is needed, this heating induced deterioration of T_1 will need to be overcome in order to allow for nuclear operations which extend over multiple μs.

A.5 High temperature operation

The ability to generate single photons with the SiV at elevated temperatures ($\sim$ 1K) would significantly relax the cryogenic experimental overhead required for operating the source. Normally SiV

quantum memories cannot be operated at these temperatures due to their susceptibility to phonon processes. Interestingly, the photon generation protocol demonstrated here is fairly immune to these requirements due to the ability to generate short photons, and thus, theoretically, should be operable at 1K.

There are three main sources of degradation of the SiV's spin properties at 1K. First, the T_2* of the spin levels significantly degrades. We estimate it to be around $\sim$ 400 ns based on extrapolation from data from [54]. With generated photons with a width of $\sim$ 20 ns, and assuming a Markovian-limited T_2*, a small increase of the linewidth 2.5% is expected based on the convolution of the spectral intensity of the Gaussian photon and the dephasing. The second potential pathway for degradation is the drop in the spin lifetime, extrapolated to be $\sim$ 1.2μs. Given our photon width of 20 ns, we would expect approximately a population decrease of $\sim$ 2%, which would degrade the efficiency by that amount and also potentially limit the $g^2(0)$ similarly. Finally, we expect an increased population trapped in the upper branch of the ground state manifold, which would decrease the efficiency of the source. Given a ground state splitting of 46GHz, we would expect a population of $\sim$ 11% in the steady state at 1K, which is the largest impact of operating at higher temperatures but is not prohibitive and could be improved via optically pumping the upper branch during initialization.

Thus even given the degraded spin properties, we would still be able to generate bandwidth-matched $\sim$ 20 ns photons at 1K, with only a small degradation in efficiency, highlighting the versatility of this protocol.

B

Supporting Material for Chapter 3

B.1 Control sequence

The control sequence for SiV control for nuclear-nuclear entanglement generation is summarized in Fig. B.1. Hardware synchronization and MW- and RF-pulse generation are achieved using two Zurich Instrument HDAWG8 2.4 GSa/s AWG (HDAWG). One of the two HDAWGs acts as the controller device and is labeled control system in Fig. B.1 a. It provides the central timing sequence,

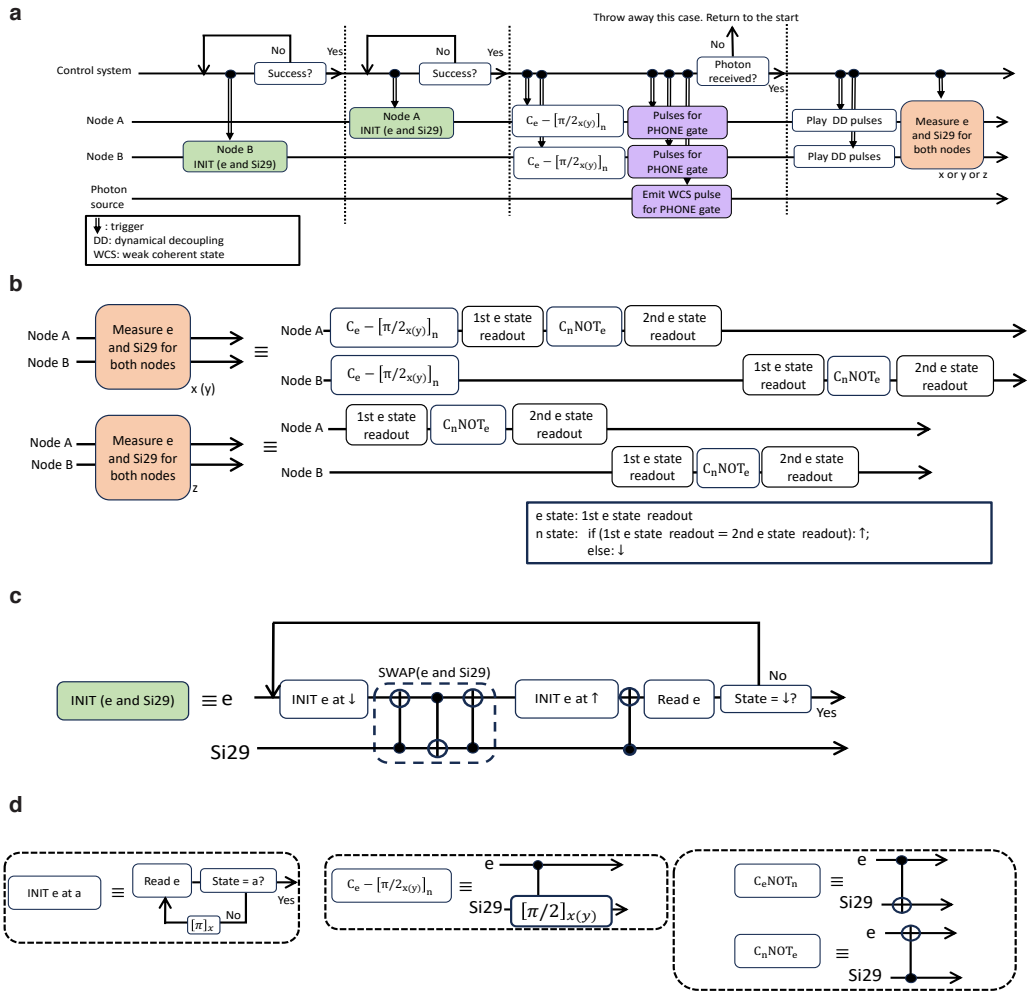
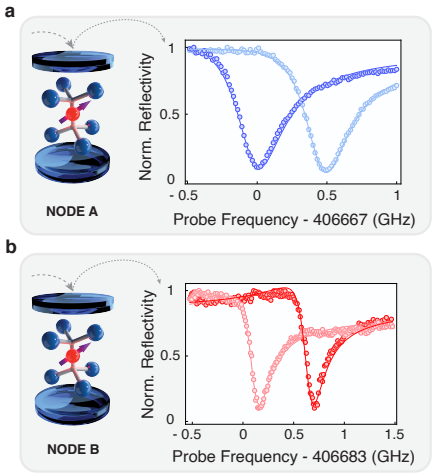


Figure B.1: Flow chart for experimental control sequence. a. Summarizes the overall workflow for nucleus-nucleus entanglement through PHONE gates. **b.** Detailed control sequence for the readout of the electron and the nuclear state. The electron state readout (e state readout in the figure) is performed by detecting photon numbers reflected back from nanophotonic cavities during a read laser pulse. The nuclear state is read by checking if a $C_n NOT_e$-pulse flips the electron's state [53]. **c.** Detailed control sequence of initialization. The nuclear initialization is done by first initializing the electron and then swapping the electron and nuclear state. **d.** Schematic representations displayed in a.-c.



$\kappa_{tot}/2\pi$	148(1) GHz
$\kappa_{in}/2\pi$	120(4) GHz
$g/2\pi$	6.8(0) GHz
w_e	0.52 GHz
w_c	406.536(9) THz
w_{SiV}	406.667(1) THz
C	12.4(9)

$\kappa_{tot}/2\pi$	258(1) GHz
$\kappa_{in}/2\pi$	192(2) GHz
$g/2\pi$	3(1) GHz
w_e	0.53 GHz
w_c	406.641(3) THz
w_{SiV}	406.68308(7) THz
C	1.5(8)

Figure B.2: Cavity-QED parameters a. Node A, and **b.** Node B. Left: Reflection spectra of the cavity-QED system for two electronic spin states. Right: Values of cavity-QED parameters. ω_e is the frequency splitting between the two electronic spin-states.

conditional feedback, and AOM control. The second HDAWG acts as worker device, standing by to be triggered by the controller HDAWG to play requested pulses. For more detailed sub-sequences, including electron and nuclear state measurement and initialization, see Fig. B.1 b - d.

B.2 Cavity-QED parameters

One of the strengths of the SiV platform is the efficient optical interface. The efficiency of the interface is due to three characteristics of the system. The first one is the strong coupling between the emitter and sub-wavelength mode of the optical cavity, which results in high cooperativity $C = \frac{4g^2}{\kappa_{\text{tot}}\gamma} > 1$. Here, g is the single-photon Rabi frequency, κ_{tot} the total cavity decay rate, and γ is the bare SiV linewidth. Decay rates and linewidths are expressed as full widths at half max (FWHM). The second one is our ability to design and fabricate overcoupled one-sided cavities. And, finally, the third one is the efficient mode matching between the cavity mode and the tapered input fiber. The reflection amplitude of light for the cavity-coupled SiV at frequency ω can be ex-

pressed as:

$$\text{Reflection}(\omega) = 1 - \frac{\kappa_{\text{in}}}{i(\omega - \omega_c) + \kappa_{\text{tot}}/2 + g^2/(i(\omega - \omega_{SiV}) + \gamma/2)} \tag{B.1}$$

Here, κ_{in} is the coupling rate of the cavity into the in-coupling port, and $\omega_{SiV(c)}$ is the resonance frequency of the SiV (cavity). The cavity-QED parameters and reflection data for the SiVs used in node A and node B are shown in Fig. B.2. The design and fabrication of the nanophotonic cavity is described in 122, 96.

B.3 Contrast error distillation

Electron-electron and nuclear-nuclear entanglement are based on state-dependent electron reflectivity. Any reflection of the nominally non-reflective state contributes to Bell state infidelities, an error source we denote contrast error. This error source contributes differently to $|\Phi_{ee}\rangle^+$ and $|\Phi_{ee}\rangle^-$, so that selecting for the heralding events for a specific Bell state allows for a higher final Bell state fidelity.

We assume that the reflective electron state has unity reflectivity, while the nominally non-reflective electron state has small non-zero reflectivity r_A (r_B) in node A (B). The photon and electrons are prepared in $|+\rangle$ and $|{\rightarrow}{\rightarrow}\rangle$, respectively. After performing the $e - \gamma$ gate at the first node, the state becomes

$$|\gamma, e_A\rangle = \frac{1}{\sqrt{2}}(|e\downarrow_e^A\rangle + |l\uparrow_e^A\rangle + r_A(|e\uparrow_e^A\rangle + |l\downarrow_e^A\rangle)). \tag{B.2}$$

We use γ and $e_{A(B)}$ to denote photonic and electron states in node A (B). The photonic qubit then

interacts with the second node, resulting in the state

$$\begin{aligned}|\gamma, e_A, e_B\rangle =& \frac{1}{\sqrt{2}}(|e\downarrow_e^A |\downarrow_e^B\rangle\rangle + |l\uparrow_e^A\uparrow_e^B\rangle + r_A(|e\uparrow_e^A\downarrow_e^B\rangle + |l\downarrow_e^A\uparrow_e^B\rangle)+ \\ &+ r_B(|e\downarrow_e^A\uparrow_e^B\rangle + |l\uparrow_e^A\downarrow_e^B\rangle) + r_A r_B(|e\uparrow_e^A\uparrow_e^B\rangle + |l\downarrow_e^A\downarrow_e^B\rangle)).\end{aligned} \tag{B.3}$$

Then, measuring the photon in the $|\pm\rangle$ basis heralds a successful entanglement event. We define $|e_A, e_B\rangle_\pm$ as the resulting two-node state after measuring the photon in the $|\pm\rangle$ state:

$$\begin{aligned}|e_A, e_B\rangle_+ \propto& (1 + r_A r_B)\frac{1}{\sqrt{2}}(|\uparrow_e^A\uparrow_e^B\rangle + |\downarrow_e^A\downarrow_e^B\rangle)+ \\ &(r_A + r_B)\frac{1}{\sqrt{2}}(|\uparrow_e^A\downarrow_e^B\rangle + |\downarrow_e^A\uparrow_e^B\rangle),\end{aligned} \tag{B.4}$$

and

$$\begin{aligned}|e_A, e_B\rangle_- \propto& (1 - r_A r_B)\frac{1}{\sqrt{2}}(|\uparrow_e^A\uparrow_e^B\rangle - |\downarrow_e^A\downarrow_e^B\rangle)+ \\ &(r_B - r_A)\frac{1}{\sqrt{2}}(|\uparrow_e^A\downarrow_e^B\rangle + |\downarrow_e^A\uparrow_e^B\rangle).\end{aligned} \tag{B.5}$$

Here, both states are not normalized. Thus, the infidelity due to the contrast error would then be

$$\begin{aligned}\varepsilon_+ &= (r_A + r_B)^2/((r_A + r_B)^2 + (1 + r_A r_B)^2) \sim (r_A + r_B)^2 \\ \varepsilon_- &= (r_A - r_B)^2/((r_A - r_B)^2 + (1 - r_A r_B)^2) \sim (r_A - r_B)^2\end{aligned} \tag{B.6}$$

where the approximation is done by only considering the lowest order errors in r_A, r_B. We write $r_A = |r_A|e^{i\varphi_A}$ and $r_B = |r_B|e^{i\varphi_B}$, and based on the cavity-QED parameters of our system get $\varphi_A \approx \varphi_B \approx \pi$. In this case, ε_- should be less than ε_+ and thus contrast errors in $|e_A, e_B\rangle_-$ are suppressed. For nuclear-nuclear entanglement generation, this analysis can be carried out analogously and will also result in a suppression of contrast errors for states heralded by the TDI measuring $|-\rangle$.

B.4 Bell state fidelity and error calculation

Both Bell state fidelity and the sample standard deviation of the Bell state fidelity can be obtained from the measured ZZ, XX, and YY correlators. The Bell state fidelity $\mathcal{F}_\rho^{|\Phi^\pm\rangle}$ of an arbitrary quantum state ρ with respect to the Bell states $|\Phi^\pm\rangle$ can be expressed as $\mathcal{F}_\rho^{|\Phi^\pm\rangle} = \frac{1}{2}P_{zz} + \frac{1}{4}P_{xx} + \frac{1}{4}P_{yy}$ [53], with

$$
\begin{aligned}
P_{zz} &\equiv p_{zz}^{00} + p_{zz}^{11} \\
P_{xx} &\equiv \begin{cases} p_{xx}^{01} + p_{xx}^{10} - p_{xx}^{00} - p_{xx}^{11}, & \text{for } |\Phi^-\rangle \\ p_{xx}^{00} + p_{xx}^{11} - p_{xx}^{01} - p_{xx}^{10}, & \text{for } |\Phi^+\rangle \end{cases} \\
P_{yy} &\equiv \begin{cases} p_{yy}^{00} + p_{yy}^{11} - p_{yy}^{01} - p_{yy}^{10}, & \text{for } |\Phi^-\rangle \\ p_{yy}^{01} + p_{yy}^{10} - p_{yy}^{00} - p_{yy}^{11}, & \text{for } |\Phi^+\rangle. \end{cases}
\end{aligned}
$$

Here, $p_{nn}^{ij}, nn \in \{zz, xx, yy\}$ describe the probabilities obtaining the various measurement outcomes $(i,j) \in \{0,1\}^2$ for each measurement basis. Now, the sample variance $\sigma_{\mathcal{F}}^2$ of the Bell state fidelity can be expressed as $\sigma_{\mathcal{F}}^2 = \left(\frac{1}{2}\sigma_{zz}\right)^2 + \left(\frac{1}{4}\sigma_{xx}\right)^2 + \left(\frac{1}{4}\sigma_{yy}\right)^2$, with $\sigma_{nn\in\{zz,xx,yy\}}^2$ describing the sample variance of $P_{nn\in\{zz,xx,yy\}}$. Using the fact that $P_{nn\in\{zz,xx,yy\}}$ follows a binominal distribution, we can use the following expression of the sample variance of a binominally distributed variable with success probability p: $\sigma^2(N,p) = \frac{p(1-p)}{N}$, where N is the sample size. Noting that for $P_{zz}, p = P_{zz}$, while for P_{xx} and $P_{yy}, p = \frac{P_{nn\in\{xx,yy\}}+1}{2}$, we can finally express the sample standard deviation of the Bell state fidelity as:

$$
\sigma_{\mathcal{F}} = \sqrt{\frac{1}{4}\frac{P_{zz}(1-P_{zz})}{N_{zz}} + \frac{1}{16}\frac{(1+P_{xx})(1-P_{xx})}{N_{xx}} + \frac{1}{16}\frac{(1+P_{yy})(1-P_{yy})}{N_{yy}}} \tag{B.7}
$$

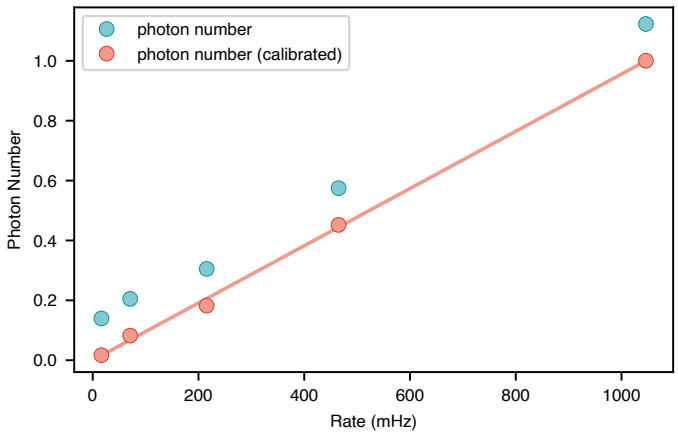


Figure B.3: Average photon number per photonic qubit versus success rate. The plot shows uncalibrated values (blue), and values where the MW-pulse infidelity has been compensated (red). The mean photon number is measured at node A's SiV. The solid line corresponds to the fitted linear relationship between μ and the success rate and is used for error simulations.

Here, $N_{nn\in\{zz,xx,yy\}}$ is the sample size for the measurements in the zz, xx, and yy basis.

B.5 Fidelity budgets

Table B.1 and Table B.2 summarize the error contributions from various sources. The individual-node errors, optical contrasts, and TDI locking performance can be directly measured, and their contributions to our target entangled states are analyzed by numerical simulation.

B.5.1 Electron-electron entanglement

The numerical simulation and error-budget analysis here are performed in two steps: extracting the average photon numbers per photonic qubit (μ) of experiments and running a simulation model for a given photon number. For photon number extraction, the analysis is carried out by observing the electron spin population resulting from a X basis e-γ gate: the electron spin should end up in $|\downarrow_e\rangle$ if no photon arrives, while it ends up being in an equally mixed state of $|\uparrow_e\rangle$ and $|\downarrow_e\rangle$ if ≥ 1 photon

arrives. Based on the coherent state's Poisson distribution, we can then estimate μ. We subtract the infidelity resulting from imperfect MW gates, correcting for the offset observed in the μ-rate plot (Fig. B.3). We then feed this photon number into a model that considers four different sources of errors: multiple photon error, imperfect optical contrast, matter-qubit operation error, and TDI locking error. The results are shown in Table B.1.

Error source	Individual-node error	Error contribution $\|\Phi_{ee}^{-}\rangle$	Error contribution $\|\Phi_{ee}^{+}\rangle$
Microwave pulse error	2.5 ± 1.5 % (A), 3.5 ± 0.5 % (B)	12.6 ± 5.0 %	7.3 ± 2.9 %
Optical contrast error	4.3 ± 1.3 (A), 8.2 ± 1.8 % (B)	2.5 ± 0.6 %	13.0 ± 2.3 %
Multi-photon error ($\mu = 0.02$)	-	0.8 %	0.3 %
TDI locking error	-	2.0 ± 1.0 %	2.0 ± 1.0 %
Total expected error	-	16.8 ± 6.4 %	25.9 ± 5.9 %
Total observed error	-	13.8 ± 2.9 %	26.0 ± 3.5 %

Table B.1: Error budget for electron-electron entanglement. μ: mean photon number per photonic qubit. Uncertainties for observed errors are one standard deviation. Uncertainties in the remaining rows are estimation ranges.

B.5.2 Nucleus-nucleus entanglement

Here, the analysis is carried out similarly as in the above subsection, with two differences: microwave pulse errors and nuclear readout assignment errors. MW pulse errors contribute differently due to the difference between e-γ and PHONE gate. Furthermore, first-order MW errors are detected with the electron flag qubit, resulting in a lower MW error contribution. To read out nuclear states, a $C_n NOT_e$ gate is applied in the middle of two electron readouts, with the measured nuclear state depending on whether the electron state has flipped or not. However, using this approach, the readout fidelity is affected by $C_n NOT_e$ gate fidelity, which results in a nuclear readout assignment error. The results of the error analysis are shown in Table B.2.

Error source	Individual-Node Error	Error contribution $\|\Phi_{nn}^{-}\rangle^{ED}$	Error contribution $\|\Phi_{nn}^{-}\rangle^{raw}$
Microwave pulse error	$1.8 \pm 0.3\%$ (A), $7.8 \pm 0.3\,\%$ (B)	≈ 0	$22.1 \pm 2.9\,\%$
Optical contrast error	$3.5 \pm 0.5\,\%$ (A), $10.4 \pm 2.1\,\%$ (B)	$3.9 \pm 0.9\,\%$	$3.2 \pm 0.7\,\%$
Multi-photon error ($\mu = 0.16$)	-	$6.5\,\%$	$1.4\,\%$
TDI locking error	-	$2.0 \pm 1.0\,\%$	$2.0 \pm 1.0\,\%$
Nuclear readout assignment error	$1.5 \pm 0.5\,\%$ (A), $6.0 \pm 1.0\,\%$ (B)	$4.3 \pm 0.5\,\%$	$3.4 \pm 0.4\%$
Total expected error	-	$18.4 \pm 3.1\,\%$	$37.0 \pm 5.0\,\%$
Total observed error	-	$22.6 \pm 5.0\,\%$	$36.7 \pm 5.0\,\%$

Table B.2: Error budget for nucleus-nucleus entanglement. μ: mean photon number per photonic qubit. Uncertainties for observed errors are one standard deviation. Uncertainties in the remaining rows are estimation ranges.

B.6 Efficiency breakdown

The optical losses in our system are broken down in Table B.3. The losses can be seen to come from three major categories. The first is conversion loss to overcome the inhomogeneous distribution, either via visible electro-optic frequency shifting or telecom frequency conversion. The former can be improved through more complex electro-optic shifting schemes, such as serrodyning with high-bandwidth, low-voltage modulators, or shifting using coupled rings. The latter can be improved through further optimization of the conversion setup. Beyond this, the integration of direct strain control of the individual SiVs could be used to tune their transitions and through this overcome the inhomogeneous distribution without any form of photon conversion.

The second major category of losses is our spin photon gate efficiencies, which together lead to almost an order of magnitude penalty on the efficiency. The largest hit to the individual spin-photon gate efficiency is due to the intrinsic 50% penalty from carving the final spin-photon entangled state from the initial product state. This can be overcome using more complex spin-photon cavity architectures such as phase-based gates using overcoupled cavities or symmetric cavities where photons are collected both on the reflection and transmission ports.

The final category of loss is the sum of the insertion loss of the rest of the components in the system (fiber coupling, circulator, etc.). Beyond improving the insertion loss of each individual

	Efficiency
Fiber coupling	60% (Node A) $60\%^2$ (Node B)
Cavity reflectance	70% (Node A) 60% (Node B)
Node A free space setup	70 %
Visible frequency shifting	7.4 %
Telecom frequency conversion	5.4 %
Circulator	$70\%^2$
SNSPD efficiency	80% and 95%
All photonic link efficiency (visible frequency shifting)	0.20 %
All photonic link efficiency (telecom frequency conversion)	0.15 %
Spin-photon gate	50%
$\|+\rangle$ / $\|-\rangle$ detection	50%
WCS mean photon number (variable)	0.1
Success probability η (visible frequency shifting)	5.0×10^{-5}
Success probability η (telecom frequency conversion)	3.7×10^{-5}

Table B.3: Estimation of photonic link efficiency and success probability in the two-node quantum network. Efficiencies with ^{2}-superscript enter twice due to our serial network configuration. The photonic link efficiency describes the full insertion loss of our system. The success probability includes the photonic link efficiency and protocol-specific loss channels. Here, the mean photon number of the WCS has been set to a representative value of 0.1.

component of the system through additional optimization, the net penalty from these components can be alleviated by changing the path architecture from a serial one as used in this work, to a parallel one where a photon is split into two paths, interacts with both nodes and then is re-interfered and measured to generate entanglement, as done in previous experiments[40,43,38,35]. This parallel architecture ensures that the loss of certain components that are intrinsic to either of the two nodes (such as fiber coupling) only penalizes the overall efficiency a single time as opposed to the double penalty incurred in the serial architecture. On the other side, moving to a parallel architecture using single-photon schemes would increase the experimental complexity due to the need to stabilize two fiber paths, which is especially challenging in deployed fiber environments.

Table B.3 does list the estimated photonic link efficiency, corresponding to the insertion loss of

our system, and the final success probability, including the protocol-specific loss channels such as losses due to the spin-photon gates. The success probability also accounts for the efficiency hit due to the mean photon number μ of the WCS used as input in this work. To improve this aspect of the work, high-efficiency deterministic single photon sources or heralded and fed forward single photon sources made from photon-pair sources could be used.

B.7 System improvements

The generated electronic Bell state error sources can be grouped into four categories: TDI locking error, optical contrast error, MW pulse error, and multi-photon error. There is no fundamental lower bound to the TDI locking error, and a straightforward improvement of the TDI design, including passive locking and environmental isolation through integration in a vacuum box, could reduce this error source to near-zero. The optical contrast error can be significantly suppressed as well. In principle, infinite contrast (and thus zero contrast error) can be achieved for any overcoupled SiV-cavity system with a cooperativity greater than one. In practice, SiV optical resonance diffusion and stray reflections can lower the contrast, though higher cooperativities mitigate these effects. With reasonable pre-selection and overcoupled SiV-cavity systems with cooperativities higher than 10, optical contrasts of 1:50 are achievable, which would reduce this error source to $\sim$ 4% for $|\Phi^+_{ee}\rangle$ and $< 1\%$ for $|\Phi^-_{ee}\rangle$.

We further note that the SiV at node B was coupled to a nearby ^{13}C that caused a reduction in MW pulse fidelities. MW pulses are limited by spectral diffusion, spin-state decoherence, as well as MW driving-induced heating. Another constraint on MW pulses is the ^{29}Si state-dependent splitting of the electron MW transition [53]. This limits how short a MW pulse can be to selectively drive one transition to about 13 ns to apply C_nNOT_e gates, or requires very large Rabi frequencies ($\Omega \gg 33$ MHz) to effectively drive both transitions to apply an unconditional NOT_e gate. While

MW gate errors of $\sim$ 0.1% have previously been demonstrated[53], solid state microscopic environmental noise and frequency-dependent noise differs from emitter to emitter, imposing different error limits for different emitters. However, implementing pulse optimization techniques could allow reproduceable and deterministic reduction of MW gate errors below 1%.

When using WCS as single photons, the error scales as $\sim \mu$, where μ is the average photon number of the WCS. To reach increasingly higher fidelities requires the use of increasingly lower photon numbers, which would cause a significant reduction in Bell state generation rate. If we replace the WCS with a single photon source, there would not be a need to sacrifice entanglement generation efficiency for fidelity. In this case, the multi-photon error would scale as the single photon source second order correlation at zero delay $\sim g^{(2)}(0)$. A state-of-the-art single photon source at the frequency and bandwidth of the SiV has previously shown to achieve $g^{(2)}(0) = 1.68\%$[122]. Further improving this fidelity would require improved single photon sources at the frequency and bandwidth of the SiV. Compiling all these improvements, fidelities of around 0.95 could be achievable in the near future, with even higher fidelities reachable in the longer term with higher cooperativity SiV-cavity systems and improved single photon sources.

Additionally to using a single photon source, the success rates of entanglement generation can further be improved by improving fiber coupling efficiency, with 95% coupling efficiency shown in previous work[64]. Higher cooperativity SiV-cavity systems could also enhance the cavity reflectance to 90%[64]. This could further boost the success rate by a factor of 7.7, yielding success rates of $\sim$ 8 Hz. Access to strain tuning would remove the need for frequency shifting, further increasing the success rate by a factor of 13.5, resulting in an success rate rate of 100 Hz.

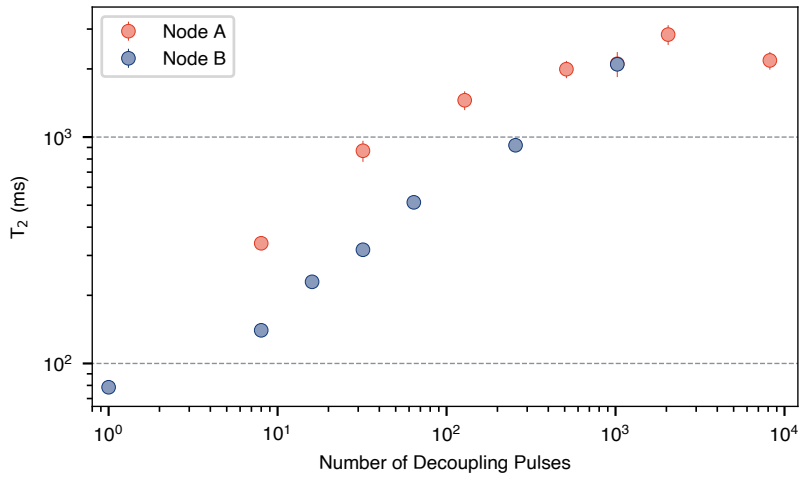


Figure B.4: T_2 coherence times of the ^{29}Si nuclear spins. Fitted T_2 coherence times of the ^{29}Si nuclear spin as a function of the number of decoupling pulses for node A and node B. The decoupling sequences are of the form of XY8-N, where N is the number of successive XY8 sequences. Error-bars are one s.d. Dashed lines indicate 0.1 s, and 1 s.

B.8 SiV properties

The SiV properties for each node are given in Table B.4. The SiVs were picked from a larger measured distribution of SiVs for a combination of desirable device cooperativity, SiV coherence time, and SiV optical stability. The T_2 coherence times of the SiV electron and nucleus can be extended with decoupling sequences of increasing length of the form XY8-N, where an XY8 sequence is repeated N times. For a given XY8 sequence, the coherence time of the nuclear spin is about 1000 times higher than for the electron spin due to the smaller nuclear magnetic dipole moment. The maximum achieved T_2 for the nuclear spin is about 2 seconds for XY8-128 (Fig. B.4). More XY8 sequences do not seem to further increase the T_2, which points to a Markovian noise source limiting the coherence time to about 2 seconds. This is likely due to coupling to phonons through the electron spin.

	Node A	Node B
τ_e	30 ns	30 ns
τ_n	∼15 µs	∼21 µs
$T_{2,e}$ XY8-1	125 µs	134 µs
$T_{2,n}$ XY8-1	339 ms	140 ms
$T_{2,n}$ XY8-128	2.11 s	2.1 s
Magnetic field	0.39 T	0.4 T

Table B.4: Node A and Node B SiV parameters. $\tau_{e,(n)}$ is the $\text{NOT}_{e,(n)}$-gate duration for the electron (nucleus).

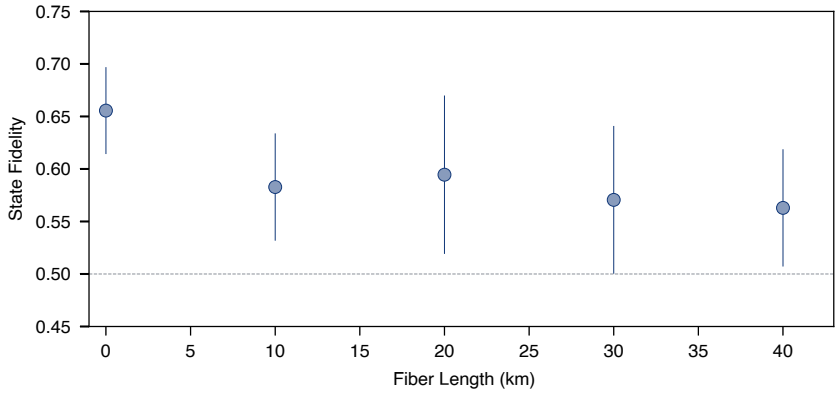


Figure B.5: $|\Phi^-_{\text{nn}}\rangle$ Bell state fidelities for telecom conversion experiment. Bell state fidelities of $|\Phi^-_{\text{nn}}\rangle^{\text{raw}}$ state without error-detection for different fiber spool lengths. The dashed line indicates the classical limit. Error-bars are one s.d.

B.9 Entanglement results additional data

Figure B.7 shows Bell state fidelities for the $|\Phi^+_{\text{nn}}\rangle$ state for different nuclear decoupling times, both error-detected and raw. The success rates for this measurement are given in Table B.5. Figure B.5 shows the Bell state fidelities of the raw $|\Phi^-_{\text{nn}}\rangle$ state for nuclear-nuclear entanglement generation through spools of up to 40 km of low-loss telecom fiber. Figure B.6 shows the Bell state fidelities for $|\Phi^+_{\text{nn}}\rangle$ for the same measurement, both error-detected and raw. The success rates for this measurement are given in Table B.6. Errors due to imperfect reflectance contrast preferentially affect the $|\Phi^+_{\text{nn}}\rangle$ state, see section III. The magnitude of this type of error slowly varies over time due to spectral diffusion of the SiV, macroscopic shifts of the resonance frequency of the nanophotonic cavity,

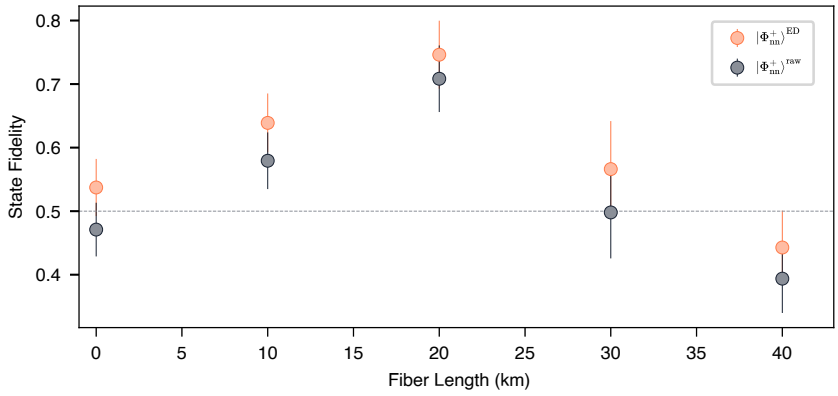


Figure B.6: $|\Phi^+_{nn}\rangle$ Bell state fidelities for telecom conversion experiment. Bell state fidelities of $|\Phi^+_{nn}\rangle$ state with (orange) and without (grey) error-detection for different fiber spool lengths. The dashed line indicates the classical limit. Error-bars are one s.d.

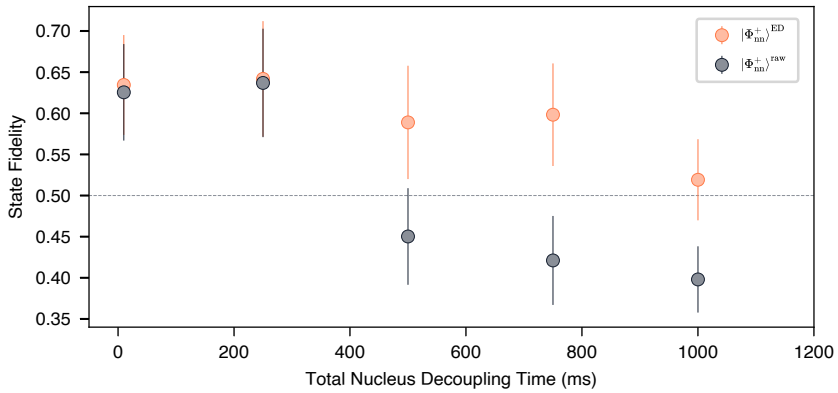


Figure B.7: $|\Phi^+_{nn}\rangle$ Bell state fidelities for decoupling experiment. Fidelities of $|\Phi^+_{nn}\rangle$ state with (orange) and without (grey) error-detection for different total decoupling times. The dashed line indicates the classical limit. Error-bars are one s.d.

Decoupling duration (ms)	Average Rate ED	Rate $\left\|\Phi^-_{nn}\right\rangle^{ED}$	Rate $\left\|\Phi^+_{nn}\right\rangle^{ED}$
10	8.3	4.3	4.0
250	3.4	1.6	1.8
500	10.0	4.8	5.2
750	2.0	1.0	1.0
1000	6.4	3.2	3.2

Table B.5: Rates for decoupling experiment. Summary of success rates for nuclear-nuclear entanglement generation. Rates are given in mHz.

Fiber length (km)	Average Rate ED	Rate $\left\|\Phi^-_{nn}\right\rangle^{ED}$	Rate $\left\|\Phi^+_{nn}\right\rangle^{ED}$
0	8.2	3.7	4.5
10	5.8	2.5	3.3
20	2.9	1.1	1.8
30	5.0	2.5	2.5
40	1.5	0.7	0.8
35 (deployed)	0.23	0.10	0.14

Table B.6: Rates for telecom conversion experiment. Summary of success rates for nuclear-nuclear entanglement generation via spools of low-loss telecom fiber and the deployed 35 km fiber loop. Rates are given in mHz.

and the laser's frequency stability. These error sources contribute to the dependency of the Bell state fidelities on the fiber length shown in Fig. B.6.

B.10 Compatibility to true space-like separated nodes

Our experimental configuration allows for true space-like separation of the quantum network nodes. The added complexity from the large physical separation can be divided into three categories: synchronization of quantum control hardware, frequency stabilization of lasers, and classical communication of software-timed signals. Our quantum control hardware consists of two AWGs, with one performing the role of the controller AWG, and one as the worker AWG. The worker AWG does not perform any logic operation and is activated using digital signals from the controller AWG. These digital trigger signals could be easily relayed through an additional deployed telecom fiber [114]. Physically separated nodes also result in the requirement to lock the frequency of two lasers at both

nodes. This is particularly important for the laser generating the photonic time-bin qubits at node A, which should match the linewidth and frequency of the laser used to lock the TDI in node B. Such frequency stabilization could be performed by locking both lasers to stable reference cavities located in both nodes. The same strategy could be used for the 1623 nm pump laser used for QFC. Finally, software-timed communication currently is performed using our local area network (LAN) based laboratory control software [102]. Extending this LAN-based approach to use the internet or a dedicated optical-fiber network is straightforward. It is worth noting that true-space-like separation would decrease the repetition rate of the experiment, as signals indicating successful initialization of node B's nuclear and electronic spin will have to travel classically to node A before the entanglement sequence can begin (see Fig. B.1), and because dynamical decoupling needs to be performed after every entanglement attempt, as opposed to only decoupling after receiving a heralding click, as is done in this work.

References

[1] Feynman, R. P. Simulating physics with computers. *Journal of Theoretical Physics* **21**, 467–488 (1981).

[2] Preskill, J. Quantum computing 40 years later. arXiv:2106.10522 (2023).

[3] Shor, P. Algorithms for quantum computation: discrete logarithms and factoring. In *Proceedings 35th Annual Symposium on Foundations of Computer Science*, 124–134 (1994).

[4] Deutsch, D. & Jozsa, R. Rapid solution of problems by quantum computation. In *Proceedings of The Royal Society A*, vol. 439, 553–558 (1992).

[5] Grover, L. K. A fast quantum mechanical algorithm for database search. In *Proceedings of the Twenty-Eighth Annual ACM Symposium on Theory of Computing*, 212–219 (1996).

[6] Bennett, C. H. & , G., Brassard. Quantum cryptography: Public key distribution and coin tossing. In *Proceedings of IEEE International Conference on Computers, Systems and Signal Processing*, vol. 175, 8 (1984).

[7] Nielsen, M. A. & Chuang, I. L. *Quantum Computation and Quantum Information: 10th Anniversary Edition* (Cambridge University Press, 2010).

[8] Park, J. L. The concept of transition in quantum mechanics. *Foundations of physics* **1**, 23–33 (1970).

[9] Gisin, N., Ribordy, G., Tittel, W. & Zbinden, H. Quantum cryptography. *Reviews of Modern Physics* **74**, 145–195 (2002).

[10] Bennett, C. H., Bessette, F., Brassard, G., Salvail, L. & Smolin, J. Experimental quantum cryptography. *Journal of cryptology* **5**, 3–28 (1992).

[11] Ekert, A. K. Quantum cryptography based on bell's theorem. *Physical Review Letters* **67**, 661–663 (1991).

[12] Clauser, J. F., Horne, M. A., Shimony, A. & Holt, R. A. Proposed experiment to test local hidden-variable theories. *Physical Review Letters* **23**, 880–884 (1969).

[13] Bell, J. S. & Aspect, A. *Speakable and Unspeakable in Quantum Mechanics: Collected Papers on Quantum Philosophy* (Cambridge University Press, 2004), 2 edn.

[14] Hensen, B. *et al.* Loophole-free bell inequality violation using electron spins separated by 1.3 kilometres. *Nature 2015 526:7575* **526**, 682–686 (2015).

[15] Giustina, M. *et al.* Significant-loophole-free test of bell's theorem with entangled photons. *Physical Review Letters* **115**, 250401 (2015).

[16] Kimble, H. J. The quantum internet. *Nature* **453**, 1023–1030 (2008).

[17] Duan, L.-M., Lukin, M. D., Cirac, J. I. & Zoller, P. Long-distance quantum communication with atomic ensembles and linear optics. *Nature* **414**, 413–418 (2001).

[18] Briegel, H. J., Dür, W., Cirac, J. I. & Zoller, P. Quantum repeaters: The role of imperfect local operations in quantum communication. *Physical Review Letters* **81**, 5932–5935 (1998).

[19] Azuma, K. *et al.* Quantum repeaters: From quantum networks to the quantum internet. *Reviews of Modern Physics* **95**, 045006 (2023).

[20] Monroe, C. *et al.* Large-scale modular quantum-computer architecture with atomic memory and photonic interconnects. *Physical Review A* **89**, 022317 (2014).

[21] Ang, J. *et al.* Architectures for multinode superconducting quantum computers. arXiv:2212.06167 (2022).

[22] Khabiboulline, E. T., Borregaard, J., Greve, K. D. & Lukin, M. D. Optical interferometry with quantum networks. *Physical Review Letters* **123**, 070504 (2019).

[23] Giovannetti, V., Lloyd, S. & Maccone, L. Quantum-enhanced positioning and clock synchronization. *Nature* **412**, 417–419 (2001).

[24] Khrapko, R. *et al.* Quasi single-mode fiber with record-low attenuation of 0.1400 db/km. *IEEE Photonics Technology Letters* **36**, 539–542 (2024).

[25] Iq quantique clavis xg qkd spec sheet. https://www.idquantique.com/quantum-safe-security/products/clavis-xg-qkd-system/. Accessed: 2024-09-18.

[26] Ramette, J., Sinclair, J., Breuckmann, N. P. & Vuletić, V. Fault-tolerant connection of error-corrected qubits with noisy links. *npj Quantum Information* **10**, 58 (2024).

[27] Acharya, R. *et al.* Quantum error correction below the surface code threshold. arXiv:2408.13687 (2024).

[28] Bluvstein, D. *et al.* Logical quantum processor based on reconfigurable atom arrays. *Nature* **626**, 58–65 (2024).

[29] Beverland, M. E. *et al.* Assessing requirements to scale to practical quantum advantage. arXiv:2211.07629 (2022).

[30] Fitzsimons, J. F. Private quantum computation: an introduction to blind quantum computing and related protocols. *npj Quantum Information* **3**, 23 (2017).

[31] Khabiboulline, E. T., Borregaard, J., Greve, K. D. & Lukin, M. D. Quantum-assisted telescope arrays. *Physical Review A* **100**, 022316 (2019).

[32] Hofmann, J. *et al.* Heralded entanglement between widely separated atoms. *Science* **337**, 72–75 (2012).

[33] Daiss, S. *et al.* A quantum-logic gate between distant quantum-network modules. *Science* **371**, 614–617 (2021).

[34] Ritter, S. *et al.* An elementary quantum network of single atoms in optical cavities. *Nature* **484**, 195–200 (2012).

[35] van Leent, T. *et al.* Entangling single atoms over 33 km telecom fibre. *Nature* **607**, 69–73 (2022).

[36] Krutyanskiy, V. *et al.* Entanglement of trapped-ion qubits separated by 230 meters. *Physical Review Letters* **130**, 050803 (2023).

[37] Stephenson, L. J. *et al.* High-rate, high-fidelity entanglement of qubits across an elementary quantum network. *Physical Review Letters* **124**, 110501 (2020).

[38] Stockill, R. *et al.* Phase-tuned entangled state generation between distant spin qubits. *Physical Review Letters* **119**, 010503 (2017).

[39] Bernien, H. *et al.* Heralded entanglement between solid-state qubits separated by three metres. *Nature* **497**, 86–90 (2013).

[40] Humphreys, P. C. *et al.* Deterministic delivery of remote entanglement on a quantum network. *Nature* **558**, 268–273 (2018).

[41] Luo, X.-Y. *et al.* Postselected entanglement between two atomic ensembles separated by 12.5 km. *Physical Review Letters* **129**, 050503 (2022).

[42] Yu, Y. *et al.* Entanglement of two quantum memories via fibres over dozens of kilometres. *Nature* **578**, 240–245 (2020).

[43] Liu, J.-L. *et al.* Creation of memory–memory entanglement in a metropolitan quantum network. *Nature* **629**, 579–585 (2024).

[44] Higginbottom, D. B. *et al.* Optical observation of single spins in silicon. *Nature* **607**, 266–270 (2022).

[45] Nagy, R. *et al.* High-fidelity spin and optical control of single silicon-vacancy centres in silicon carbide. *Nature communications* **10**, 1–8 (2019).

[46] Ruskuc, A. *et al.* Scalable multipartite entanglement of remote rare-earth ion qubits. arXiv:2402.16224 (2024).

[47] Janitz, E., Bhaskar, M. K. & Childress, L. Cavity quantum electrodynamics with color centers in diamond. *Optica* **7**, 1232–1252 (2020).

[48] Hepp, C. Electronic structure of the silicon vacancy color center in diamond. *PhD Dissertation, Universität des Saarlandes* (2014).

[49] Sukachev, D. D. *et al.* Silicon-vacancy spin qubit in diamond: A quantum memory exceeding 10 ms with single-shot state readout. *Physical Review Letters* **119**, 223602 (2017).

[50] Jahnke, K. D. *et al.* Electron–phonon processes of the silicon-vacancy centre in diamond. *New Journal of Physics* **17**, 043011 (2015).

[51] Nguyen, C. T. *et al.* Quantum network nodes based on diamond qubits with an efficient nanophotonic interface. *Physical Review Letters* **123**, 183602 (2019).

[52] Meesala, S. *et al.* Strain engineering of the silicon-vacancy center in diamond. *Physical Review B* **97**, 205444 (2018).

[53] Stas, P.-J. *et al.* Robust multi-qubit quantum network node with integrated error detection. *Science* **378**, 557–560 (2022).

[54] Pingault, B. *et al.* Coherent control of the silicon-vacancy spin in diamond. *Nature Communications* **8**, 15579 (2017).

[55] Reiserer, A. & Rempe, G. Cavity-based quantum networks with single atoms and optical photons. *Reviews of Modern Physics* **87**, 1379–1418 (2015).

[56] Burek, M. J. *et al.* Fiber-coupled diamond quantum nanophotonic interface. *Physical Review Applied* **8**, 024026 (2017).

[57] Hepp, C. *et al.* Electronic structure of the silicon vacancy color center in diamond. *Physical Review Letters* **112**, 036405 (2014).

[58] Doherty, M. W. *et al.* The nitrogen-vacancy colour centre in diamond. *Physics Reports* **528**, 1–45 (2013).

[59] Faraon, A., Santori, C., Huang, Z., Acosta, V. M. & Beausoleil, R. G. Coupling of nitrogen-vacancy centers to photonic crystal cavities in monocrystalline diamond. *Physical Review Letters* **109**, 033604 (2012).

[60] Green, B. L. *et al.* Electronic structure of the neutral silicon-vacancy center in diamond. *Physical Review B* **99**, 1–6 (2019).

[61] Rose, B. C. *et al.* Observation of an environmentally insensitive solid-state spin defect in diamond. *Science* **361**, 60–63 (2018).

[62] Zhang, Z.-H. *et al.* Neutral silicon vacancy centers in undoped diamond via surface control. *Physical Review Letters* **130**, 166902 (2023).

[63] Zhang, Z.-H., Edmonds, A. M., Palmer, N., Markham, M. L. & de Leon, N. P. Neutral silicon-vacancy centers in diamond via photoactivated itinerant carriers. *Physical Review Applied* **19**, 034022 (2023).

[64] Bhaskar, M. K. *et al.* Experimental demonstration of memory-enhanced quantum communication. *Nature* **580**, 60–64 (2020).

[65] Knaut, C. M. *et al.* Entanglement of nanophotonic quantum memory nodes in a telecom network. *Nature* **629**, 573–578 (2024).

[66] Raussendorf, R. & Briegel, H. J. A one-way quantum computer. *Physical Review Letters* **86**, 5188–5191 (2001).

[67] Kok, P. *et al.* Linear optical quantum computing with photonic qubits. *Reviews of Modern Physics* **79**, 135 (2007).

[68] Wang, H. *et al.* Towards optimal single-photon sources from polarized microcavities. *Nature Photonics* **13**, 770–775 (2019).

[69] Eisaman, M. D., Fan, J., Migdall, A. & Polyakov, S. V. Invited review article: Single-photon sources and detectors. *Review of Scientific Instruments* **82**, 071101 (2011).

[70] Kuhn, A., Hennrich, M. & Rempe, G. Deterministic Single-Photon Source for Distributed Quantum Networking. *Physical Review Letters* **89**, 4–7 (2002).

[71] McKeever, J. *et al.* Deterministic generation of single photons from one atom trapped in a cavity. *Science* **303**, 1992–1994 (2004).

[72] Keller, M., Lange, B., Hayasaka, K., Lange, W. & Walther, H. Continuous generation of single photons with controlled waveform in an ion-trap cavity system. *Nature* **431**, 1075–1078 (2004).

[73] Michler, P. *et al.* Quantum correlation among photons from a single quantum dot at room temperature. *Nature* **406**, 968–970 (2000).

[74] Yuan, Z. *et al.* Electrically driven single-photon source. *Science* **295**, 102–105 (2002).

[75] Beveratos, A. *et al.* Single photon quantum cryptography. *Physical Review Letters* **89**, 187901 (2002).

[76] Uppu, R. *et al.* Scalable integrated single-photon source. *Science Advances* **6**, 1–6 (2020).

[77] He, Y.-M. *et al.* Deterministic implementation of a bright, on-demand single-photon source with near-unity indistinguishability via quantum dot imaging. *Optica* **4**, 802 (2017).

[78] Unsleber, S. *et al.* Highly indistinguishable on-demand resonance fluorescence photons from a deterministic quantum dot micropillar device with 74% extraction efficiency. *Opt. Express* **24**, 8539–8546 (2016).

[79] Arcari, M. *et al.* Near-unity coupling efficiency of a quantum emitter to a photonic crystal waveguide. *Physical Review Letters* **113**, 093603 (2014).

[80] Tomm, N. *et al.* A bright and fast source of coherent single photons. *Nature Nanotechnology* **16**, 399–403 (2021).

[81] Muralidharan, S., Kim, J., Lütkenhaus, N., Lukin, M. D. & Jiang, L. Ultrafast and fault-tolerant quantum communication across long distances. *Physical Review Letters* **112**, 1–6 (2014).

[82] Kalb, N., Reiserer, A., Ritter, S. & Rempe, G. Heralded storage of a photonic quantum bit in a single atom. *Physical Review Letters* **114**, 220501 (2015).

[83] Duan, L. M. & Kimble, H. J. Scalable photonic quantum computation through cavity-assisted interactions. *Physical Review Letters* **92**, 127902 (2004).

[84] Baek, B., Stevens, M. J., Nam, S. W. & Dyer, S. D. High-efficiency, ultra low-noise all-fiber photon-pair source. *Optics Express, Vol. 16, Issue 13, pp. 9966-9977* **16**, 9966–9977 (2008).

[85] song Ma, X., Zotter, S., Kofler, J., Jennewein, T. & Zeilinger, A. Experimental generation of single photons via active multiplexing. *Physical Review A* **83**, 043814 (2011).

[86] Mücke, M. *et al.* Generation of single photons from an atom-cavity system. *Physical Review A* **87**, 1–6 (2013).

[87] Schupp, J. *et al.* Interface between Trapped-Ion Qubits and Traveling Photons with Close-to-Optimal Efficiency. *Physical Review X Quantum* **2**, 1 (2021).

[88] Pursley, B. C., Carter, S. G., Yakes, M. K., Bracker, A. S. & Gammon, D. Picosecond pulse shaping of single photons using quantum dots. *Nature Communications 2017 9:1* **9**, 1–6 (2018).

[89] He, Y. *et al.* Indistinguishable tunable single photons emitted by spin-flip raman transitions in ingaas quantum dots. *Physical Review Letters* **111**, 237403 (2013).

[90] Borregaard, J. *et al.* One-Way Quantum Repeater Based on Near-Deterministic Photon-Emitter Interfaces. *Physical Review X* **10**, 21071 (2020).

[91] Schwartz, I. *et al.* Deterministic generation of a cluster state of entangled photons. *Science* **354**, 434–437 (2016).

[92] Gimeno-Segovia, M., Rudolph, T. & Economou, S. E. Deterministic generation of large-scale entangled photonic cluster state from interacting solid state emitters. *Physical Review Letters* **123**, 070501 (2019).

[93] Tiurev, K. *et al.* High-fidelity multiphoton-entangled cluster state with solid-state quantum emitters in photonic nanostructures. *Physical Review A* **105**, L030601 (2022).

[94] Buterakos, D., Barnes, E. & Economou, S. E. Deterministic generation of all-photonic quantum repeaters from solid-state emitters. *Physical Review X* **7**, 041023 (2017).

[95] Lindner, N. H. & Rudolph, T. Proposal for pulsed on-demand sources of photonic cluster state strings. *Physical Review Letters* **103**, 113602 (2009).

[96] Nguyen, C. T. *et al.* An integrated nanophotonic quantum register based on silicon-vacancy spins in diamond. *Physical Review B* **100**, 165428 (2019).

[97] Rogers, L. J. *et al.* All-optical initialization, readout, and coherent preparation of single silicon-vacancy spins in diamond. *Physical Review Letters* **113**, 263602 (2014).

[98] Jahnke, K. D. *et al.* Electron–phonon processes of the silicon-vacancy centre in diamond. *New Journal of Physics* **17**, 043011 (2015).

[99] Joannopoulos, J. D., Johnson, S. G., Winn, J. N. & Meade, R. D. Photonic crystals: Molding the flow of light. *Photonic Crystals: Molding the Flow of Light (Second Edition)* (2008).

[100] Miguel-Ramiro, J. & Dür, W. Efficient entanglement purification protocols for d-level systems. *Physical Review A* **98**, 042309 (2018).

[101] Cozzolino, D., Lio, B. D., Bacco, D. & Oxenløwe, L. K. High-dimensional quantum communication: Benefits, progress, and future challenges. *Advanced Quantum Technologies* **2**, 1900038 (2019).

[102] Knaut, C. M. *et al.* pylabnet - Client-server, python-based laboratory software (2021).

[103] Kiršanske, G. *et al.* Indistinguishable and efficient single photons from a quantum dot in a planar nanobeam waveguide. *Physical Review B* **96**, 1–11 (2017).

[104] Zhong, H.-S. *et al.* 12-photon entanglement and scalable scattershot boson sampling with optimal entangled-photon pairs from parametric down-conversion. *Physical Review Letters* **121**, 250505 (2018).

[105] Weisskopf, V. & Wigner, E. Berechnung der natürlichen linienbreite auf grund der diracschen lichttheorie. In *Part I: Particles and Fields. Part II: Foundations of Quantum Mechanics*, 30–49 (Springer, 1997).

[106] Johansson, J., Nation, P. & Nori, F. QuTiP 2: A Python framework for the dynamics of open quantum systems. *Computer Physics Communications* **184**, 1234–1240 (2013).

[107] Wehner, S., Elkouss, D. & Hanson, R. Quantum internet: A vision for the road ahead. *Science* **362**, eaam9288 (2018).

[108] Sipahigil, A. *et al.* An integrated diamond nanophotonics platform for quantum-optical networks. *Science* **354**, 847–850 (2016).

[109] Ourari, S. *et al.* Indistinguishable telecom band photons from a single erbium ion in the solid state. *Nature* **620**, 977–981 (2023).

[110] Ruskuc, A., Wu, C.-J., Rochman, J., Choi, J. & Faraon, A. Nuclear spin-wave quantum register for a solid-state qubit. *Nature* **602**, 408–413 (2022).

[111] Riedel, D. *et al.* Efficient photonic integration of diamond color centers and thin-film lithium niobate. *ACS Photonics* (2023).

[112] Molesky, S. *et al.* Inverse design in nanophotonics. *Nature Photonics* **12**, 659–670 (2018).

[113] Parker, R. A. *et al.* A diamond nanophotonic interface with an optically accessible deterministic electronuclear spin register. *Nature Photonics* (2023).

[114] Bersin, E. *et al.* Telecom networking with a diamond quantum memory. *Physical Review X Quantum* **5**, 010303 (2024).

[115] Bersin, E. *et al.* Development of a boston-area 50-km fiber quantum network testbed. *Physical Review Applied* **21**, 014024 (2024).

[116] Barrett, S. D. & Kok, P. Efficient high-fidelity quantum computation using matter qubits and linear optics. *Physical Review A* **71**, 060310(R) (2005).

[117] Drmota, P. *et al.* Verifiable blind quantum computing with trapped ions and single photons. *Physical Review Letters* **132**, 150604 (2024).

[118] Nichol, B. C. *et al.* An elementary quantum network of entangled optical atomic clocks. *Nature* **609**, 689–694 (2022).

[119] Thomas, P., Ruscio, L., Morin, O. & Rempe, G. Efficient generation of entangled multiphoton graph states from a single atom. *Nature* **608**, 677–681 (2022).

[120] Wang, X. *et al.* Quantum frequency conversion and single-photon detection with lithium niobate nanophotonic chips. *npj Quantum Information* **9**, 38 (2023).

[121] Schäfer, M., Kambs, B., Herrmann, D., Bauer, T. & Becher, C. Two-stage, low noise quantum frequency conversion of single photons from silicon-vacancy centers in diamond to the telecom c-band. *Advanced Quantum Technologies* 2300228 (2023).

[122] Knall, E. *et al.* Efficient source of shaped single photons based on an integrated diamond nanophotonic system. *Physical Review Letters* **129**, 053603 (2022).

[123] Machielse, B. *et al.* Quantum interference of electromechanically stabilized emitters in nanophotonic devices. *Physical Review X* **9**, 031022 (2019).

[124] Zeng, B. *et al.* Cryogenic optical packaging of nanophotonic devices with coupling loss $<$ 1dB. *Applied Physics Letters* **123**, 161106 (2023).

[125] Assumpcao, D. R. *et al.* Deterministic creation of strained color centers in nanostructures via high-stress thin films. *Applied Physics Letters* **123**, 244001 (2023).

[126] Bradley, C. E. *et al.* A ten-qubit solid-state spin register with quantum memory up to one minute. *Physical Review X* **9**, 031045 (2019).

[127] Burek, M. J. *et al.* High quality-factor optical nanocavities in bulk single-crystal diamond. *Nature Communications* **5**, 1–7 (2014).

[128] Ding, S. W. *et al.* High-q cavity interface for color centers in thin film diamond. *Nature communications* **15**, 6358 (2024).

[129] Guo, X. *et al.* Microwave-based quantum control and coherence protection of tin-vacancy spin qubits in a strain-tuned diamond-membrane heterostructure. *Physical Review X* **13**, 041037 (2023).

[130] Kuruma, K. *et al.* Coupling of a single tin-vacancy center to a photonic crystal cavity in diamond. *Applied Physics Letters* **118** (2021).

[131] Bennett, C. H. *et al.* Purification of noisy entanglement and faithful teleportation via noisy channels. *Physical Review Letters* **76**, 722–725 (1996).

[132] Beukers, H. K. C. *et al.* Control of solid-state nuclear spin qubits using an electron spin-1/2. arXiv:2409.08977 (2024).

[133] Osterkamp, C. *et al.* Engineering preferentially-aligned nitrogen-vacancy centre ensembles in cvd grown diamond. *Scientific reports* **9**, 5786 (2019).

[134] Lang, J. *et al.* Long optical coherence times of shallow-implanted, negatively charged silicon vacancy centers in diamond. *Applied Physics Letters* **116** (2020).

[135] Kastoryano, M. J., Reiter, F. & Sørensen, A. S. Dissipative preparation of entanglement in optical cavities. *Physical Review Letters* **106**, 2–5 (2011).

[136] Borregaard, J., Kómár, P., Kessler, E. M., Lukin, M. D. & Sørensen, A. S. Long-distance entanglement distribution using individual atoms in optical cavities. *Physical Review A* **92**, 1–15 (2015).

[137] Evans, R. E. *et al.* Photon-mediated interactions between quantum emitters in a diamond nanocavity. *Science* **362**, 662–665 (2018).

[138] Akahane, Y., Asano, T., Song, B. S. & Noda, S. High-Q photonic nanocavity in a two-dimensional photonic crystal. *Nature* **425**, 944–947 (2003).

[139] Tiecke, T. G. *et al.* Nanophotonic quantum phase switch with a single atom. *Nature* **508**, 241–244 (2014).

[140] Senellart, P., Solomon, G. & White, A. High-performance semiconductor quantum-dot single-photon sources. *Nature Nanotechnology 2017 12:11* **12**, 1026–1039 (2017).

This thesis was typeset using LaTeX, originally developed by Leslie Lamport and based on Donald Knuth's TeX. The body text is set in 11 point Egenolff-Berner Garamond, a revival of Claude Garamont's humanist typeface. A template that can be used to format a PhD thesis with this look and feel has been released under the permissive MIT (X11) license, and can be found online at github.com/suchow/Dissertate or from its author, Jordan Suchow, at suchow@post.harvard.edu.